(1)

REPORT DOCUMENTATION PAGE

READ INSTRUCTIONS BEFORE COMPLETING FORM

1. REPORT NUMBER: AFIT/CI/NR 88- 187
2. GOVT ACCESSION NO.
3. RECIPIENT'S CATALOG NUMBER

TITLE (and Subtitle): KINEMATIC AND DYNAMIC STUDIES OF MICROBURSTS IN THE SUBCLOUD LAYER DERIVED FROM JAWS DUAL-DOPPLER RADAR FOR A COLORADO THUNDERSTORM

5. TYPE OF REPORT & PERIOD COVERED: MS THESIS
6. PERFORMING ORG. REPORT NUMBER

AUTHOR(s): JOHN ANTHONY COOVER, JR

8. CONTRACT OR GRANT NUMBER(s)

PERFORMING ORGANIZATION NAME AND ADDRESS: AFIT STUDENT AT: SAINT LOUIS UNIVERSITY

10. PROGRAM ELEMENT, PROJECT, TASK AREA & WORK UNIT NUMBERS

11. CONTROLLING OFFICE NAME AND ADDRESS

12. REPORT DATE: 1988
13. NUMBER OF PAGES: 225

14. MONITORING AGENCY NAME & ADDRESS (if different from Controlling Office):
AFIT/NR
Wright-Patterson AFB OH 45433-6583

15. SECURITY CLASS. (of this report): UNCLASSIFIED
15a. DECLASSIFICATION/DOWNGRADING SCHEDULE

16. DISTRIBUTION STATEMENT (of this Report)

DISTRIBUTED UNLIMITED: APPROVED FOR PUBLIC RELEASE

17. DISTRIBUTION STATEMENT (of the abstract entered in Block 20, if different from Report)

SAME AS REPORT

18. SUPPLEMENTARY NOTES

Approved for Public Release: IAW AFR 190-1
LYNN E. WOLAVER 19 Aug 88
Dean for Research and Professional Development
Air Force Institute of Technology
Wright-Patterson AFB OH 45433-6583

19. KEY WORDS (Continue on reverse side if necessary and identify by block number)

20. ABSTRACT (Continue on reverse side if necessary and identify by block number)

ATTACHED

DD FORM 1 JAN 73 1473 EDITION OF 1 NOV 65 IS OBSOLETE

KINEMATIC AND DYNAMIC STUDIES OF MICROBURSTS IN THE SUBCLOUD LAYER DERIVED FROM JAWS DUAL-DOPPLER RADAR FOR A COLORADO THUNDERSTORM

John Anthony Coover Jr., B.S., M.S.

A Digest Presented to the Faculty of the Graduate School of Saint Louis University in Partial Fulfillment of the Requirements for the Degree of Doctor of Philosophy

1989

DIGEST

The kinematic, dynamic and thermodynamic features of a simple and a complex microburst event were calculated, and comparisons were made in order to find common and unique structural features that might lead to greater insight into the physical mechanisms responsible for microburst development. Dual-Doppler radar data from CP-3 and CP-4, collected near Denver, Colorado, during the Joint Airport Weather Studies (JAWS) project were judiciously edited, gridded and kinematically integrated upward from the surface, to produce a three-dimensional wind field. The retrieved pressure field from the three-dimensional wind field was used to compute a relative "goodness of fit" of the mass field to the momentum field. The perturbation temperature and thermodynamic variables were used to compute the momentum budgets and field was derived from the buoyancy equation, using the derived wind and pressure fields. The complete set of Doppler derived winds and thermodynamic variables were used to compute budgets of the momentum flux and the eddy kinetic energy within the microburst domain, to allow for a more definitive interpretation of the results.

The results from this study reveal some basic similarities, along with some notable differences in structure. Both cases reveal a downward flux of mass, momentum, and eddying

energy within the microburst; the boundary layer above 0.75 km is the source of the mass and momentum; an intermediate level near 0.75 km acts as a conduit for the downward flux; and the surface layer below 0.75 km that comprises the divergent flow enclosed in the microburst. The microburst also included a high reflectivity core at the center. The complex case contains a misocyclone above 0.75 km. The misocyclone will hereafter refer to the cyclonic circulation above the surface microburst. The role played by hail was more significant to the microburst's development. The most significant result of this study was that a combination of physical mechanisms, including evaporative cooling, precipitation drag, downward momentum and eddy kinetic energy flux and hail melt, were responsible for maintaining the microburst, during its mature stage. The degree to which any particular mechanism plays a role in the microburst is dependent on the synoptic scale dynamic and thermodynamic structures.

This dissertation is dedicated to my family,
who have helped me all these years to get to this point. My parents for helping me through my first 4 years of college, and my wife and children for being there my last 4 years.

COMMITTEE IN CHARGE OF CANDIDACY

Professor Yeong-jer Lin,
Chairperson and Advisor

Professor Gandikota V. Rao

Assistant Professor Lawrence Coy

ACKNOWLEDGEMENTS

The author would like to express his deepest thanks to Dr. Yeong-jer Lin for his guidance and assistance in completing this dissertation. He also thanks Drs. Gandikota V. Rao and Lawrence Coy for their helpful comments and suggestions. Special thanks go to P. Wright and for his help in computational problems encountered during the course of this study. Thanks to K. Elmore for ground clutter removal from the raw data, and to S. Lasher for her help with the tables and in editing this manuscript. The author is grateful to Dr. R. W. Pasken for his initial development of the software used in thermodynamic retrieval and to the National Center Atmospheric Research (NCAR) for providing the initial dual-Doppler data. Special thanks for my wife [redacted] and my daughters [redacted] for their support.

This research has been partially supported by the Division of Atmospheric Sciences, National Science Foundation, under Grants ATM-8312172 and ATM-8312172-01 and by the Air Force Institute of Technology (AFIT).

TABLE OF CONTENTS

TABLE OF CONTENTS (CONTINUED)

TABLE OF CONTENTS (CONTINUED)

LIST OF TABLES

LIST OF FIGURES

LIST OF FIGURES (CONTINUED)

LIST OF FIGURES (CONTINUED)

LIST OF FIGURES (CONTINUED)

LIST OF FIGURES (CONTINUED)

1. Introduction

The downburst was first identified by Fujita (1976), after a study of an aircraft accident at John F. Kennedy airport in New York City, N.Y. in 1975. It was quantified as a small downburst of cool air within a 4 km diameter capable of producing damaging winds up to 75 m/s. The dry and wet downburst types were first quantified by Fujita and Wakimoto (1983) in terms of measurable precipitation associated with the downburst. Fujita (1985) found that 83% of the JAWS microbursts were of the dry variety.

A microburst was further defined by Wilson et al. (1984) as a divergent horizontal outflow of horizontal diameter 4 km with total horizontal shear > 10 m/s. Larger scale phenomena are referred to as macrobursts. Evaporative cooling was shown by Srivastava (1985) as an important mechanism in initiating downdrafts in the subcloud layer for high-based cumulonimbus resembling those found on the high plains. The kinematic structure of the downburst was examined by Wilson et al. (1984) and a pilot of the dynamics and thermodynamics was completed by Lin et al. (1987).

Studies using dual-Doppler radar do not directly provide a Cartesian three-dimensional wind field, nor pressure and

temperature perturbations. The wind, perturbation pressure and perturbation temperature fields are required when studies of the momentum flux and kinetic energy budgets are made. Therefore, indirect retrieval of these quantities is required. A method for recovery of the 3-D wind field was formulated by Armijo (1969), which is used in this study. Pressure and temperature are not directly measured but are indirectly measured as the perturbation quantities. These quantities vary a few degrees of temperature or a few millibars of pressure from their mean value. These quantities cannot be accurately measured by other passive or active sensors.

Gal-Chen (1978) proposed a retrieval method where the perturbation density, pressure and temperature deviations are recovered by solving a special form of the momentum equations using a known 3-D Cartesian wind field. This method has been used on both model and observed data by Gal-Chen (1978), Hane et al. (1981), Lin and Pasken (1982), Brandes (1984), Roux et al. (1984), Hane and Ray (1985), Lin et al. (1986) and Lin et al. (1987).

Since thermodynamic retrieval is indirect, data accuracy is critical to an accurate result (Hane et al., 1981). A verification scheme is required to insure the accuracy of the retrieved variables. Gal-Chen and Hane (1981) suggested momen-

tum checking and time continuity as methods. Momentum checking does not require a sequence of time periods for comparison, as time continuity checking does, so it is more widely used. Momentum checking was used by Gal-Chen and Kropfli (1984), Hane and Ray (1985) Lin et al. (1986) and Lin et al. (1987). Time continuity checking was used by Gal-Chen and Kropfli (1984). The previous studies determined that the accuracy of observed winds was crucial in determining the applicability of thermodynamic retrieval.

1.1 Momentum Budgets for Convective Storms

Strong wind shears in the boundary layer during the JAWS project have been noted by Wilson et al. (1984) and Lin et al. (1987). The spatial and temporal resolution is at least meso γ-scale, which would allow for an investigation of momentum transfer and eddy mixing in the subcloud layer. A study by Lin et al. (1987) found that microbursts produce stronger wind shear and more effective mixing and momentum transfer.

The generation of momentum in the subcloud layer of a microburst producing storm has been investigated using dual-Doppler radar by Condray (1987). He examined the momentum flux equation patterned after LeMone (1983) and the local flux quantities. The results showed that a counter-gradient momentum

flux occurred below 2 km with strong downdrafts transporting large positive values of momentum downward. Additionally, the buoyancy and pressure terms were of equal magnitude and tended to oppose each other. The divergence and shear terms were weak secondary contributors. Other authors have used rawinsonde data and aircraft measurements to study the momentum budgets of thunderstorms. Results indicate that the horizontal momentum is approximately conserved following the parcel in the updraft. Additionally, the large momentum produced in the low-level sub-cloud layer is carried aloft and a strong downdraft fed by potentially cool air from mid-levels exists (Ogura and Liou, 1980). The vertical transport of horizontal momentum perpendicular to a tropical squall line was counter the vertical mean momentum gradient. LeMone (1983) also noted that the mesoscale pressure was predominately hydrostatic in the zone of active convection. More research is needed to clarify the effect of boundary layer microbursts on generation of horizontal momentum flux.

1.2 Kinetic Energy Budgets for Convective Storms

There are relatively few studies in the literature that describe the effect of areas of intense convection on its immediate environment. Most mesoscale, diagnostic kinetic

energy studies have examined how large areas of convection can modify the larger synoptic-scale kinetic energy balance. Using rawinsonde data from the National Severe Storms Laboratory (NSSL), McInnis and Kung (1972), Rao and Fishman (1974), Kung and Tsui (1975) and Tsui and Kung (1977) studied the meso α-scale storm environment. Environments containing intense convection were typified by anomalously large generation and dissipation of kinetic energy at jet stream level. By contrast, non-convective environments were characterized by massive destruction of kinetic energy from cross-contour flow and transfer of energy from subgrid to grid scales of motion. Meso α-scale energy transformations were an order of magnitude greater than the same processes on the synoptic scale for several environments containing large areas of intense convection. A lack of high resolution data has limited research until recently.

Kinetic energy studies based on finer resolution data became feasible upon completion of the Atmospheric Variability Experiments (AVE) and the AVE-SESAME (Severe Environmental Storms And Mesoscale Experiment) projects. Fuelberg and Scoggins (1978) used AVE-SESAME IV rawinsonde data in computing the kinetic energy balance of the mesoscale convective complex (MCC) described by Maddox (1980). Very large energy changes were contained in areas of convection embedded in a rather inactive region as a whole. The large energy changes in the

storm environment consisted of generation of kinetic energy by cross-contour flow, horizontal flux divergence near jet stream level, upward transport due to large scale ascending motion and transfer of energy from resolvable to non-resolvable scales of motion. They suggested that convection caused energy changes since the maximum of energy conversion and transport occurred near the times and location of the most convection.

Fuelberg and Scoggins (1980) used National Weather Service (NWS) rawinsonde observations in examining the synoptic-scale energy processes present during the Red River Valley tornado outbreak, which occurred within the AVE-SESAME project. The upper-level jet was the dominant physical mechanism in generating energy transformations at the synoptic scale, where the large magnitudes of horizontal flux convergence and cross-contour destruction of kinetic energy were associated with sub-geostrophic flow. Conversely, the convective environment was dominated by the generation of kinetic energy and positive dissipation. Fuelberg et al. (1980) theorized that sub-synoptic scale data may resolve the role of feedback mechanisms between the storm environment and the dynamics of the synoptic scale.

Sub-synoptic scale kinetic energy studies for the Red River Valley tornado outbreak were conducted by Fuelberg and

Jedlovec (1982) and Fuelberg and Printy (1984). The presence of additional rawinsonde observations provided finer spatial resolution than was obtained by Fuelberg et al. (1980). Additional results from Fuelberg and Printy (1984) showed that the convective environment was energetically very active compared to the entire analyzed domain. Furthermore, the magnitudes of energy transformations in the convective environment were significantly larger and the effects were more discernible than at the synoptic scale.

A study of a modified meso γ-scale kinetic energy budget for a severe convective cell embedded within a squall line was completed by Coover (1986). Results indicate that the flux divergence term is of great importance within the convective cell and that the updraft/downdraft centers generate the majority of kinetic energy and are the most energetically active. The terms tended to be one order of magnitude greater than previous meso β-scale study results. The kinetic energy generation term was balanced by the divergence term rather than the dissipation term of previous studies at larger scales. The subcloud layer was not included in the budget due to a lack of data. The current research will concentrate on the subcloud layer.

A study of the total kinetic energy budget conducted by Rupp (1987) was conducted on the 1647 MDT, 14 July 1982 case.

The results showed that: 1) the horizontal flux divergence and horizontal generation terms act as a source of kinetic energy with turbulent dissipation as a sink; 2) horizontal flux divergence prevails above 5 km AGL with convergence dominating below. The vertical and horizontal flux divergence term nearly are in balance and 3) the buoyancy term balances with the vertical generation term.

Pan (1987) conducted an eddy kinetic energy budget on the 1647 MDT, 14 July 1982 case. Results from this study, which focused on an ideal case of a single microburst with no significant secondary circulations, demonstrate that eddy kinetic energy is transported downward, the horizontal flux divergence due to eddy motion acts as the main source of eddy kinetic energy, the eddy kinetic energy from the horizontal flux divergence due to mean motion and frictional dissipation act as sinks and the total buoyancy term is approximately balanced by the vertical generation term.

2. Statement of the Problem

Examination of the dynamics resulting from wet microbursts is not presently possible by means other than Doppler radar observations. The problem is to process the dual-Doppler data from raw signals to kinematic and thermodynamic variables that can be used to calculate the microburst dynamics, which describe the physical processes that maintain the microburst. The problem is an inversion problem where physical variables present in the atmosphere such as temperature, pressure and three-dimensional wind are recovered from changes in the Doppler signal.

The Doppler radar emits a signal, which is attenuated by raindrops, hail and other obstacles along the path. The interaction causes a phase shift, which may be separately calculated based upon the strength of the return signal. The collected data are statistical quantities, which require the investigator to examine possible sources of error and uncertainty.

Uncertainty in the data must be evaluated with an eye to quantizing its impact on the eventual calculation of the dynamic equations and budgets. Because this research is fairly specialized and techniques for evaluating the impact of

uncertainty are not always tractable, a qualitative description of the phenomenon and an estimate or informed speculation may be necessary.

3. Methodology

Doppler radar collected raw data from several sites around Stapleton Airport. NCAR's CP-2, CP-3 and CP-4, located at these sites, formed a triangle with base lines of length 15, 18 and 28 km (Fig. 3.1). The technical characteristics are outlined in Table 1. The data were collected in 2 min time scans by slowly increasing the elevation angle per azimuth sweep. A microburst was noted at 1846 MDT near the middle of the analysis domain. The shallow volume scans being considered were centered on times 1845, 1847 and 1850 MDT for 5 August 1982.

The shallow volume scans with five layer, 0.25 km vertical resolution are ideal for investigating subcloud boundary layer phenomena. Previous studies by Elmore et al. (1986) and Hughes (1986) on the 5 August 1982 and 14 July 1982 cases, respectively, revealed single microburst events characterized by a region of high pressure at the downdraft core surrounded by a low pressure ring. The downdraft core was characterized (Hughes, 1987) by strong sinking motion and warm (positive) perturbation temperature. Induced circulations include wind rotors in the boundary layer on the upwind side. No well defined horizontal cyclonic circulations were discerned or intensively investigated. A possible role of terrain effects on

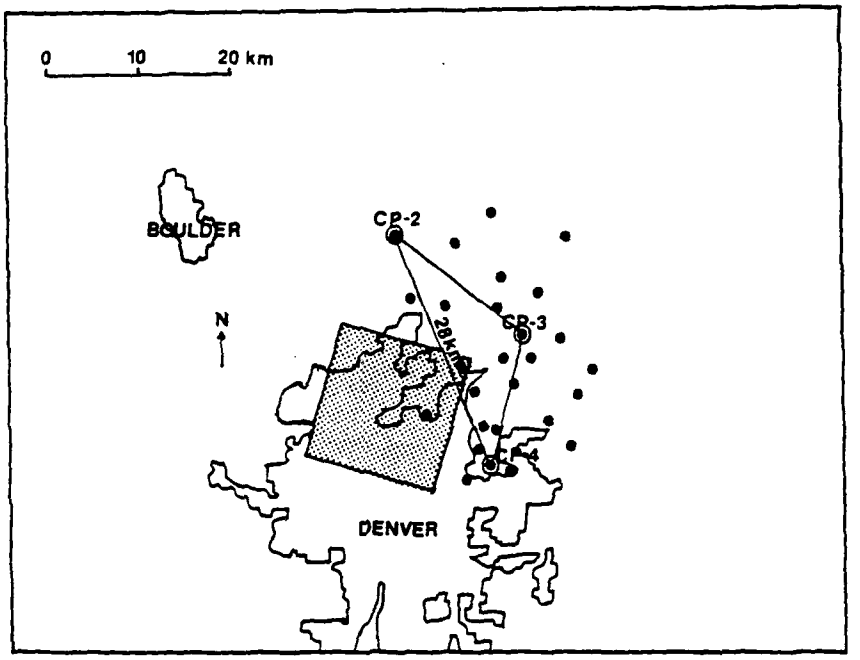

Fig. 3.1 Geometric relationship between the Doppler radars and the domain of interest.

Table 1

NOAA Doppler Radar characteristics for JAWS

Parameter		CP-2	CP-3	CP-4
Wavelength (cm)		10.67	5.45	5.40
Pulse Duration (s)		0.4 to 1.5	1.0	1.0
Avg. Power* (dBm)		59	55	55
Pulse Repetition Frequency (Hz)		960 & 480	1666 & 1250	1666 & 1250
Antenna Diameter (m)		8.534	3.658	3.658
System Gain (dB)		43.0	43.0**	41.0***
Beamwidth (deg)		0.97	1.17	1.00
Minimum Detectable Signal at 10 km (dBz)*	Reflectivity	-25	-10	-24
	Velocity	-25	-23	-24

*Representative Values

**Radar Dome Off

***Radar Dome On

the microburst flow has not been examined by other investigators. Also, temporal evolution of the thermodynamic variables, eddy kinetic energy, momentum budget and vorticity budget may be examined. Better understanding of the kinematic, dynamic and thermodynamic structure of a downburst in the subcloud layer over several minutes is a goal of this study.

3.1 The Synoptic Situation

The synoptic situation at 0600 MDT on 5 August 1982 featured low pressure systems in southwest Kansas and southeast Montana (Fig. 3.2). A quasi-stationary front connected the low pressure centers and bisected northeast Colorado. The front moved slowly northeast during the day. The surface forcing and upper-level dynamics were very weak on this day with the jet stream located from Oregon through Idaho and finally exiting the United States from northeast Montana.

The Denver sounding for 0000 GMT (Greenwich Mean Time) on 5 August 1982 (Fig. 3.3) features a well-mixed boundary layer extending to 1.5 km above ground level (AGL). The cumulus convection level is 650 mb, and note that the cumulus temperature of (30 ^{o} C) has been reached. Also note the unusual depth of the moist layer (4.0 - 7.0 km) for a high plains storm and the general lack of mid-level dry air. The height of the wetbulb (0

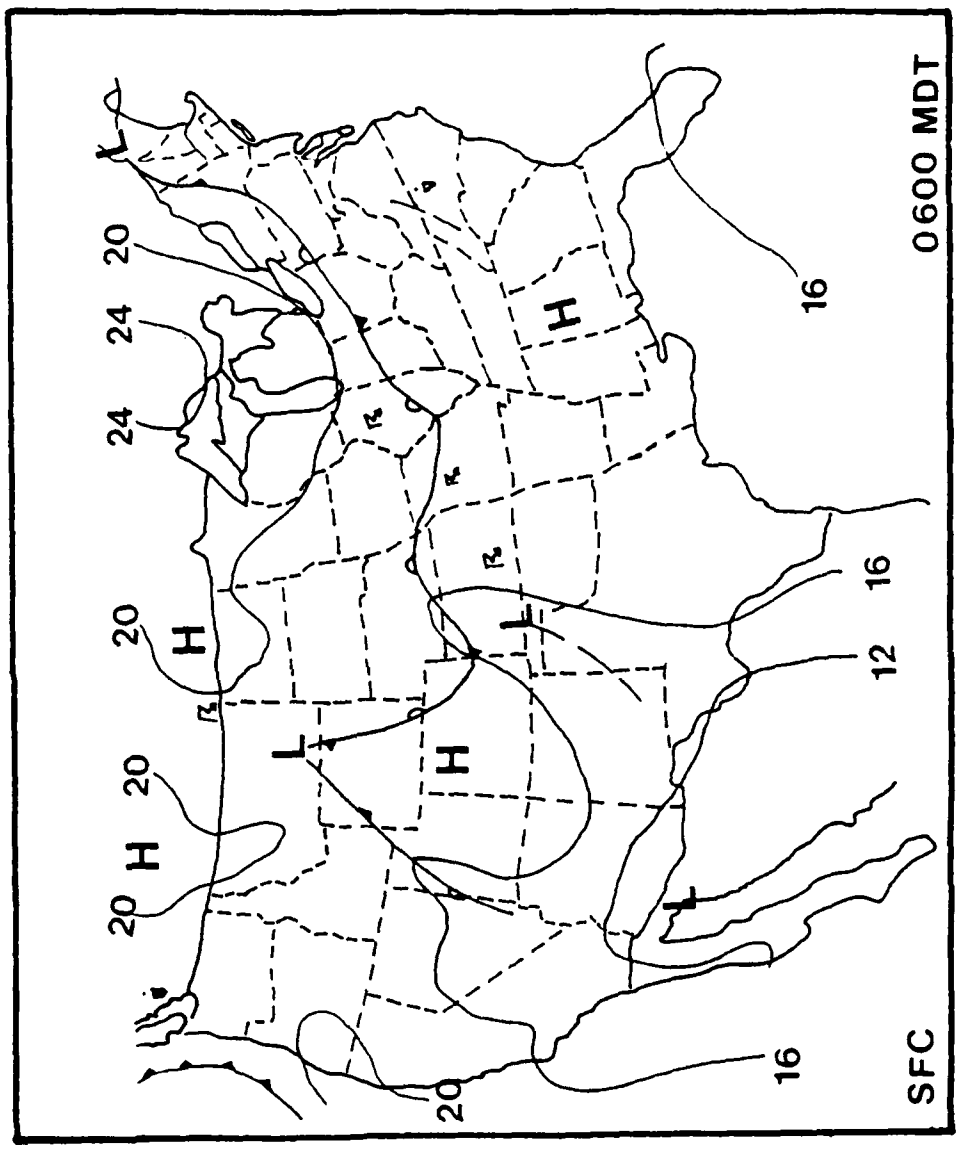

Fig. 3.2 Synoptic situation, 0600 MDT 5 August 1982.

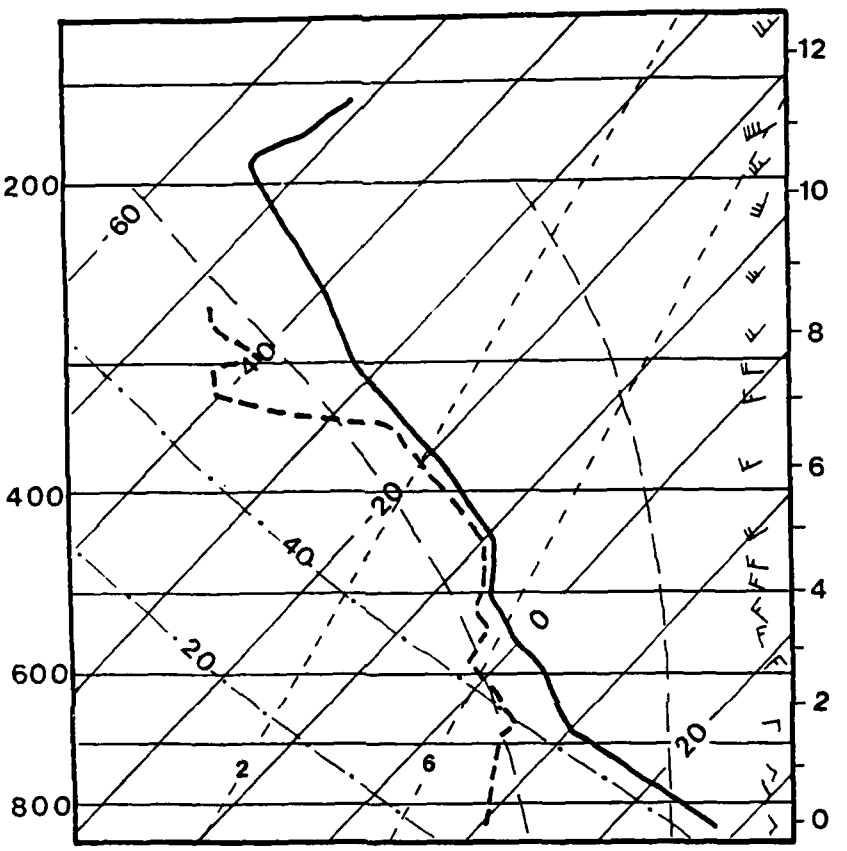

Fig. 3.3 0000Z Sounding for Denver, Co., 5 August 1982.

° C) temperature is 2.8 km AGL, within the range for formation of a hail producing storm. By utilizing the Upper Level Instability (UI) and 700 mb dewpoint depression (TdD), four conditions are predicted to occur, which reflect the likelihood of downburst occurence. With a 700 mb (TdD) of (7 ° C) and a UI value of 4.0, the predicted region, Area 1, corresponds to an area too moist for downbursts, but thunderstorms may still develop, Caracena et al. (1983). This result suggests that the dynamics of this downburst may be different than other studies since different mechanisms may be responsible for this storm.

The synoptic situation, see Fig. (3.4), for the 1649 MDT, 14 July 1982 case is considerably different than the 5 August 1982 case. The synoptic scale trigger was a rapidly moving cold front that passed through the domain of interest at 1800 MDT.

The Denver sounding, released at 1800 MDT, 14 July 1982 is graphically presented in Fig. (3.5). The dry layer extends to a height comparable to the 5 August case, but the surface mixed layer has an average mixing ratio of 4.5 g/Kg for the 1649 MDT, 14 July case, while a value of 6.5 g/Kg occurred in the 5 August case. The depth of the moist layer is 3 km for the 5 August case, while it is approximately 1.5 km thick in the 14 July case. Both soundings were conditionally unstable with little lift required or increase of temperature necessary to

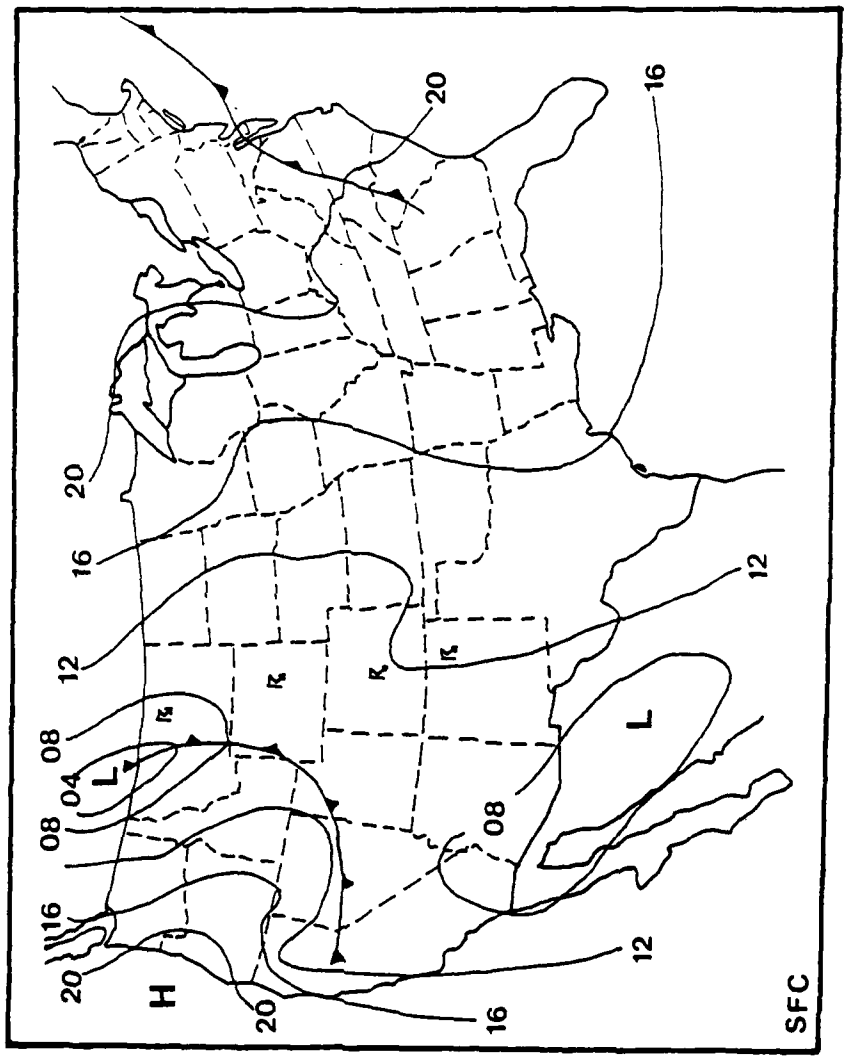

Fig. 3.4 Same as Fig. 3.2, except for 14 July 1982.

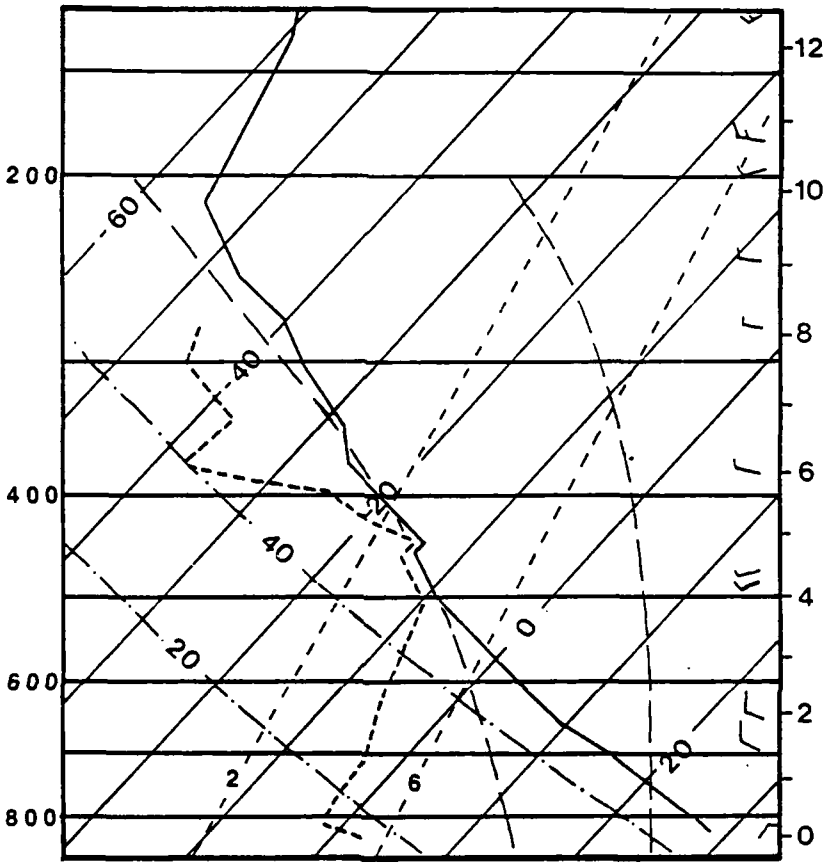

Fig. 3.5 Same as Fig. 3.3, except for 14 July 1982.

induce convection. The TdD was (18 ^{o} C) and the UI was 3.0. Therefore, a microburst event is predicted in this case with wind gusts greater than 40 knots. Of additional interest is the difference in the wind profile. The 5 August case features winds backing sharply with height in the boundary layer, while the 14 July case has little directional shear in the boundary layer.

3.2 Data Reduction and Analysis

Raw Doppler data are commonly archived for the researcher in unified format (UF), Barnes (1973). The data must be properly processed to minimize error and extract the real physical information. Lin and Pasken (1982) outlined the various stages in processing Doppler data: 1) Desired data are extracted and archived according to time and altitude. 2) Datum are converted from a spherical coordinate system to an orthogonal system. 3) Values exceeding pre-set tolerances are eliminated and "folded" radial velocities are corrected. 4) A spatial scattering of data contained in a given space is interpolated to a two-dimensional grid array. 5) The three-dimensional wind field is computed from the gridded fields of reflectivity and two-dimensional radial velocity. 6) Thermodynamic retrieval is performed and finally, 7) These data are displayed.

3.2.1 Data Reduction of the Initial Data Field

The data consist of azimuth sweeps subtending approximately 90 deg. of arc. Data falling outside the area affecting the domain of interest is deleted by extracting the proper sequence of rays. Next, the data were converted from spherical coordinates relative to the source radar to orthogonal coordinates relative to one radar (CP-2).

The datum are advected to a common time near the midpoint of the data collection cycle using storm's horizontal motion. Editing of data is accomplished using velocity thresholds predicted by Doppler wave propagation and a lower limit on data resolution as a function of the returned signal. The resultant datum were sliced into slabs centered on a vertical level of interest. The slabs are then horizontally interpolated to the grid points by use of the Barnes (1973) scheme. The data points are then vertically interpolated to the specified horizontal plane.

3.2.2 Conversion of Radial Velocity to Cartesian Components

The processed data are now composed of two radial velocities (from the two radars) and the radar reflectivity, which can be related to vertical velocity as will be discussed further. A scheme relating radial velocity to the three Carte-

sian components was proposed by Armijo (1969) and has been used by Brandes (1977, 1978), Lin and Pasken (1982), Lin et al. (1986) and Lin et al. (1987) in their studies. The scheme is governed by the following equations:

$$V_{R1} = \frac{(x-x_1) + v(y-y_1) + (w+V_t)(z-z_1)}{R_1} \qquad \text{Eq. (3.1)}$$

$$V_{R2} = \frac{u(x-x_2) + v(y-y_2) + (w+V_t)(z-z_2)}{R_2} \qquad \text{Eq. (3.2)}$$

where R_1 is the radial distance from radar 1 to target, R_2 is the radial distance from 2 to target, Vr1 is the radial velocity measured by radar 1, Vr2 is the radial velocity measured by radar 2, (u,v,w) are the components of the true wind in the x,y,z directions, in order, (x,y,z) is the actual location of the target with respect to (w.r.t.) the origin, (x1,y1,z1) is the location of radar 1 w.r.t. the origin, (x2,y2,z2) is location of radar 2 w.r.t. origin and V_t is the mean terminal velocity of hydrometeors within the target volume.

The terminal fall speed is estimated using a formula for a high plains thunderstorm, Martner (1975), with a density-height correction of Foote and du Toit (1969), i.e.,

$$V_t = -5.70\, Z_e^{0.04} \left(\frac{\rho_{00}}{\rho_0(z)}\right)^{0.4} \qquad \text{Eq. (3.3)}$$

where $\rho_o(z)$ is the environmental air density, ρ_{oo} is the surface air density. Z_e is equivalent radar reflectivity factor. Finally, the anelastic continuity equation is:

$$\frac{\partial(\bar{\rho}_a(z)w)}{\partial z} = -\nabla_H \cdot (\bar{\rho}_a(z)\vec{\nabla}_H) \qquad \text{Eq. (3.4)}$$

where $\rho_a(z)$ is the air density in an adiabatic-hydrostatic atmosphere.

The equations in this section comprise the equations which can be solved for the three-dimensional wind field if the boundary value of w is known. The continuity equation may be solved for the vertical velocity at the upper level and subsequently integrated upward. The resultant equation consists of:

$$W(up) = \frac{\bar{\rho}_{a(lwr)(z)}}{\bar{\rho}_{a(up)(z)}} W(lwr) - \frac{\bar{\rho}_{(ave)(z)}}{\bar{\rho}_{a(up)(z)}} (\nabla_2 \cdot \vec{\nabla}_H) \Delta z \qquad \text{Eq. (3.5)}$$

Since the depth of the analysis domain is only 1.25 km, the accumulation of error is negligible (Lin et al., 1986).

3.3 Thermodynamic Retrieval of Pressure and Temperature

This study will use a moving coordinate system. Studies by Chong et al. (1980), Hane et al. (1981) and Gal-Chen (1982) demonstrated that it is necessary to use a storm-relative coordinate system. The momentum equations used by Gal-Chen (1978)

to compute the perturbation pressure are as follows:

$$\frac{\partial P'}{\partial x} = F \qquad \text{Eq. (3.6)}$$

$$\frac{\partial P'}{\partial y} = G \qquad \text{Eq. (3.7)}$$

$$\frac{\partial P'}{\partial z} = -H - \rho' g \qquad \text{Eq. (3.8)}$$

where F, G and H are defined as:

$$F = -\bar{\rho}_a \vec{\nabla} \cdot \nabla u + \left(\frac{\partial \tau_{1i}}{\partial x_i}\right)_{i=1,2,3} + \bar{\rho}_a 2\Omega (v \sin\phi - w \cos\phi) \qquad \text{Eq. (3.9)}$$

$$G = -\bar{\rho}_a \vec{\nabla} \cdot \nabla u + \left(\frac{\partial \tau_{2i}}{\partial x_i}\right)_{i=1,2,3} - \bar{\rho}_a 2\Omega u \sin\phi \qquad \text{Eq. (3.10)}$$

$$H = \bar{\rho}_a \vec{\nabla} \cdot \nabla w - \left(\frac{\partial \tau_{3i}}{\partial x_i}\right)_{i=1,2,3} - \bar{\rho}_a 2\Omega u \cos\phi + \rho_a g \qquad \text{Eq. (3.11)}$$

The variables include ρ' as the perturbation density, p' is the perturbation pressure, ρ_a is the hydrostatic atmosphere, which is roughly equivalent to the environmental density (Brandes, 1984; Lin et al., 1986) and τ_{1i}, τ_{2i} and τ_{3i} are turbulent momentum fluxes.

The turbulent momentum flux terms, τ_{ij}, are computed in a manner described in Appendix A.

From Smagorinsky (1963), the eddy viscosity coefficient is

$$K_M = \frac{c^2 \ell^2}{\sqrt{2}} \left| \frac{\partial u_i}{\partial x_j} + \frac{\partial u_j}{\partial x_i} \right| \qquad \text{Eq. (3.12)}$$

Finally, the precipitation drag term, q_1 from Eq. (3.11) is estimated by relating liquid water content to reflectivity as derived by Kessler (1969), i.e.,

$$q_l = \left\{ \frac{Z\,(mm\,m^{-3})}{a} \right\}^{1/b} \qquad \text{Eq. (3.13)}$$

where b = 1.75 and a = 1.73×10^4 .

Once the values for precipitation drag and turbulent momentum fluxes are calculated, Eqs. (3.9 - 3.11) can be solved for the horizontal perturbation pressure. This involves solving the following Poisson partial differential equation resulting from differentiating Eq. (3.6) with respect to x and Eq. (3.7) with respect to y:

$$\frac{\partial^2 P'}{\partial x^2} + \frac{\partial^2 P'}{\partial y^2} = \frac{\partial F}{\partial x} + \frac{\partial G}{\partial y} \qquad \text{Eq. (3.14)}$$

Using sequential relaxation and the following Neumann boundary conditions yields:

$$\frac{\partial P'}{\partial x} = F \; ; \; at \; x = \pm a$$

$$\frac{\partial P'}{\partial y} = G \; ; \; at \; y = \pm b$$

A unique solution to Eq. (3.14) exists if the horizontal area mean <P'> of P' is subtracted from P'.

Perturbation density is recovered using the following equation:

$$(\rho' - \langle \rho' \rangle) g = \frac{-\partial P_d}{\partial z} - (H - \langle H \rangle) \qquad \text{Eq. (3.15)}$$

where the quantities of the form <> represent areal means which are height-dependent only. The perturbation density, ρ'_d, and perturbation pressure are used to compute the deviation perturbation virtual temperature from the perturbation equation of state:

$$T_{vd}' = \left(\frac{P_d'}{\bar{P}} - \frac{\rho'}{\bar{\rho}} \right) \left(\frac{\bar{P}}{R_d \bar{\rho}} \right) \qquad \text{Eq. (3.16)}$$

3.4 Verification of the Retrieved Thermodynamic Data

The Gal-Chen (1978) method is indirect, thus verification will be necessary. By use of momentum checking and continuity, Gal-Chen and Hane (1981) suggested a method for calculating a correlation factor for each analysis level. A non-dimensional factor, Er, is calculated for the relative error as follows:

$$E_r = \frac{\iint \left\{ \left(\frac{\partial P_d'}{\partial x} - F \right)^2 + \left(\frac{\partial P_d'}{\partial y} - G \right)^2 \right\} dx dy}{\iint (F^2 + G^2) dx dy} \qquad \text{Eq. (3.17)}$$

Gal-Chen and Hane (1981) predicted that values of Er>.5 were "noise", while Er<.5 were scientifically meaningful. But, Hane and Ray (1985) showed that values of Er>.5 may still

contain useful information. This method was used by many authors. Kropfli (1984), Roux et al. (1984), Brandes (1984), Hane and Ray (1985) and Lin et al. (1986) have used this method to verify the retrieved fields. Momentum checking is important since the physical structures of the storm should agree with fields of divergence/convergence and vertical motion. Momentum flux reveals the fit of the retrieved data.

3.5 Calculation of the Turbulent Dynamics

Subsynoptic-scale motion within convective cells contains non-hydrostatic processes. Synoptic-scale kinetic energy budgets studied by Kung and Tsui (1975) and Ward and Smith (1976) can not be used in this study. This study considers a three-dimensional kinetic energy budget for turbulent processes occurring in the surface at 1.25 km layer in a microburst and surrounding mesoγ-scale environment.

In the Doppler data processing, a three-dimensional wind field within a convective cell can be synthesized from multiple-Doppler data. This wind field can be inputed for calculating fields of deviation pressure and temperature perturbations, P'_d and T'_d, using the method developed by Gal-Chen (1978). Data resolution for the JAWS case was 0.5 km in the horizontal and 0.25 km in the vertical. Fine resolution data

allow investigation of eddy phenomenon such as the momentum and eddy energy budget. Doppler data's advantage over aircraft data is that Doppler data are nearly simultaneously scanned so the data are more temporally accurate.

Values of the three Cartesian wind components (u,v,w) at gridpoints can be used to calculate the mean component (u,v,w) and perturbation (u',v',w') quantities. The retrieved thermodynamic perturbation quantities were derived from their area means, i.e.,

$$P'd = P' - \langle P' \rangle; \quad Tv'd = T'v - \langle T'v \rangle$$

not the environmental mean state. However, the derived thermodynamic perturbations can replace the actual perturbation quantities.

3.5.1 Calculation of the Turbulent Kinetic Energy Equations

The development of the turbulent kinetic energy begins with the derivation of the energy equation for mean motion. Recall that the Reynolds' stress tensor is given by:

$$\tau_{ik}^{*} = -\rho \overline{u_i' u_k'} \qquad \text{Eq. (3.18)}$$

and the molecular stress tensor is:

$$\tau_{ik} = -p \delta_{ik} + M_{ik} \qquad \text{Eq. (3.19)}$$

The Kronecker constant, δ_{iK} is valued as:

$$\begin{cases} 1 & \text{if } i=K \\ 0 & \text{if } i\neq K \end{cases}$$

Additionally,

$$\text{Mik} = \mu\left\{\left(\frac{\partial u_i}{\partial x_K}+\frac{\partial u_K}{\partial x_i}\right)-\frac{2}{3}\delta_{iK}\left(\frac{\partial u_j}{\partial x_j}\right)\right\},$$

$$\text{deformation tensor} = \frac{\partial u_i}{\partial x_K}+\frac{\partial u_K}{\partial x_i},$$

$$\text{static pressure, } P = -\frac{1}{3}(\tau_{xx}+\tau_{yy}+\tau_{zz}),$$

$$\text{individual change, } D/Dt = \frac{\partial}{\partial t}+\bar{u}_K\frac{\partial}{\partial x_K}, \text{ and}$$

finally, the Reynolds' equations for mean motion in tensor form is given by Eq. (3.20):

$$\bar{\rho}\frac{D\bar{u}_i}{Dt}+2\varepsilon_{ijK}f_j\bar{\rho}\bar{u}_K\bar{u}_L=-\bar{\rho}\frac{\partial\bar{\Phi}}{\partial x_i}+\frac{\partial}{\partial x_K}\left(\bar{\tau}_{iK}+\tau^*_{iK}\right) \qquad \text{Eq. (3.20)}$$

Note that at the meso γ-scale, the Coriolis term, $2\varepsilon_{ijk}f_j\bar{\rho}\bar{u}_k\cdot\bar{u}_i=0$. By using scale analysis, Euler's expansion and the chain rule, the equation may be transformed into:

$$\bar{\rho}\frac{\bar{D}}{\bar{D}t}\left(\frac{1}{2}\bar{u}_i^2+\Phi\right)=\frac{\partial}{\partial x_K}\left(\bar{\tau}_{iK}\bar{u}_i+\tau^*_{iK}\bar{u}_i\right)-\left(\bar{\tau}_{iK}+\tau^*_{iK}\right)\frac{\partial\bar{u}_i}{\partial x_K} \qquad \text{Eq. (3.21)}$$

where the term on the right hand side (RHS) of Eq. (3.21) is the rate per unit volume at which the mean total apparent stresses do work on the mean motion, and the total rate of transformation per unit volume of mechanical energy of mean motion into other forms of energy, respectively.

The eddy form of the kinetic energy equation results from multiplying Eq. (3.21) by U to yield:

$$\underbrace{\frac{\partial}{\partial t}\left(\frac{\overline{\rho u_i^2}}{2}\right)}_{A} + \underbrace{\frac{\partial}{\partial x_K}\left(\frac{\overline{\rho u_i^2 u_K}}{2}\right)}_{B} = -\rho \underbrace{\overline{u_i \frac{\partial \Phi}{\partial x_i}}}_{C} + \underbrace{\overline{u_i \frac{\partial \tau_{iK}}{\partial x_K}}}_{D} \qquad \text{Eq. (3.22)}$$

The terms of Eq. (3.22) can be expanded by dividing the total variable into a mean and a perturbed quantity. The expanded terms are combined to form a new equation. The equation for the mean motion kinetic energy, Eq. (3.20), is subtracted from the new equation, which results in the eddy kinetic energy equation:

$$\begin{aligned}\underbrace{\bar{\rho}\frac{\bar{D}}{Dt}\left(\frac{1}{2}\overline{u_i'^2}\right)}_{(A)} &= \frac{\partial}{\partial t}\left(\frac{\overline{\rho u_i'^2}}{2}\right) + \frac{\partial}{\partial x_K}\left\{\frac{\overline{\rho u_i^2 u_K}}{2}\right\} \\ &= \underbrace{-\overline{\rho u_i}\frac{\partial \Phi}{\partial x_i}}_{(B)} + \underbrace{\tau_{iK}^*\frac{\partial \bar{u}_i}{\partial x_K}}_{(C)} + \underbrace{\frac{\partial}{\partial x_K}\left(\overline{u_i'\tau_{iK}'}\right)}_{(D)} + \\ &\quad \underbrace{-\overline{\tau_{iK}'\frac{\partial u_i'}{\partial x_K}}}_{(E)} - \underbrace{\frac{\partial}{\partial x_K}\left(\frac{1}{2}\overline{\rho u_i'^2 u_K'}\right)}_{(F)}\end{aligned} \qquad \text{Eq. (3.23)}$$

The above equation is the equation for the mean rate of change in the mechanical energy of the eddying motion, per unit volume. The physical meaning of each of the terms is given as follows: A = the rate of change of mean turbulent kinetic energy, per unit volume, B = the work rate of the geopotential field on the eddy flux of mass arising from the degree of correlation between the density and velocity perturbation (i.e., buoyancy production term), C = energy cascade effect of mechanical energy conversion to the eddy state from the mean state (i.e., work done by the Reynolds' stress terms), D = the mean rate at which the eddying energy is changing from work done by dissipation, E = the mean rate of transformation of

eddying energy into heat and internal energy, and F = the rate of loss of eddying energy, per unit volume, by eddying diffusion.

The molecular stress factor and Mik are known and so substitution into Eq. (3.23) yields:

$$\bar{\rho}\frac{D}{Dt}\left(\tfrac{1}{2}\overline{u_i'^2}\right) = \underbrace{-\overline{\rho' u_i'}\frac{\partial \bar{p}}{\partial x_i}}_{A} + \underbrace{\bar{\tau}_{ik}^{*}\frac{\partial \bar{u}_i}{\partial x_k}}_{B} \underbrace{- \overline{u_i'\frac{\partial p'}{\partial x_i}}}_{C} + \underbrace{\frac{\partial}{\partial x_k}\left(\overline{m_{ik}u_i'}\right)}_{D} \qquad \text{Eq. (3.24)}$$

$$\underbrace{-\overline{m_{ik}\frac{\partial u_i}{\partial x_k}}}_{E} - \underbrace{\frac{\partial}{\partial x_k}\left(\tfrac{1}{2}\bar{\rho}\overline{u_i^2 u_k'}\right)}_{F}$$

Several new terms appear after this derivation. Their physical meanings are in order as follows: C = the mean rate of work of the variable static pressure gradient, D = the mean work rate, per unit volume, by viscous stresses on the eddying motion, E = the mean dissipation rate, per unit volume, of eddy kinetic energy into heat (>0)

The three-dimensional mean eddy kinetic energy, per unit volume, may be written as:

$$\tfrac{1}{2}\bar{u}_i^2 = \tfrac{1}{2}\left(\overline{u'^2} + \overline{v'^2} + \overline{w'^2}\right) = E_T$$

The buoyancy term (A) can be rewritten as: Eq. (3.25)

$$-\overline{\rho' u_i'}\frac{\partial \bar{p}}{\partial x_i} = -\overline{\rho' w'} g$$

By recognizing:

$$\frac{\rho'}{\bar{\rho}} \approx \frac{-T_v'}{\bar{T}_v}$$

And solving for ρ', with substitution into Eq. (3.25), yield:

$$-\overline{\rho' u_i'} \frac{\partial \Phi}{\partial x_i} \approx \frac{\bar{\rho} g}{\bar{T}_v} \overline{T_v' w'} \left[-\bar{\rho} g \overline{q_l w'} \right] \qquad \text{Eq. (3.26)}$$

where T_v is the virtual temperature. The term in brackets represents the production or destruction of eddy kinetic energy due to precipitation loading.

Assume the mean flow is a function of height only so that the mean values are area averages and work done by the Reynolds' stresses are then described by:

$$\tau_{ik}^* \frac{\partial \bar{u}_i}{\partial x_k} = \tau_{i3}^* \frac{\partial u_i}{\partial x_3} = \tau_{xz}^* \frac{\partial \bar{u}(z)}{\partial z} + \tau_{yz}^* \frac{\partial \bar{v}(z)}{\partial z} + \tau_{zz}^* \frac{\partial \bar{w}(z)}{\partial z} \qquad \text{Eq. (3.27)}$$

The molecular dissipation terms can be grouped together as a single term:

$$DD = \frac{\partial}{\partial x_k} \left(\overline{M_{ik} u_i'} - \overline{M_{ik} \frac{\partial u_i'}{\partial x_k}} - \frac{\partial}{\partial x} \left(\frac{1}{2} \overline{\rho u_i'^2 u_k'} \right) \right) \qquad \text{Eq. (3.28)}$$

This term is calculated using perturbations from the area means and the frictional stresses are calculated in the same manner as in Appendix A. Substituting Eqs. (3.26-3.28) into Eq.

(3.24) yields the final form of the eddy kinetic energy budget equation:

$$\bar{\rho}\frac{\bar{D}}{Dt}\left(\tfrac{1}{2}\overline{u_i}^2\right) = \frac{\partial \overline{\rho E_T}}{\partial t} + \frac{\partial}{\partial x_k}\left\{\bar{\rho}\,\overline{E_T}\,\overline{u_k}\right\}$$

$$= \frac{\bar{\rho}g}{\overline{T_v}}\left\{\overline{T_v'w'}\right\} - \overline{\rho g q_l w'} + \qquad \text{Eq. (3.29)}$$

$$\left(\tau^*_{xz}\frac{\partial \bar{u}}{\partial z} + \tau^*_{xy}\frac{\partial \bar{v}}{\partial z} + \tau^*_{xz}\frac{\partial \bar{w}}{\partial z}\right) -$$

$$\left(\overline{u'\frac{\partial p'}{\partial x}} + \overline{v'\frac{\partial p'}{\partial y}} + \overline{w'\frac{\partial p'}{\partial z}}\right) + DD$$

The eddy quantities are calculated in exactly the same way as will be used in the momentum budget calculation. The Reynold's stresses calculated in the mean shear/turbulent interaction term were calculated using the direct method. The area average of the product of perturbation wind components multiplied by the environmental density constitutes the direct method. The turbulent dynamics of the subcloud layer may also be investigated in terms of a momentum budget that examines the role of eddy and mean momentum exchange. Results should prove useful in confirming results of the eddy kinetic energy budget and provide insight into physical processes not easily explained by energy transformations.

3.5.2 Calculation of the Vertical Momentum Flux

The local momentum flux terms are given by the following

equations:

$$\frac{\tau^*_{xz}}{\rho} = -\overline{u'w'} \qquad \text{Eq. (3.30)}$$

$$\frac{\tau^*_{yz}}{\rho} = -\overline{v'w'} \qquad \text{Eq. (3.31)}$$

These equations may be used to diagnose where momentum is transported within the storm. A vertical slice showing how the atmosphere transports available momentum may be constructed along a cross-section of interest.

The methodology used is outlined in the following steps:

1) Storm-relative winds were acquired by any gridpoint contacting the cross-section.

2) Nearby data points of u,v and w were linearly interpolated to the cross-section.

3) A string-average was taken of all the points on the cross-section unique to that level.

4) From the string-averaged mean, perturbations of u', v' and w' were computed.

The location of the cross-section is set to include the region of maximum rising motion and bisecting the microburst.

3.5.3 Calculation of the Momentum Budget

Momentum budgets on the convective scale have been con-

ducted by Moncrieff and Miller, 1976; Sanders and Emanuel, 1977; LeMone, 1983 . Previous research has utilized direct turbulent measurements by aircraft or model data. Coover (1986) and Condray (1987) utilized retrieved thermodynamic variables from dual-Doppler data. A similar methodology is employed.

The momentum budget equations for the total flow in a moving Cartesian coordinate system is formulated as:

$$\frac{\partial u}{\partial t} + u\frac{\partial u}{\partial x} + v\frac{\partial u}{\partial y} + w\frac{\partial u}{\partial z} = -\frac{1}{\rho}\frac{\partial p}{\partial x} + fv - fw^* + F_x \qquad \text{Eq. (3.32)}$$

$$\frac{\partial v}{\partial t} + u\frac{\partial v}{\partial x} + v\frac{\partial v}{\partial y} + w\frac{\partial v}{\partial z} = -\frac{1}{\rho}\frac{\partial p}{\partial y} - fu + F_y \qquad \text{Eq. (3.33)}$$

$$\frac{\partial w}{\partial t} + u\frac{\partial w}{\partial x} + v\frac{\partial w}{\partial y} + w\frac{\partial w}{\partial z} = -\frac{1}{\rho}\frac{\partial p}{\partial z} - g + f^*u + F_z \qquad \text{Eq. (3.34)}$$

The Coriolis force is at least one order of magnitude smaller than the larger terms of the above equations. It is frequently two orders of magnitude smaller at the mesoγ-scale and was not included in the budget calculation.

The turbulent component of the momentum budget may be extracted from the total flow by separating it into a mean component and the turbulent (perturbed) flow. The prime value is the perturbed part and the barred values are the mean components of the area of interest, which are calculated from the area mean. It is only a function of height. The variables of

(u,v,w,p,q) were likewise separated, which resulted in the following expansion of Eqs. (3.32-3.34).

$$\frac{\partial u'}{\partial t} + \bar{u}(z)\frac{\partial u'}{\partial x} + u'\frac{\partial \bar{u}}{\partial x} + \bar{v}(z)\frac{\partial u'}{\partial y} + \bar{w}(z)\frac{\partial \bar{u}}{\partial z} + w'\frac{\partial \bar{u}}{\partial z} + \bar{w}(z)\frac{\partial u'}{\partial z} + w'\frac{\partial u'}{\partial z} = \frac{-1}{\rho}\frac{\partial p'}{\partial x} + F_x \qquad \text{Eq. (3.35)}$$

$$\frac{\partial \lambda'}{\partial t} + \bar{u}(z)\frac{\partial \lambda'}{\partial x} + u'\frac{\partial \bar{\lambda}}{\partial x} + \bar{v}(z)\frac{\partial \lambda'}{\partial y} + v'\frac{\partial \bar{\lambda}}{\partial y} + \bar{w}(z)\frac{\partial \bar{\lambda}}{\partial z} + w'\frac{\partial \bar{\lambda}}{\partial z} + \bar{w}(z)\frac{\partial \lambda'}{\partial z} + w'\frac{\partial \lambda'}{\partial z} = \frac{-1}{\rho}\frac{\partial p'}{\partial y} + F_y \qquad \text{Eq. (3.36)}$$

$$\frac{\partial w'}{\partial t} + \bar{u}(z)\frac{\partial w'}{\partial x} + u'\frac{\partial w'}{\partial x} + \bar{v}(z)\frac{\partial w'}{\partial y} + v'\frac{\partial w'}{\partial y} + \bar{w}(z)\frac{\partial \bar{w}}{\partial z} + w'\frac{\partial \bar{w}}{\partial z} + \bar{w}(z)\frac{\partial w'}{\partial z} + w'\frac{\partial w'}{\partial z} = \frac{-1}{\rho}\frac{\partial \bar{p}}{\partial z} - \frac{1}{\rho}\frac{\partial p'}{\partial z} - g\bar{q}_l - gq_l' + F_z \qquad \text{Eq. (3.37)}$$

Substituting for $\partial P/\partial z$ from the hydrostatic equation results in:

$$\frac{\partial w'}{\partial t} + \bar{u}(z)\frac{\partial w'}{\partial x} + u'\frac{\partial w'}{\partial x} + \bar{v}(z)\frac{\partial w'}{\partial y} + v'\frac{\partial w'}{\partial y} + \bar{w}(z)\frac{\partial \bar{w}}{\partial z} + w'\frac{\partial \bar{w}}{\partial z} + \bar{w}(z)\frac{\partial w'}{\partial z} + w'\frac{\partial w'}{\partial z} = \frac{-1}{\rho}\frac{\partial p'}{\partial z} - \left(\frac{\rho'}{\rho}\right)g + F_z - g(\bar{q}_l - q_l') \qquad \text{Eq. (3.38)}$$

where the gravitational buoyancy term can be rewritten as:

$$-g\frac{\rho'}{\bar{\rho}} = g\left(\frac{T_v'}{\bar{T}_v}\right) - g\frac{p'}{\bar{p}} \qquad \text{Eq. (3.39)}$$

Schlesinger (1980) termed the quantities on the right side of Eq. (3.50) as the moist thermal buoyancy and the pressure buoyancy, respectively. The pressure buoyancy term is one order of magnitude less than the other terms so it is neglected. The u-momentum equation (3.35) is multiplied by w' and the w-momentum equation is multiplied by u'. The resultant equations are:

$$w'\frac{\partial u'}{\partial t} = -\bar{u}(z)w'\frac{\partial u'}{\partial x} = u'w'\frac{\partial u'}{\partial x} - \bar{v}(z)w'\frac{\partial u'}{\partial y} - v'w'\frac{\partial u'}{\partial y} - \bar{w}(z)w'\frac{\partial \bar{u}}{\partial z} - w'^2\frac{\partial u'}{\partial z} - w'^2\frac{\partial \bar{u}}{\partial z} - \bar{w}(z)w'\frac{\partial u'}{\partial z} - \frac{w'}{\bar{\rho}}\frac{\partial p'}{\partial x} + w'F_x \qquad \text{Eq. (3.40)}$$

$$u'\frac{\partial w'}{\partial t} = -\bar{u}(z)u'\frac{\partial w'}{\partial x} - u'w'\frac{\partial w'}{\partial x} - \bar{v}(z)u'\frac{\partial w'}{\partial y} - \bar{w}(z)u'\frac{\partial \bar{w}}{\partial z} - u'w'\frac{\partial \bar{w}}{\partial z} - \bar{w}(z)u'\frac{\partial w'}{\partial z} - u'w'\frac{\partial w'}{\partial z} + \frac{g}{\bar{T}_v}u'T_v' - g\,u'(\bar{q}_\ell - q_\ell') \qquad \text{Eq. (3.41)}$$

Adding Eq. (3.40) and Eq. (3.41) and performing the bar operation yields:

$$\frac{\partial \overline{u'w'}}{\partial t} = -\bar{u}(z)\frac{\partial \overline{u'w'}}{\partial x} - \overline{u'\frac{\partial u'w'}{\partial x}} - \bar{v}(z)\frac{\partial \overline{u'w'}}{\partial y} - \overline{v'\frac{\partial u'w'}{\partial y}} - \cancel{\overline{w'}(z)}^{\,0}\overline{w'}\frac{\partial \bar{u}}{\partial z} - \cancel{\overline{w}(z)}\,\overline{u'}\frac{\partial \bar{u}}{\partial z} - \overline{w'^2}\frac{\partial \bar{u}}{\partial z} - \overline{w'\frac{\partial u'w'}{\partial z}} - \bar{w}\frac{\partial \overline{u'w'}}{\partial z} + \frac{g}{\bar{T}_v}\overline{u'T_v'} - g\overline{u'q_\ell} - \left(\frac{\overline{w}}{\bar{\rho}}\frac{\partial p'}{\partial x} + \frac{\overline{u'}}{\bar{\rho}}\frac{\partial p'}{\partial z}\right) \qquad \text{Eq. (3.42)}$$

The terms may be expanded to a final form:

$$\frac{\partial \overline{u'w'}}{\partial t} = -\bar{u}(z)\frac{\partial \overline{u'w'}}{\partial x} - \overline{u'\frac{\partial u'w'}{\partial x}} - \bar{v}(z)\frac{\partial \overline{u'w'}}{\partial y} - \overline{v'\frac{\partial w'w'}{\partial y}}$$

$$-\bar{w}(z)\overline{w'\frac{\partial u'}{\partial z}} - \bar{w}(z)\overline{u'\frac{\partial w'}{\partial z}} - \overline{w'^2}\frac{\partial \bar{u}}{\partial z} -$$

$$\overline{w'\frac{\partial u'w'}{\partial z}} - \bar{w}\overline{\frac{\partial u'w'}{\partial z}} + \frac{g}{\bar{T}_v}\overline{u'T_v'} - \overline{gu'q'} \qquad \text{Eq. (3.43)}$$

$$-\left(\overline{\frac{w'}{\rho}\frac{\partial p'}{\partial x}} + \overline{\frac{u'}{\rho}\frac{\partial p'}{\partial x}}\right)$$

or

$$\underset{A}{\frac{\partial \overline{u'w'}}{\partial t}} = \underbrace{-\overline{w'^2}\frac{\partial \bar{u}}{\partial t}}_{B} - \underbrace{\frac{1}{\bar{\rho}}\frac{\partial}{\partial z}\left(\bar{\rho}\overline{u'w'^2}\right)}_{C} + \underbrace{\frac{g}{\bar{T}_v}\overline{u'T_v'}}_{D} - \underbrace{g\overline{u'q'}}_{I} -$$

$$\underbrace{\left(\overline{\frac{w'}{\rho}\frac{\partial p'}{\partial x}} + \overline{\frac{u'}{\rho}\frac{\partial p'}{\partial z}}\right)}_{E} - \underbrace{\left[\frac{\partial}{\partial x}\left(\bar{u}\overline{u'w'}\right) + \frac{\partial}{\partial x}\left(\overline{u'^2w'}\right)\right]}_{F} - \qquad \text{Eq. (3.44)}$$

$$\underbrace{\left[\frac{\partial}{\partial y}\left(\bar{v}\overline{u'w'}\right) + \frac{\partial}{\partial y}\left(\overline{u'v'w'}\right)\right]}_{G} - \frac{1}{\bar{\rho}}\underbrace{\left[\frac{\partial}{\partial z}\left(\bar{w}\bar{\rho}\overline{u'w'}\right)\right]}_{H}$$

where term A = the local time change of u-momentum flux,

term B = the mechanical production of u-momentum flux from vertical mean shear,

term C = a source of momentum flux from the vertical transport of u-momentum flux,

term D = buoyancy production term,

term E = production and destruction of eddy stress by velocity-pressure interactions,

term F = a source of momentum flux from the horizontal divergence of u-transport,

term G = a source of momentum flux from the horizontal

divergence of v-transport,

term H = a source of momentum flux from the vertical divergence of w-transport, and

term I = the effect of precipitation loading.

The v-momentum flux may be derived in a similar manner with the following result:

$$\frac{\partial \overline{v'w'}}{\partial t} = -\overline{w'^2}\frac{\partial v}{\partial z} - \frac{1}{\bar{\rho}}\frac{\partial}{\partial z}\left(\bar{\rho}\,\overline{v'w'^2}\right) - \frac{g}{\bar{T}_v}\overline{v'T_v'} - \left(\overline{\frac{w'}{\bar{\rho}}\frac{\partial p'}{\partial y}} - \overline{\frac{v'}{\bar{\rho}}\frac{\partial p'}{\partial z}}\right) - \left[\frac{\partial}{\partial x}\left(\bar{u}\overline{v'w'}\right) + \frac{\partial}{\partial x}\left(u'v'w'\right)\right] - \frac{1}{\bar{\rho}}\left[\frac{\partial}{\partial z}\left(\bar{w}\bar{\rho}\overline{v'w'}\right)\right] - g\overline{v'q_\ell'} \qquad \text{Eq. (3.45)}$$

3.5.4 Calculation of the Momentum Budgets from Dual-Doppler Data

Momentum budgets have used either direct turbulent measurements using aircraft or model generated output. The perturbation quantities are not directly measured by dual-Doppler radar. They are indirectly measured by using geometrically synthesized wind fields, and assuming an appropriate divergence profile, to retrieve thermodynamic variables. The retrieved perturbation quantities are shown to be equivalent to the directly measured variables as shown:

$$p'_d \cong p' - \langle p' \rangle \; ; \; p' = p'_d + \langle p' \rangle$$

$$T'_{vd} = T'_v - \langle T_v \rangle \; ; \; T'_v = T'_{vd} + \langle T_v \rangle$$

$$\overline{\frac{v'}{\bar{\rho}}\frac{\partial p'}{\partial z}} = \overline{\frac{v'}{\bar{\rho}}\frac{\partial}{\partial z}\left(p'_d + \langle p' \rangle\right)} = \frac{\overline{v'}}{\bar{\rho}}\frac{\partial p'_d}{\partial z} + \frac{\overline{v'}}{\bar{\rho}}\cancel{\frac{\partial}{\partial z}\langle p' \rangle}^{\,0}$$

The terms of the momentum budget were calculated using finite differencing techniques. Centered differencing was used

in the nested grid of choice over the microburst, but some one-sided differences were used at the edges of the large domain of interest.

4. Error Analysis

Error analysis and interpretation are essential when using real data. Real data are subject to errors during collection, processing and parameterization of physical processes, which may not be totally representative of the real storm structure. An analysis of possible error sources and their impact on the results is therefore necessary to estimate the validity of this research.

Error sources are of a random and non-random nature. Random errors include ground clutter, inadequate sampling, inadequate temporal synchronizing of the radars, side lobe contamination, and signal processing uncertainty. Random errors are non-systematic; therefore, it is virtually impossible to detect and correct errors in the Unified Format (UF) data because of initial data signal processing and editing. Non-random errors are more likely to be present in the data processing conducted during this research, from the use of boundary conditions, finite differences methods, and errors in calculated fields derived from errors or inadequately resolved features in the wind field.

4.1 Random Error

Many researchers, Bohne and Srivastava (1976), Doviak et al. (1976), Ray et al. (1978,1980), Nelson and Brown (1982), Parsons et al. (1983), Wilson et al. (1984) and Lin, Wang and Lin (1986), have quantified random errors in the Doppler radar wind data. All the researchers concluded that errors in the three-dimensional wind field were < +3 m/s. Doviak et al. (1976) estimated errors in the wind field of ten degrees in direction and 1 m/s in speed. Lin and Pasken (1982), Elmore (1982) and Nelson and Brown (1982) obtained comparable results. Ray et al. (1978) found that targets located within 40 km of the radars have a standard deviation of horizontal wind uncertainty of < .2 m/s. Wilson et al. (1984) assumed a value of unity for the radial velocity variance from both radars and also the terminal velocity variance to show that the combined error due to statistical uncertainty in the radial velocity estimates and geometric configuration are approximately 1-2 m/s in the derived horizontal wind.

Random errors in velocity data are induced by variance in the probability density of the assumed drop-size distribution. This problem is impossible to quantify, since the drop-size distribution is unique to each storm, even if it tends to follow a best-fit curve, and no direct measurements are available.

4.2 Non-random Errors

Non-random errors may be classified as error due to limiting assumptions and from calculation techniques, as outlined by Hughes (1986).

Limiting assumptions include the choice of terminal velocity-reflectivity relationship, the adiabatic-hydrostatic assumption on density, and the quasi-steady state assumption.

4.2.1 Quasi-steady State Assumption

Dual-doppler radar were synchronized to scan the same storm volume at the same time. This condition was met for the 5 August case and any error is believed negligible. The 14 July 1982 data, where data collection was synchronized, still may have error since the radars were not scanning the exact space per time. The error would result as a difference of data resolution between the radars, which is mitigated to a large extend by use of the Barnes' scheme (1973).

In addition to resolution differences, error may result due to non-linear growth or decay of the storm structure during the scanning sequence. The observation time should be reduced to as small a value as possible. A mean correction time is assigned as the center value of the scanning sequence. As Gal-

Chen (1982) suggested, a linear forward or backward temporal advection correction is employed. This condition requires a non-accelerating storm motion and a minimum amount of temporal change in storm development.

The non-accelerating storm motion condition is generally satisfied as revealed by Wilson et al. (1984). The 5 August 1982 storm appears to drift to the west at 1-2 m/s. This speed is of the same magnitude as the 14 July 1982 case. The temporal change requirement requires an assumption of constant or linear growth/decay of the storm. While temporal growth is likely to be non-linear in a microburst-producing convective storm, it apparently does not introduce unacceptable error for a two minute scan time. This assumption has been successfully employed by Lin and Hughes (1987), Wirsing (1985) and Lin and Pasken (1982).

4.2.2 Errors Associated with the Wind Field

Errors in this category include formulation of the terminal velocity equation with its dependence on the Foote and du Toit correction scheme for computing drop fall speed. Subjective analysis reduces known error by substituting a realistic datum. Since the datum is not known but approximated by use of contoured typical values known to occur in its vicinity, error

remains.

The terminal velocity-reflectivity relationship of Martner (1975) is used since it is a solution for a high-plains thunderstorm. Hughes (1986) showed that errors will be one order of magnitude smaller than the values of the u and v wind components. He also showed that the error is larger at greater elevation angles. The errors related to Foote & du Toit are also significant above 2 km AGL.

Subjective error in the wind field can not be quantified. Fortunately, few data points were in the 14 July 1982 data set and no subjective correction was used in the 5 August 1982 data. The method employed was to apply restrictive criteria to the selection of replacement values. Inconsistent values that resulted in large errors in thermodynamic retrieval, were replaced with data consistent with the contoured values of non-affected datum points.

4.2.3 Errors in the Derived Thermodynamic Fields

Errors in the pressure field comes from error in the wind field and the value of the mean pressure as defined by the data field. The effect of a 10% error in the wind field on the perturbation field was examined by Pasken (1981). He found that

the error in the wind field is directly proportional to the error in the resultant pressure field. The mean values of pressure per level were zero. This satisfies the condition of $\langle p' \rangle = 0$, Gal-Chen (1978). Lin et al. (1986) determined that exclusion of the local time tendency term did not reduce the accuracy of pressure recovery.

The retrieved perturbation temperature field is more sensitive to error than the perturbation pressure field. Hane et al. (1981) found that this calculation is not only subject to random error, but may produce an average error of 1 deg. by unresolved features in the wind field. Results also indicated that the temperature field was significantly affected by the elimination of the local time derivative.

4.2.4 Error in the Calculation of the Eddy Kinetic Energy Budget and the Momentum Budget Equations

Positive sources of error in these calculations include error in finite difference calculation, applicability of the mean value of the grid wind field to the environmental wind and the parameterization of the frictional eddy stresses.

The finite differencing used was fourth-order on interior points with centered and one-sided differencing used only on

the grid edges. The use of fourth-order differencing maximizes the data resolution and minimizes space truncation error.The mean value of the wind was determined from the grid. The grid derived mean wind was comparable in magnitude and direction to the sounding wind. Little if any error is likely to be introduced, because the 5 August 1982 grid contains nearly 1000 grid points and the 14 July 1982 grid contains 400 grid points over areas of 225 and 100 km, respectively. Frictional parameterization will introduce error, but results from Lin and Condray (1987) and Pan (1987) suggest that physically meaningful results can still be obtained.

Finally, Waldteufel (1976) and Doviak and Zrnic (1984) suggested, and Hughes (1986) showed that a 10% to 15% total error in the wind field is acceptable for accurate results in thermodynamic retrieval. He also showed that errors in reflectivity were significant in areas of high (> 40 dBz) areas of reflectivity.Such an error would be of significance in the rain water loading term of the perturbation-pressure equation, Gal-Chen (1978). However, the vertical deviation perturbation-pressure gradient term dominates the buoyancy equation with rain water loading only - 10% of the main term. Therefore, even a 100% error in the rain water loading term will result in a 10% error in the pressure calculation. The temperature calculation will be more directly affected. Spahn and Smith (1976)

found that the discrepancy between the calculated reflectivity, based on an actual measurement of hail, and the reflectivity calculated from the CP-2 radar was in fairly good agreement with a maximum difference of 10 - 15%. Previous research by Pasken (1981) showed that error in input data, e.g., wind data, is directly proportional in magnitude and sign to the thermodynamically retrieved variable. This result was verified by Hughes (1986). For a more complete discussion on scale analysis arguments, see Appendix B.

The result of acceptable data quality and lack of growth in the error after repeated calculations is physically realistic output.

5. Objectives

Thermodynamic retrieval provided perturbation pressure fields are used to examine the role of the three-dimensional pressure gradient in the maintenance and evolution of several wet microbursts. It is postulated that the strong outflow and downdrafts associated with the microbursts are directly related to the strength of the perturbation-pressure gradient. The downdraft itself is hypothesized to be maintained by precipitation loading in the high humidity environment of a wet microburst. Since vertical velocity is calculated independent of reflectivity, a positive correlation between the two fields will provide support to this theory. The perturbation pressure fields are theorized to maintain the outflow in a microburst. Eddy kinetic energy budgets and momentum budgets may be used as tracers to examine how momentum and kinetic energy transfers and conversions effect and maintain the evolution of microbursts. The outflow is postulated to interact with other outflows to form gust fronts, which may produce additional convective updrafts. A link between the microburst outflow, new convective updrafts and the initiation of microbursts will be examined. Since two cases, 5 August 1982 and 14 July 1982, are examined, useful comparisons may be made.

It is theorized that warm core microburst events are maintained by strong downdraft speeds of more than 7-8 m/s in the boundary layer in a wet microburst, due to the lack of evaporative cooling. By comparing a microburst containing strong downdraft speeds, 14 July 1982 case, with one containing downdraft speeds of 3-4 m/s, 5 August 1982 case, it is hypothesized that the weaker case should contain a weaker warm core structure or perhaps even a cold core structure. Additionally, microburst propagation is postulated to occur as discrete events organized by interactions between a microburst's perturbation-pressure forces and the updrafts thought to be associated with them. By examining the case of a single microburst, 14 July 1982, to one with multiple microbursts, 5 August 1982, similarities and differences in storm evolution may provide clues as to whether there is a common method of microburst propagation.

The microburst episodes considered occurred on 14 July 1982 and 5 August 1982. Data were collected from 164615-164915 MDT on 14 July 1982 and 1843-1851 MDT (Mountain Daylight Time) with data temporally corrected to 1647,1649 MDT and 1845,1850 MDT. Due to shallow scan heights of 9 deg. or less, vertical data resolution was limited to a 2 km AGL (Above Ground Level) scan. Data analysis and reduction procedures similar to those of Lin et al. (1986) and Hughes (1986) will be used to derive a three-dimensional wind field and thermodynamic variables.

Budgets of eddy kinetic energy and momentum fluxes at four analysis times will be calculated based on the derived wind, pressure and temperature fields.

By comparing budgets for different microburst occurrences, common structures and processes may be identified. Differences may also be identified and the forcing mechanisms may be found. The ultimate goal is to test a current hypothesis of microburst structure and development to devise a clearer model of what physical processes are the major contributors to the microburst development and what circulations may result.

6. Results

An analysis of two separate boundary layers containing microbursts was conducted during this research. The results indicated that the 14 July 1982, 1649 MDT case consisted of one large microburst emanating from a single parent storm; whereas, the 5 August 1982, 1845 and 1850 MDT cases revealed the presence of multiple microburst events. These two storms may be further categorized as a quasi-steady state microburst, 14 July 1982 case, and an evolving cluster of microbursts, the 5 August 1982 case, with the latter case containing a microburst in genesis. Other differences examined during this research include the role of terrain and the possible consequences of the presence of hail. The results are addressed in two parts. The first part is an analysis of the kinematic and dynamic features and the second section deals with the dynamics revealed by the momentum and eddy kinetic energy budgets. The following section will describe the boundary layer for the relatively simple case of a single, quasi-stationary microburst event, 14 July 1982 case to the complex case of a multiple microburst event, 5 August 1982, in varying stages of development.

6.1 Simple Case: An Analysis of the Kinematics for the 14 July 1982 Case

The first microburst event described will be the simple case. The lack of interactions between microbursts and the dominance of the microburst dynamics over the environmental flow assures a clearer picture of the physical mechanisms at work. It also provides a conceptual framework to compare and contrast the complex case with. The analysis will be conducted by examining the horizontal levels for structural features and continuity of the features through the boundary layer.

6.1.1 Plan View for the 14 July 1982, 1649 MDT Case

The plan view of the 0.25 km horizontal wind and reflectivity field, Fig. 6.1, reveals a symmetric microburst with the center located in the bow echo, high reflectivity region of reflectivities greater than 45 dBz. A strong gust front is noted northeast of the center (dashed line), and a weaker one is located west of the microburst center. The strongest winds occur between the microburst center and the strong gust front to the east of the center. The area of strongest winds east of the center is coincident with the location of Standley Lake, Colorado. At the east edge of this area, an area of strong convergence occurs in a weak echo region of reflectivities less

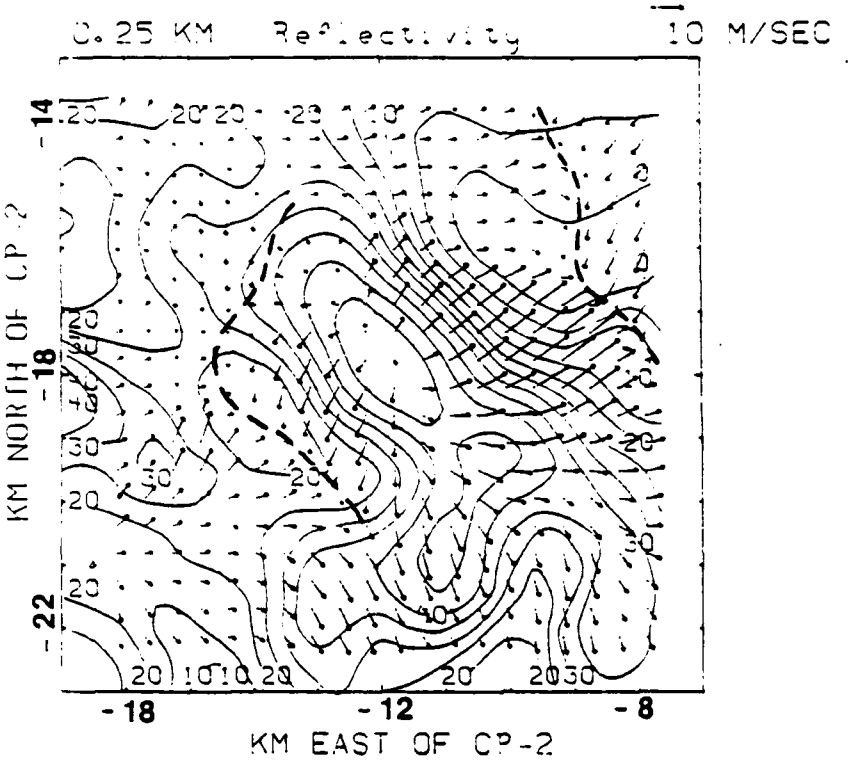

Fig. 6.1 Plan view of the horizontal wind and reflectivity field, for the 14 July 1982, 1649 MDT case at 0.25 km.

than zero. The lack of signal return suggests that environmental air is located there. The 0.25 km view confirms that a singular microburst event is in progress. The vertical dimensions of the storm may be obtained by examining higher levels.

The 0.50 km horizontal wind and reflectivity field, Fig. 6.2, reveals that the core reflectivities have increased to values greater than 50 dBz. The horizontal microburst winds have a maximum value at this level, although the winds in the area of Standley Lake are of approximately the same magnitude. The implication may be that the maximum magnitude of the horizontal wind at 0.25 km was due to the relatively low value of friction above the water surface. The vertical velocity field (see Fig. 6.3), while not at a maximum value, reveals that twin upward velocity centers coincided with the strong and weak gust fronts. A maximum value of 4 m/s occurs at -8.5 km east of CP-2 and -17 km north of CP-2. This area coincides with the convergence region on the strong gust front. A focusing mechanism for the updraft location on the front may be the location of the strongest winds in the cold air behind the gust front. A maximum value of shear is encountered where the maximum winds intersect the gust front. The microburst driving the outflowing winds has a value of descending motion of -2 m/s at .5 km. The microburst core does not contain a well defined perturbation pressure bubble, but a large value of low pressure occurs to

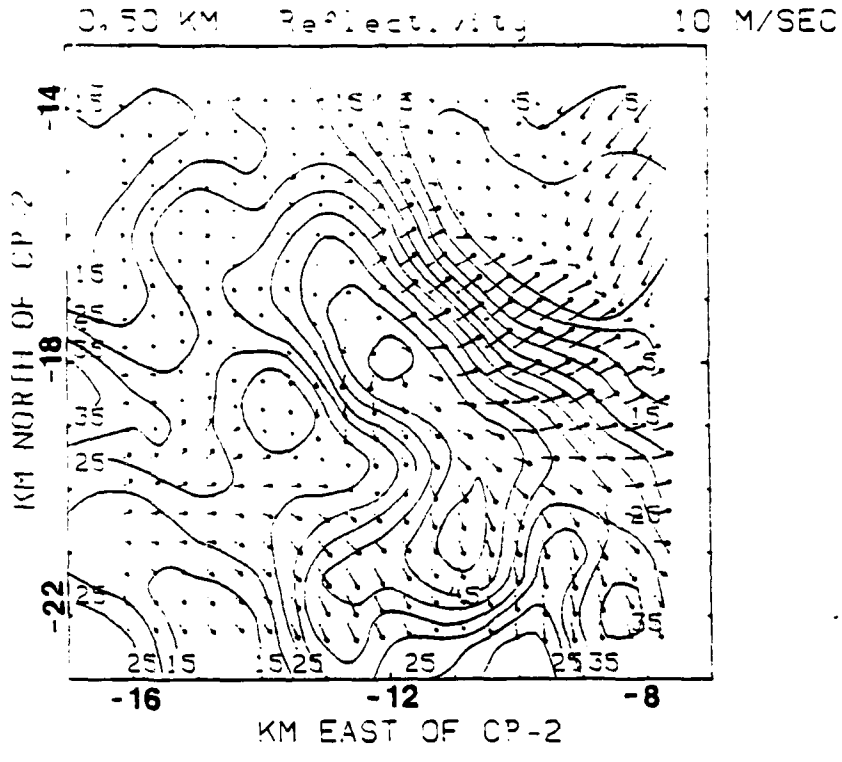

Fig. 6.2 Same as Fig. 6.1, except for 0.50 km.

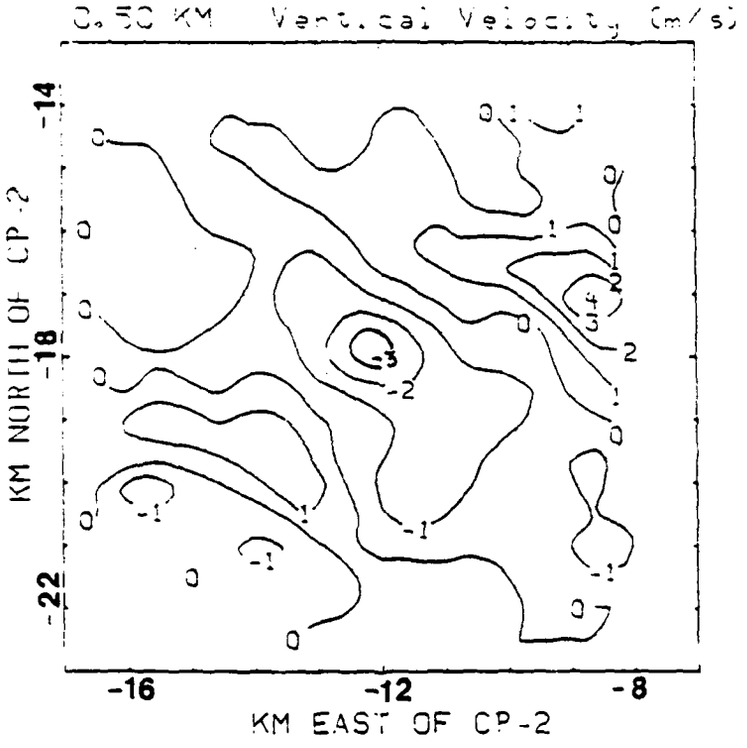

Fig. 6.3 Plan view of the vertical velocity field, for the 14 July 1982, 1649 MDT case at 0.50 km.

the east of the microburst (Fig. 6.4). The lack of a pressure bubble, which was found by Lin and Hughes (1987), suggests that less mass is being transported downward at 1649 MDT and more mass is being transported outward with the stronger horizontal winds relative to 1647 MDT, as the microburst enters the later stages of its life cycle. The large pressure gradient east of the microburst is consistent with the acceleration of air to the east. Another weaker low pressure area to the west of the microburst coincides with a weak gust front. The microburst center represents a warm-core system, as shown in Fig. 6.5. This finding is consistent with results obtained by Lin and Hughes (1987) for the 1647 MDT case that preceded this one. The warmest temperatures coincided with the strong outflow to the east of the microburst. The acceleration to the east of the storm outflow and the eastward distortion of the warm anomaly, may be due to the difference in friction in air flow over land and water surfaces. The apparent acceleration due to less friction will yield a lower pressure at low levels, where friction is a factor. At a higher altitude of 0.5 km, friction is less a factor; therefore, the apparent acceleration due to the lack of friction is not very great. The result of a lower pressure due to the apparent acceleration from lack of friction, relative to the area away from the lake, means that the dp/dz term in the temperature perturbation equation is maximized with a resultant

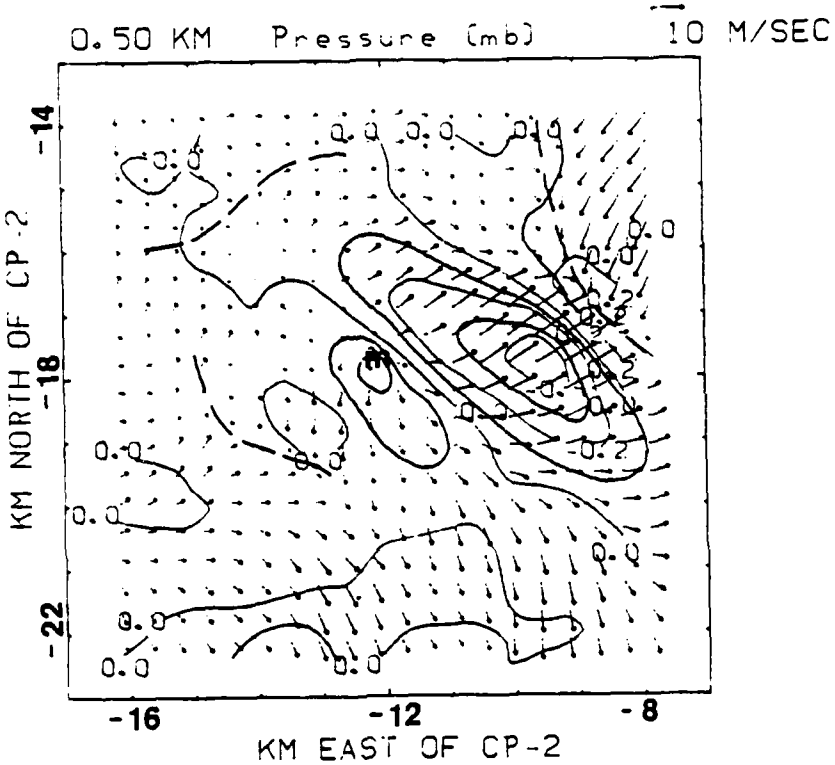

Fig. 6.4 Plan view of the perturbation pressure field, for the 14 July 1982, 1649 MDT case at 0.50 km.

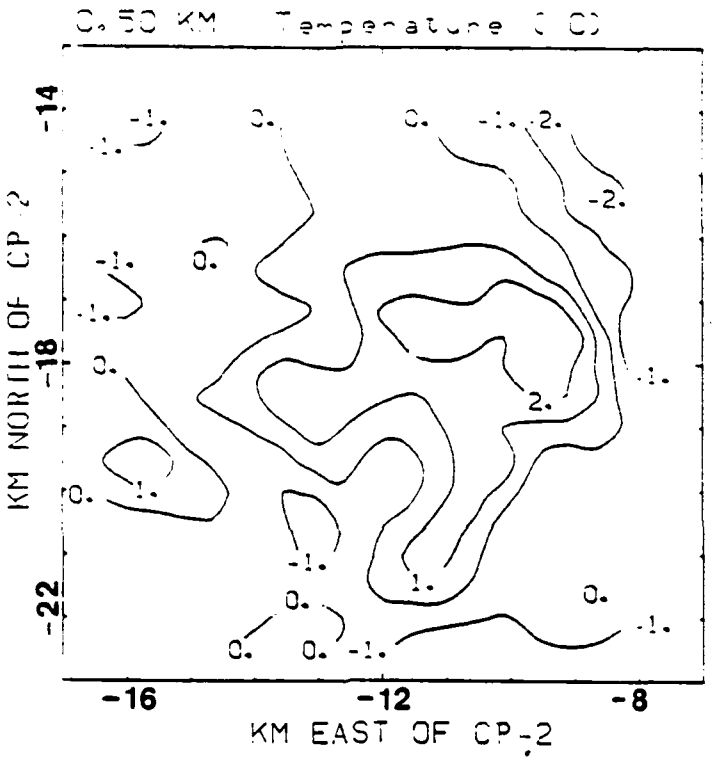

Fig. 6.5 Plan view of the perturbation temperature field, for the 14 July 1982, 1649 MDT case at 0.50 km.

maximum of perturbation temperature. The levels from 0.75 km to 1.5 km will be examined using the reflectivity and horizontal wind fields.

The horizontal wind flow at 0.75 km reveals a strong gust front to the east of the microburst is still intact (Fig. 6.6). Of note is the appearance of a dry tongue or notch, with left to right flow of low reflectivity air, into the bow echo structure. The majority of the horizontal motion contains a large component of mean motion and comparatively little eddy motion. Eddy motion consists of a diffluent pattern over the bow echo region and an inflow of air to the northeast of the microburst center. This pattern prevails at the 1.0 km level (Fig. 6.7), with strong winds now beginning to appear to the west of the bow echo. Also, strong inflow winds to the northeast of the microburst have expanded in area coverage and magnitude. The trend is for the microburst circulation to develop a jet to the rear of the bow echo and for the strong outflow in front of the storm to lessen in magnitude with a corresponding dissipation of the gust front. The 1.5 km horizontal wind pattern reveals the almost total loss of the strong outflow region east of the echo. See Fig. 6.8. A low level jet, also found by Lin and Hughes (1987), at 700 mb is present. Note the strong west northwesterly wind maximum to the west of the bow echo at -12 km east of CP-2 and -19 km north of CP-2. Strong confluence is

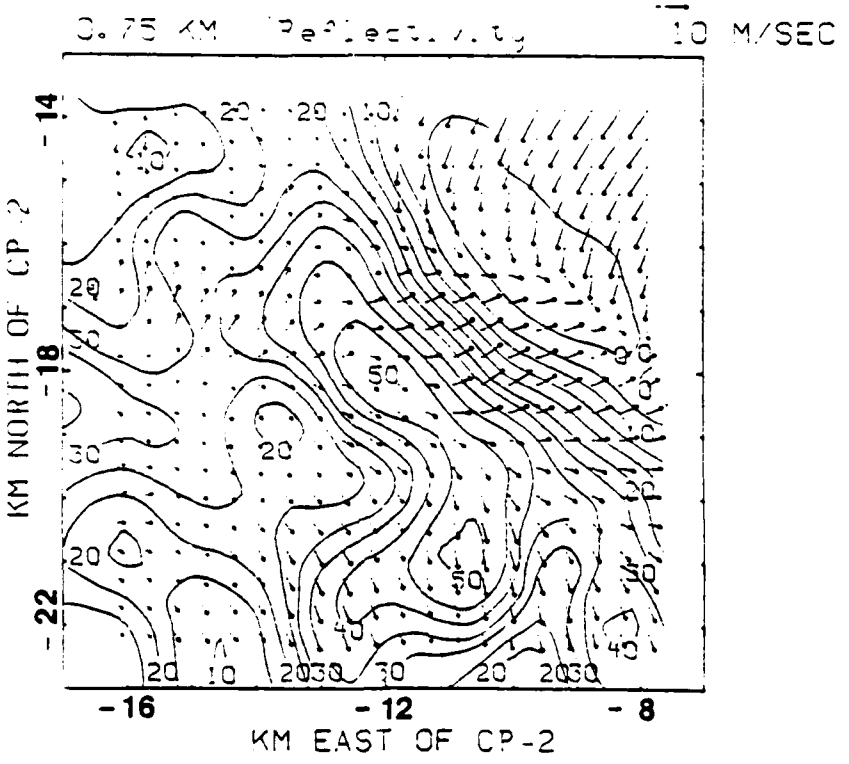

Fig. 6.6 Same as Fig. 6.1, except for 0.75 km.

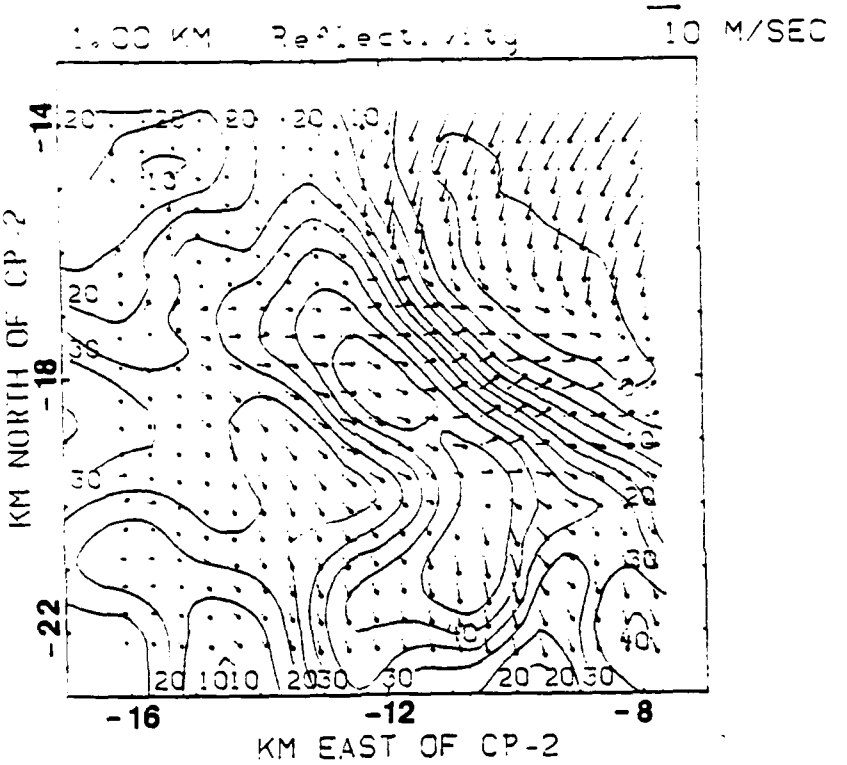

Fig. 6.7 Same as Fig. 6.1, except for 1.0 km.

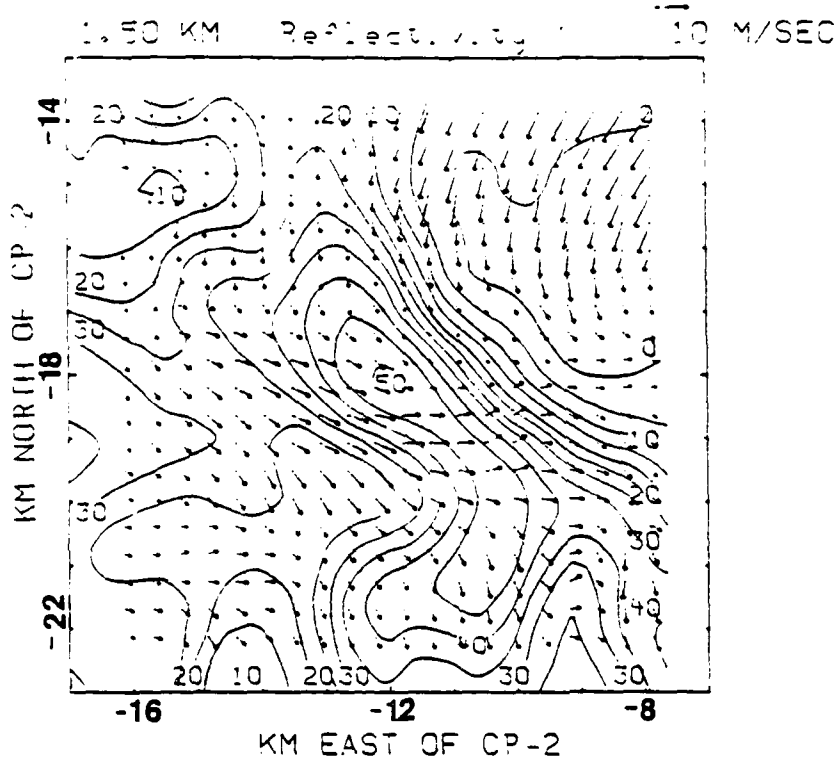

Fig. 6.8 Same as Fig. 6.1, except for 1.5 km.

noted to the north and northwest of the wind maximum and diffluence to the south and east of the wind maximum. The large decrease in magnitude of the horizontal wind across the bow echo suggests that some mass has to be transported either upward or downward just southeast of the 50 dBz maximum located in the microburst head. This phenomenon will be dealt with in greater detail at the 2.0 km level.

The 2.0 km level continues the trend of a stronger wind maximum to the rear of the microburst (see Fig. 6.9), as does all levels above 0.75 km. The wind maximum is better defined and stronger. It is interesting to note that the area of maximum winds is located in the area of maximum reflectivity gradient. The gradient becomes increasingly tighter in the confluence region to the northwest of the wind maximum, and a spreading of the gradient occurs to the southeast of the wind maximum in the diffluent region. The vertical velocity field, shown in Fig. 6.10, contains a large area of downward motion located where the horizontal winds are diverging outward from the wind maximum across the bow echo in the high reflectivity region. The reduction in magnitude of the horizontal wind across the bow echo at the microburst location, with a corresponding increase in downward vertical motion, suggests some of the dry, high speed, environmental air injected into the bow echo mixes with the saturated downdraft and enhanced

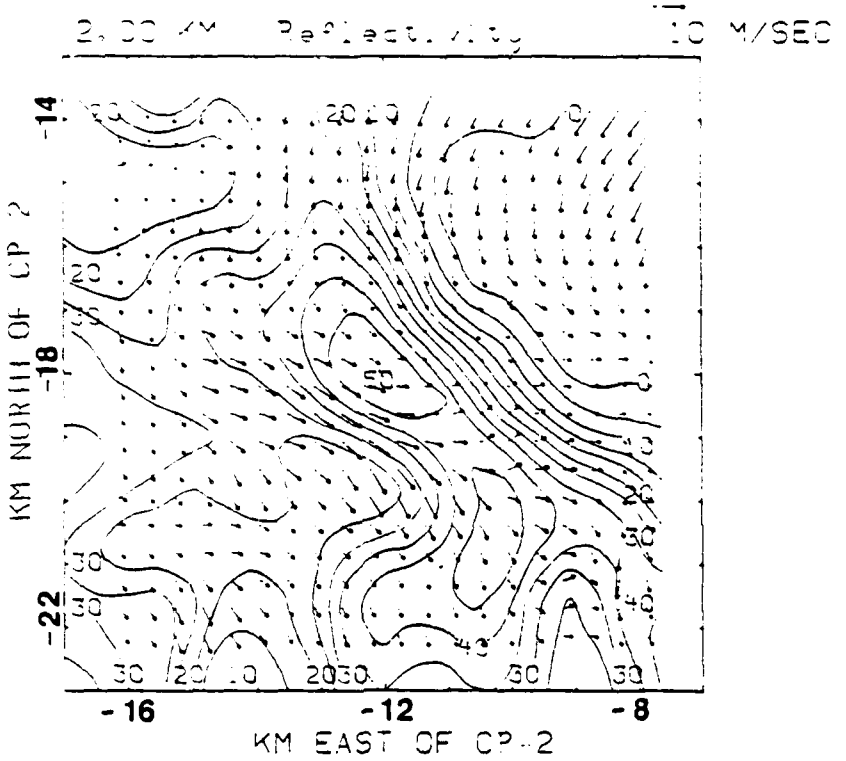

Fig. 6.9 Same as Fig. 6.1, except for 2.0 km.

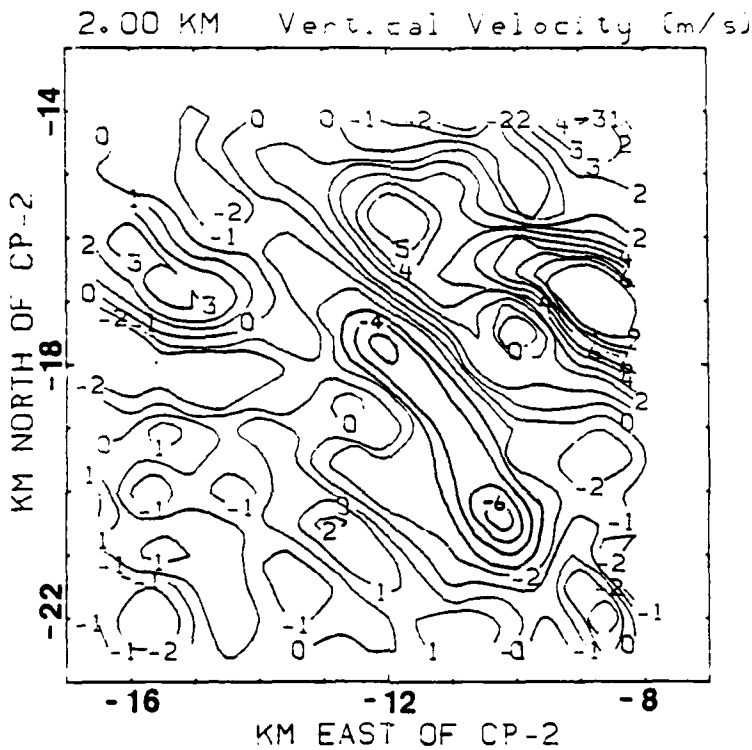

Fig. 6.10 Same as Fig. 6.3, except for 2.0 km.

the microburst. Lin and Condray (1988) showed that momentum flux is directed downward for the 1647 MDT, 14 July 1982 case. Strong upward vertical motion occurs where the gust front position occurred at lower levels to the area of the confluence or air into the jet. Apparently, some of the air feeding into the jet comes from lower levels. A small value of upward motion associated with the weak west gust front and coincident with the horizontal wind maximum, is located at -19 km north of CP-2 and -12.5 km east of CP-2. The wind maximum is associated with an area of lower pressure (Fig. 6.11). A strong maximum of perturbation pressure in the northeast sector of the grid accelerates the flow to the southwest, consistent with the horizontal wind field. The temperature perturbation field (Fig. 6.12) reveals an area of neutral to slightly warm temperature associated with the wind maximum, located in a low pressure region. This field also reveals an area of warming associated with the updraft at -8 km east of CP-2 and -16.5 km north of CP-2. An area of cooling in the exit region of the wind maximum is located at -12.5 km east of CP-2 and -19 km north of CP-2. This feature may be the result of mixing of the dry environmental air, advected in by the wind maximum, with the saturated air of the precipitation shaft. This area of maximum cooling is also coincident with the maximum wind crossing the bow echo at a large angle. By integrating the horizontal plan views of the

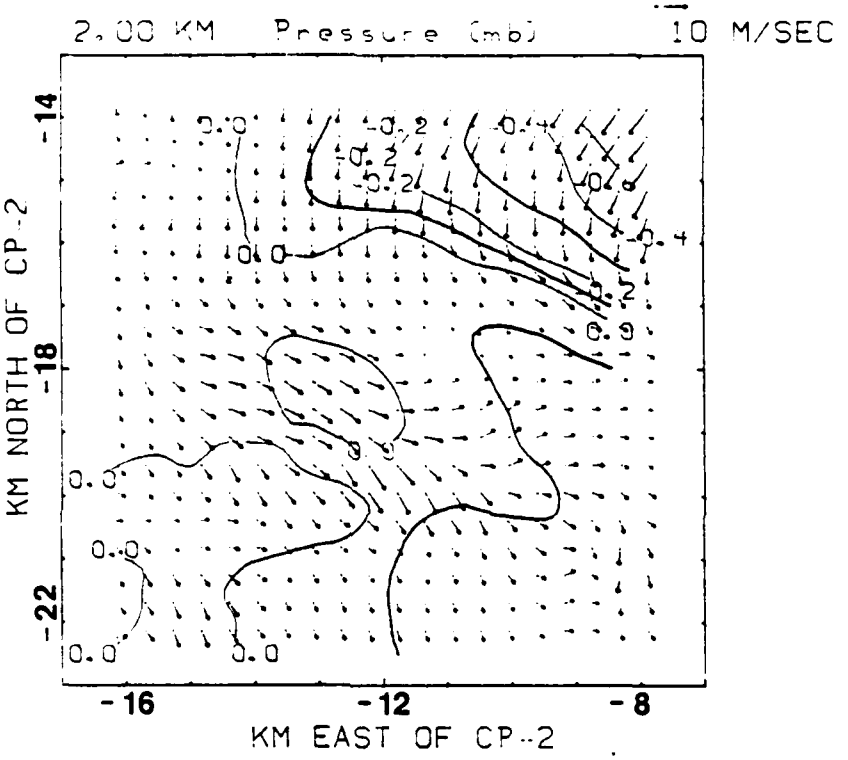

Fig. 6.11 Same as Fig. 6.4, except for 2.0 km.

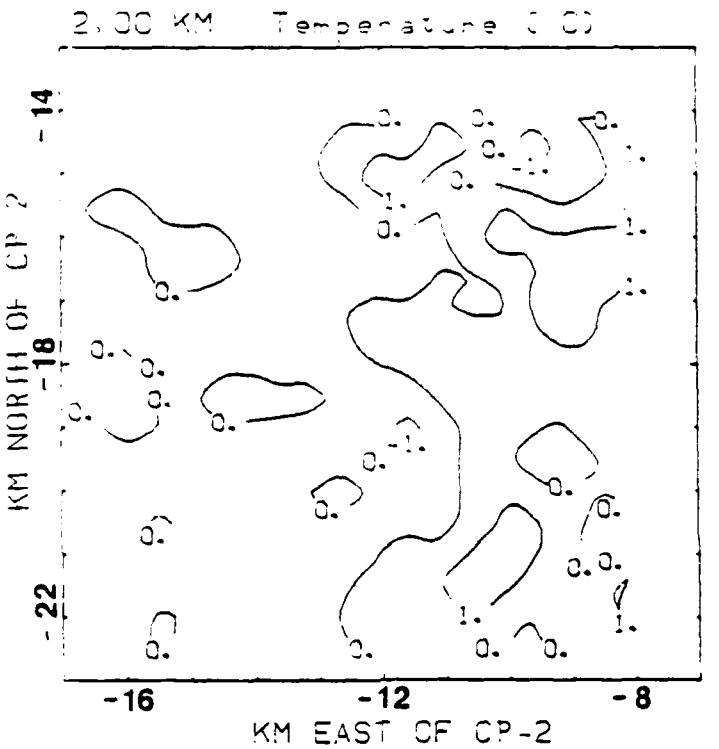

Fig. 6.12 Same as Fig. 6.5, except for 2.0 km.

storm into a vertical volume and relating features that maintain some continuity with height, a conceptual model of the 1649 MDT, 14 July 1982 storm, which represents a simple case of a singular wet microburst, may be obtained.

The simple wet microburst in summary consists of the classic structure of a strong downdraft with a velocity of approximately -4 m/s in a region of reflectivities greater than 45 dBz, spreading out upon reaching an altitude of less than 0.75 km AGL (above ground level) with strong horizontal outflow below 0.5 km. The center of the microburst features a warm-core in the boundary layer with a high pressure perturbation at the microburst center. The sole interaction that takes place is between the microburst and the surrounding environmental flow. The environmental flow vector was given as the mean wind.

Other features of note include the low pressure ring that virtually surrounds the microburst at low levels and the strong updraft located on the gust front to the east of the microburst. There is an absence of strong rotation above 0.75 km, but a low-level jet (LLJ) was noted for this case by Lin and Hughes (1987) at 3.5 km. The low level jet interacts with the downward, saturated air in the bow echo to enhance the downdraft. Also, this system was not rapidly changing between 1647 and 1649 MDT.

The simple case consists of a rapidly descending stream of relatively warm air in the boundary layer (below 0.75 km), embedded within moderate values of reflectivity (Z < 50 dBz) with a classic horizontal wind profile of a roughly symmetric, circular outflow pattern that was slowly evolving. The stagnation point at the site of the microburst's contact with the ground is characterized by a relatively warm area of high pressure. While the simple case may be advantageous for its ease of study and lack of complicated interactions, its use in understanding how the microbursts interact with each other and the environment to promote rapid changes in the kinematic structures at the microburst scale (meso -γ) are thought to be too simplistic for meaningful extrapolation. An examination of a more complex case is required.

6.2 Complex Case: An Analysis of the Kinematics for the 5 August 1982 Case

The second microburst event described will be the complex case. The boundary layer for the complex case was examined at 1845 and 1850 MDT. The presence of multiple microbursts and their interactions at different stages of development allows the researcher the ability to study a number of different possible interactions occurring at one area, at one time. It pro-

vides a more realistic microburst event that may be compared to the simple case to isolate events unique to the complex case, which may be due to complex microburst dynamics. Two different time periods are examined, so continuity is an added analysis tool present in this case.

The analysis will be conducted by examining the horizontal levels for structural features. Vertical continuity will be examined by evaluating two cross sections taken through areas of interest. The time continuity of features is revealed by examining two time periods. The 1845 MDT case will be examined first at each horizontal level, followed by the 1850 MDT case.

6.2.1 Plan View for the 5 August 1982, 1845 MDT Case

The plan view of the 0.25 km horizontal wind and reflectivity field is shown in Fig. 6.13. Distances are in kilometers from the CP-2 radar. It reveals that two microbursts are present, M1 and M2, which occur near or within the highest reflectivity regions of values greater than 50 dBz. The dominant microburst is the M1 feature. Its center is located at (x = -2, y = -23.5). Note that the environmental mean flow at this level is from 220 deg. at 6-8 kts. The other discernible microburst, M2, is located to the northwest of M1 near (-6,-19.5), and a third event, M4 (not shown), is located off the east edge

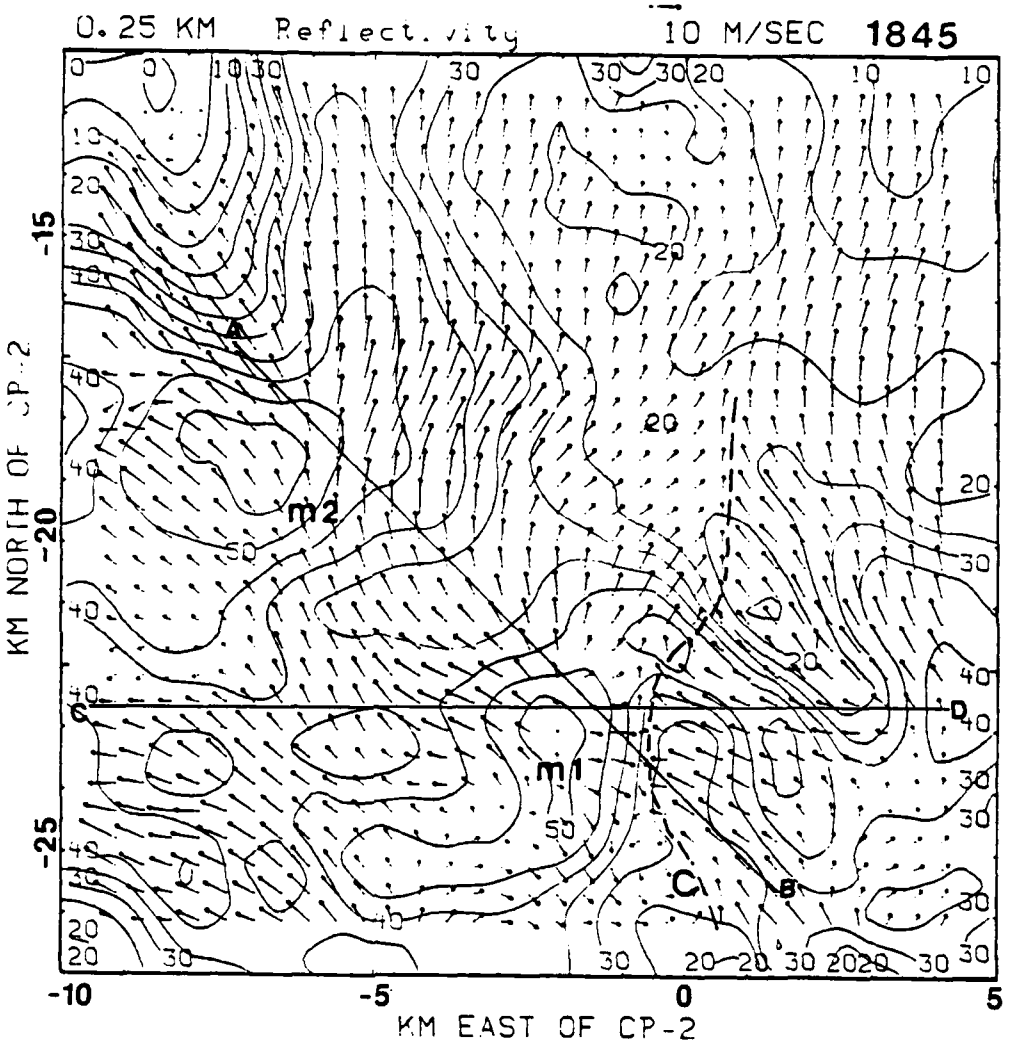

Fig. 6.13 Plan view of the horizontal wind and reflectivity field, for the 5 August 1982, 1845 MDT case at 0.25 km.

of the grid almost due east of M1. A gust front (GF) between M1 and M3, marked with the dashed line, begins at the south margin of the domain and extends northward to two thirds of the way across the grid. At the south end of the gust front (0, -25.5), a cyclonic circulation (C) is present. The wind field reveals that the combined flow of the environmental wind, and the outflow from M1 almost completely overwhelms M2. It is not obvious from the horizontal wind flow that M1 and M2 are separate microbursts. The temperature pattern at this level (Fig. 6.14) may be of help in establishing the fact that two distinct microbursts are within the grid. The M1 and to a lesser extent M2 are both cold-core and separate entities, which contrasts with the warm-core microburst noted for the 1649 MDT, 14 July 1982 case. The M2 microburst does not have a well defined cold core located at the area of strongest downward motion and highest reflectivity, because the combined outflow from M1 and the environment overwhelms and distorts the storm structure. Another area of relatively cool air is associated with the gust front. A very warm value of +3 ^{o} C, located in the middle of the grid at (-2.5,-18.5), may be due in part to terrain and partially due to the one sided finite difference technique required at the lowest level. A net decrease of 200 meters between the microburst location and the anomaly location results in a channeling and acceleration of the flow. An area

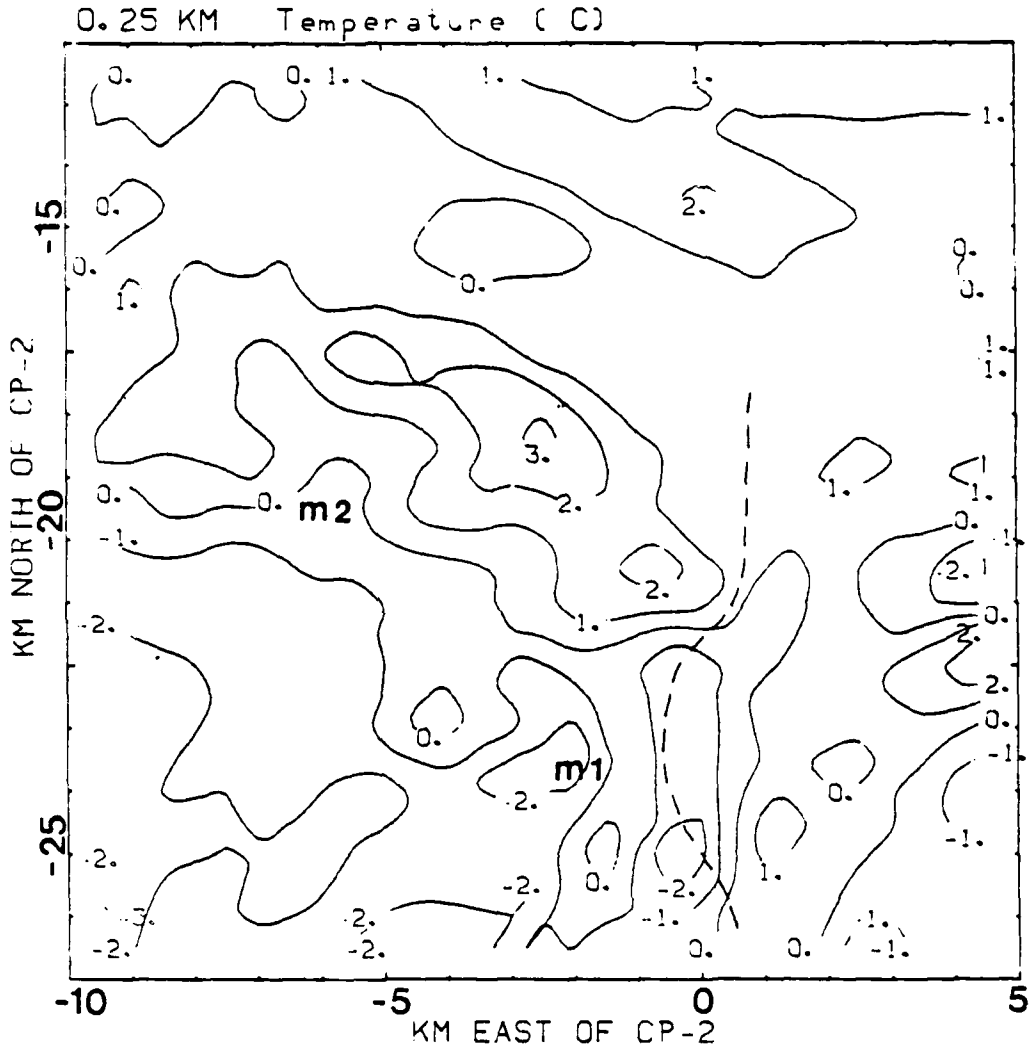

Fig. 6.14 Plan view of the perturbation temperature field, for the 5 August 1982, 1845 MDT case at 0.25 km.

of strong winds at 0.25 km is not reflected at 0.50 km because the terrain has less effect at that level. The relative low pressure region near (-5,-17) at 0.25 km, associated with the area of strong winds, is not as pronounced at 0.50 km (Fig. 6.15), which yields a smaller low pressure anomaly relative to the surrounding area. The $-\partial p/\partial z$ term is therefore a maximum. A warm anomaly results in the area of strong downslope winds.

An examination of the 0.50 km level reveals that the microburst positions on the grid, and the cyclonic circulation (C) on the gust front, are still present (Fig 6.16). The M1 microburst still overwhelms the M2 microburst no apparent gust front between the two features. The M1 microburst features a coincident value of -2 m/s vertical motion (Fig. 6.17). A value of -1 m/s vertical motion, associated with M2, is removed from the region of highest reflectivities, and is displaced downwind from the combined mean flow and outflow from M1, as the outflow from M1 overwhelms M2's divergent structure. The maximum divergence is thus shifted to the downwind side of M2. An important characteristic of the vertical velocity field is that it clearly delineates M1 and M2. Both M1 and M2 are located in an area of sinking motion. A ring of upward motion virtually surrounds M1 and M2, even the area between M1 and M2. One may expect a correlation between the vertical velocity and the pressure fields. The perturbation pressure pattern (see

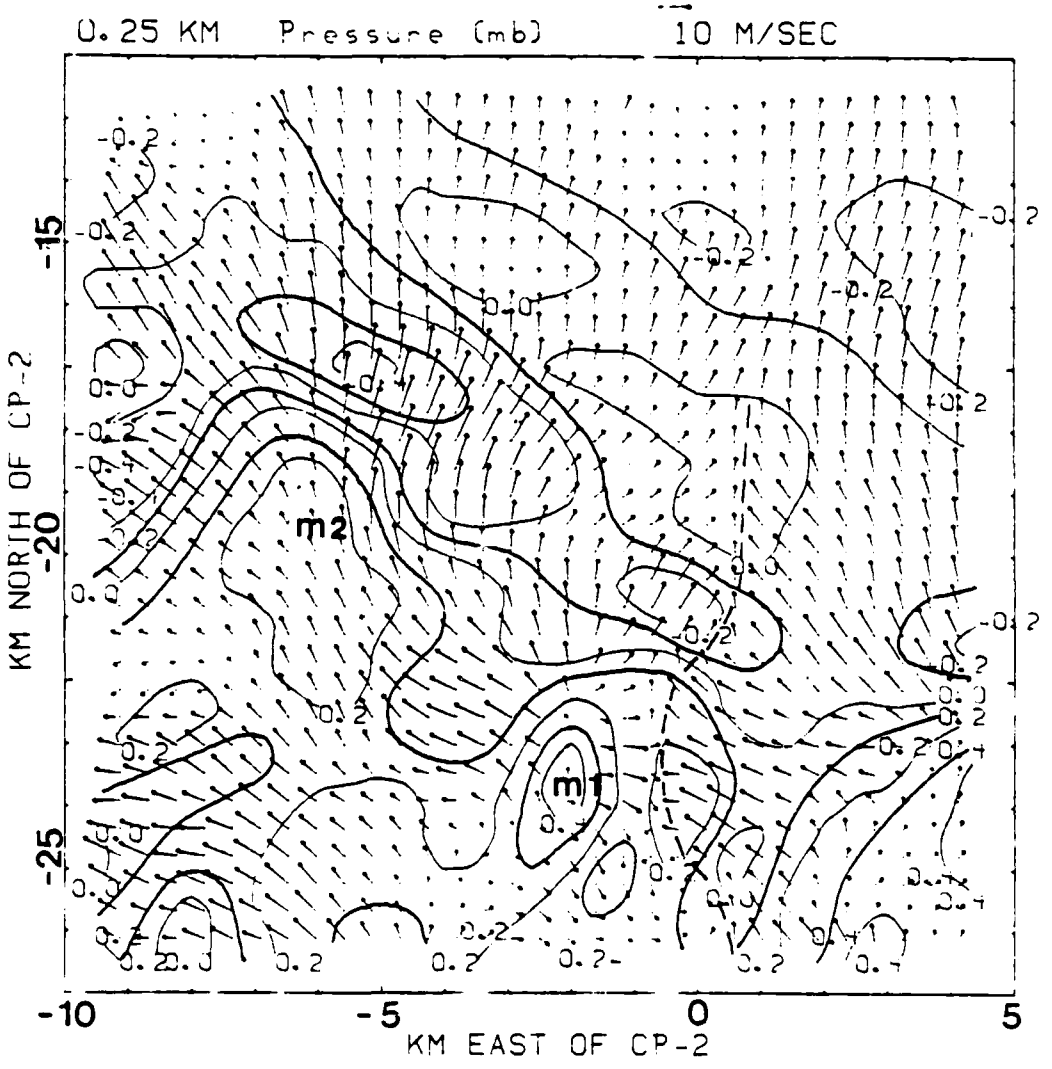

Fig. 6.15 Plan view of the perturbation pressure field, for the 5 August 1982, 1845 MDT case at 0.25 km.

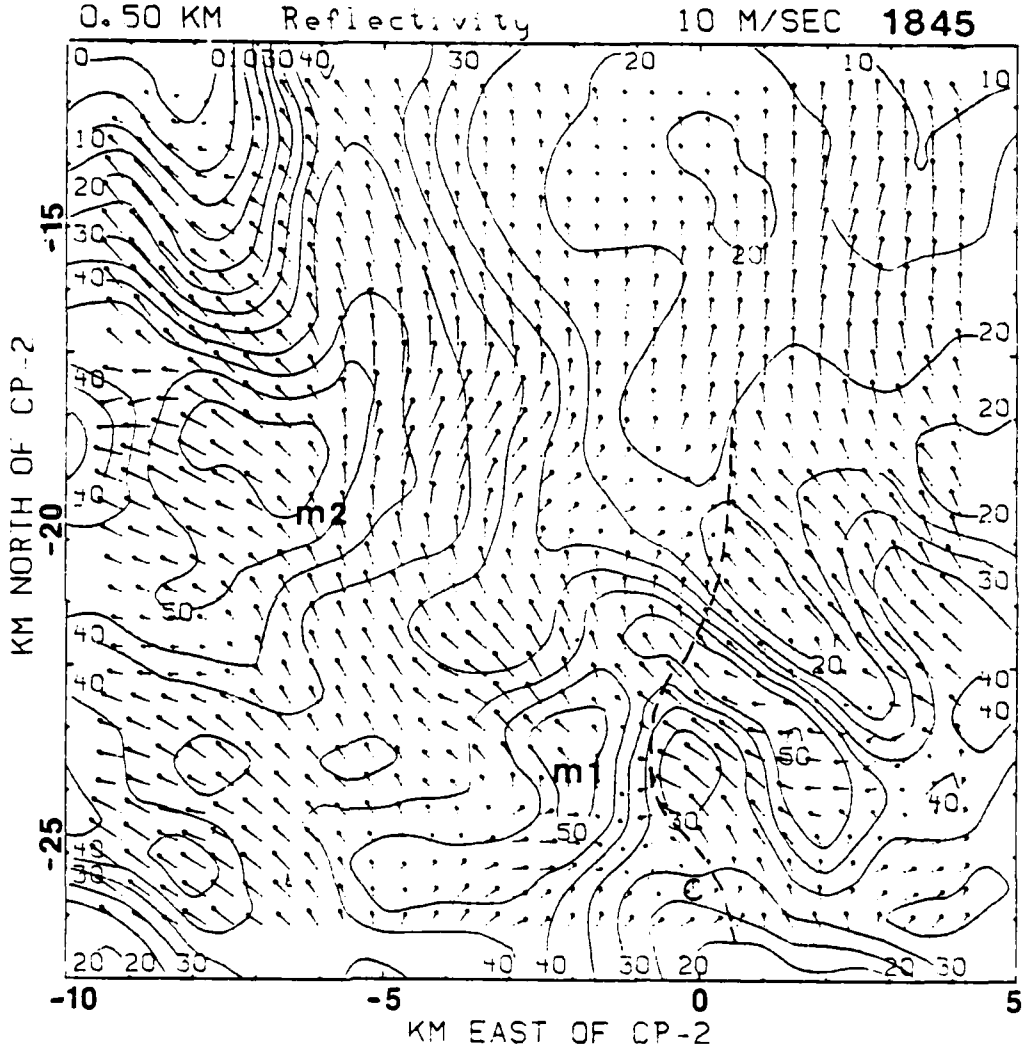

Fig. 6.16 Same as Fig. 6.13, except for 0.50 km.

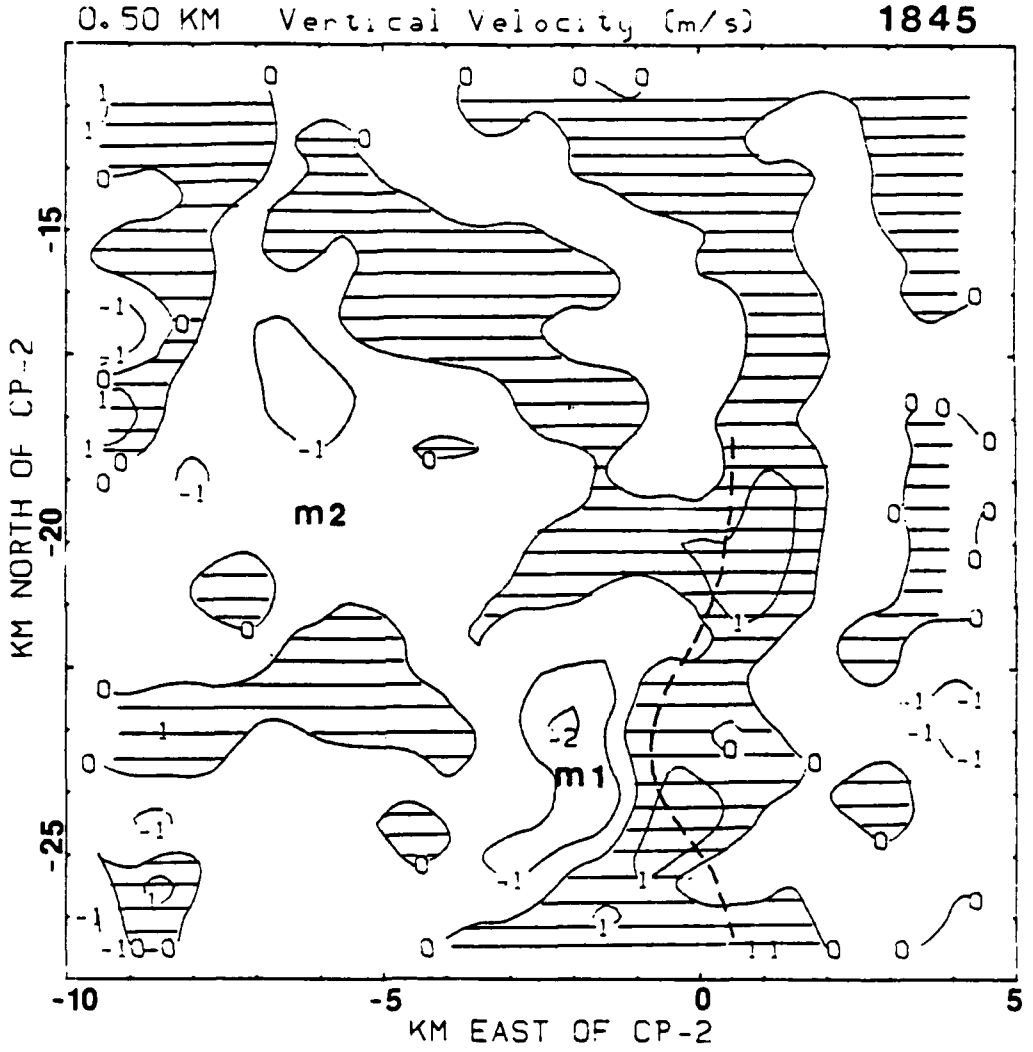

Fig. 6.17 Plan view of the vertical velocity field, for the 5 August 1982, 1845 MDT case at 0.50 km.

Fig. 6.18) reveals that the microbursts are areas of relatively high pressure of +0.2 mb for M1 and +0.3 mb at M2. Low pressure is located along the gust front and generally surrounds the microbursts. The cyclonic vortex located on the gust front has low pressure. The temperature pattern at 0.50 km (see Fig. 6.19) features a less amplified temperature pattern than 0.25 km. The M2 and M1 microbursts are still nominally cold core. The cyclonic circulation on the gust front also features a relative colder region as upward motion increases; thereby, cooling the unsaturated inflow air by dry adiabatic expansion. Also note that the warm anomaly to the east of M2 is much reduced in area and the magnitude of the warm anomaly has decreased by two thirds. The strong outflow region of the microburst structure has been examined, but an examination of higher levels is needed to determine the complete storm structure.

A dramatic change takes place in the horizontal wind field at 0.75 km, as shown in Fig. 6.20. The flow is predominately from the southeast or south. The total flow has thus become almost exclusively environmental flow in the horizontal plane with little horizontal eddy motion. This is not to say the microbursts do not exist or affect the wind field, but their influence is limited to vertical velocity. This means that 0.75 km can be thought of as a level of non-divergence for this

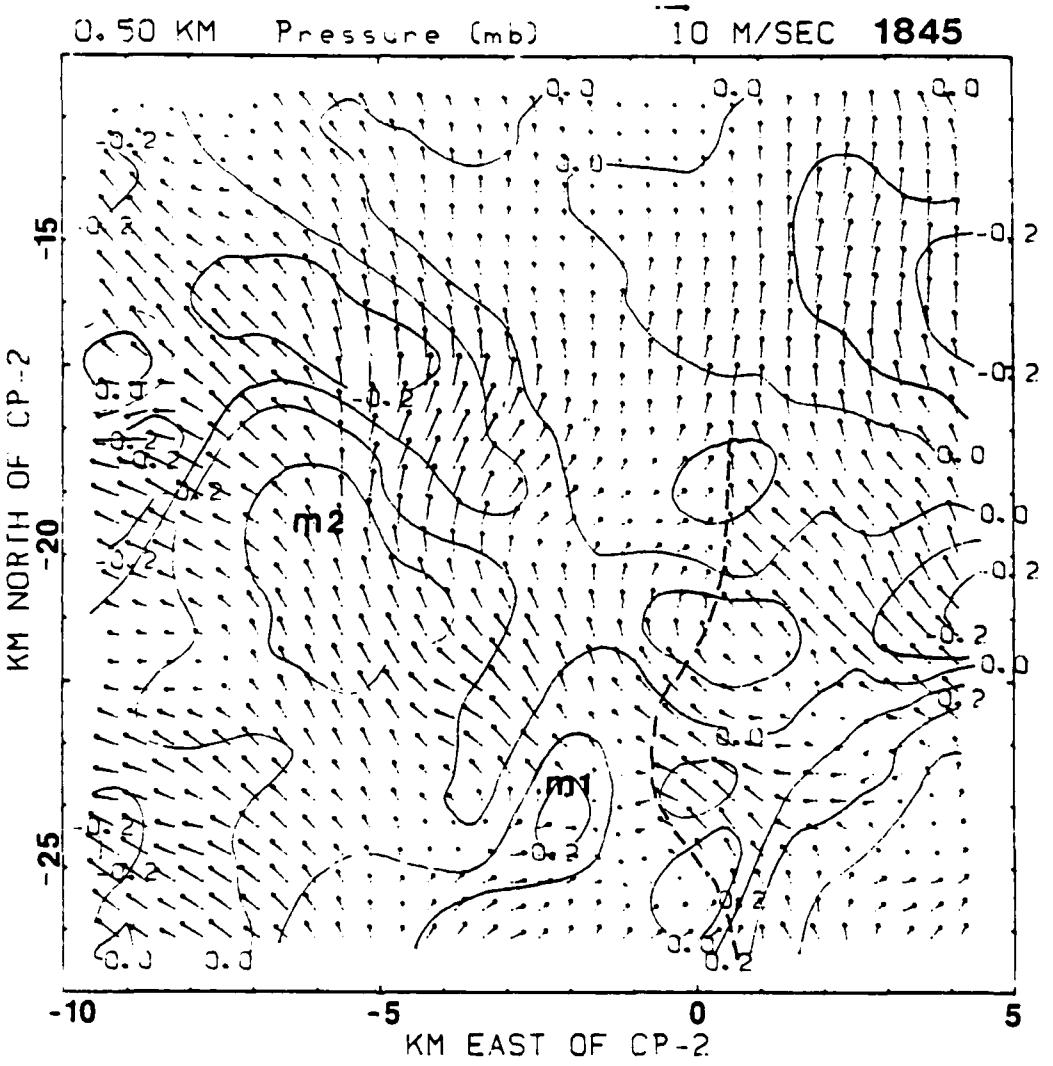

Fig. 6.18 Plan view of the perturbation pressure field, for the 5 August 1982, 1845 MDT case at 0.50 km.

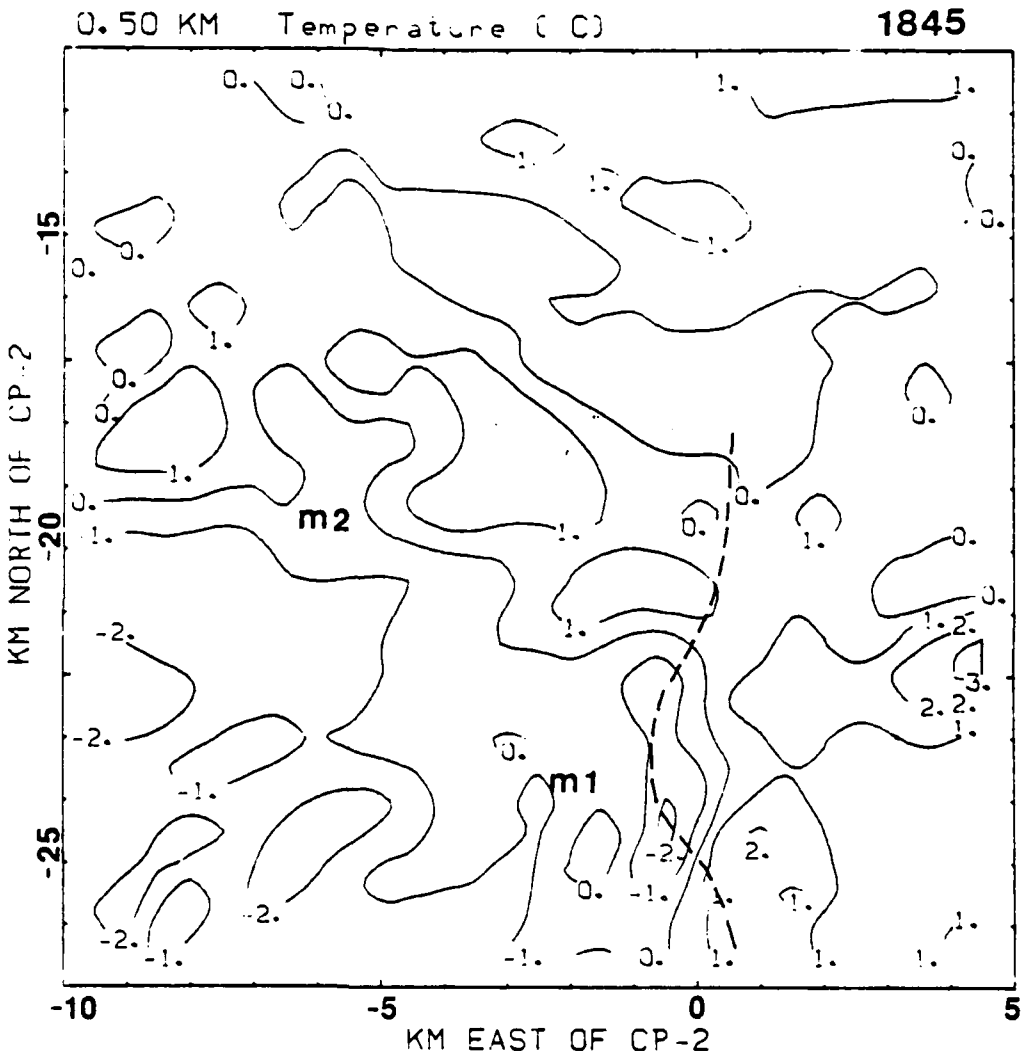

Fig. 6.19 Same as Fig. 6.14, except for 0.50 km.

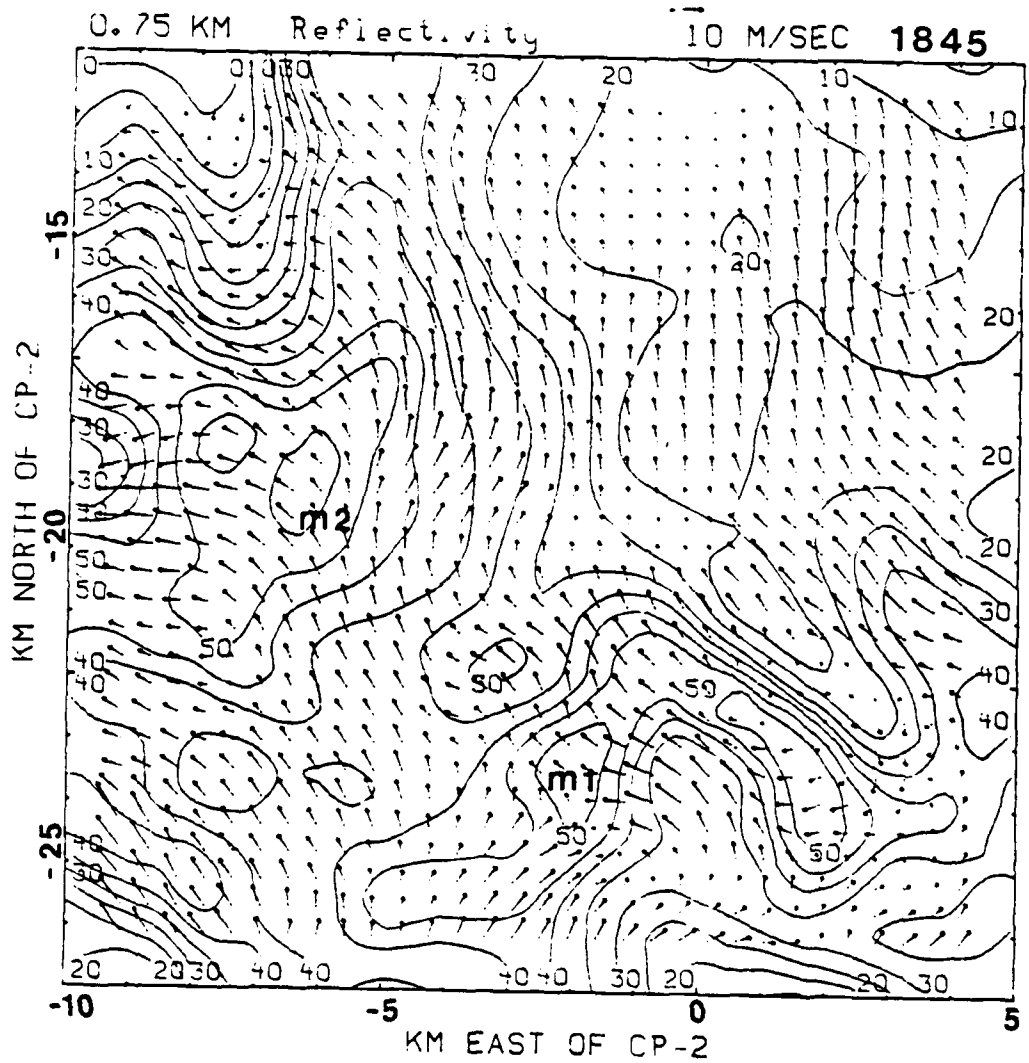

Fig. 6.20 Same as Fig. 6.13, except for 0.75 km.

particular microburst. The microburst downdraft does not decelerate greatly due to the effect of the earth's surface at this level, nor is it at a level where mass originates and is collected for downward transport, since there is comparatively little entrainment into or transport out of the downdraft. Rather it acts as a conduit, where mass collected above may pass through this layer to be distributed by horizontal divergence below 0.75 km. The cyclonic circulation at the south end of the gust front near (-1.5,-25) remains, although the circulation becomes an open wave. The cyclonic circulation extends to about 0.75 km of depth with ever increasing radius of rotation. The circulation slightly tilts to the west northwest with height. Also note that the winds tend to blow parallel to the reflectivity contours to the northeast of M2 and to the southeast of the cyclonic circulation. This suggests that the strong outflow of precipitation cooled air from the high reflectivity core, which occurred at lower levels, is not taking place. It also suggests that entrainment of dry environmental air from flow towards higher reflectivity values is likewise absent. The upper levels should reveal if any dry entrainment of environmental air occurs at those levels.

At the 1 km level (Fig. 6.21), the most significant change in the wind flow is the increase in the crossing angle of flow of the environmental air from the low reflectivity regions,

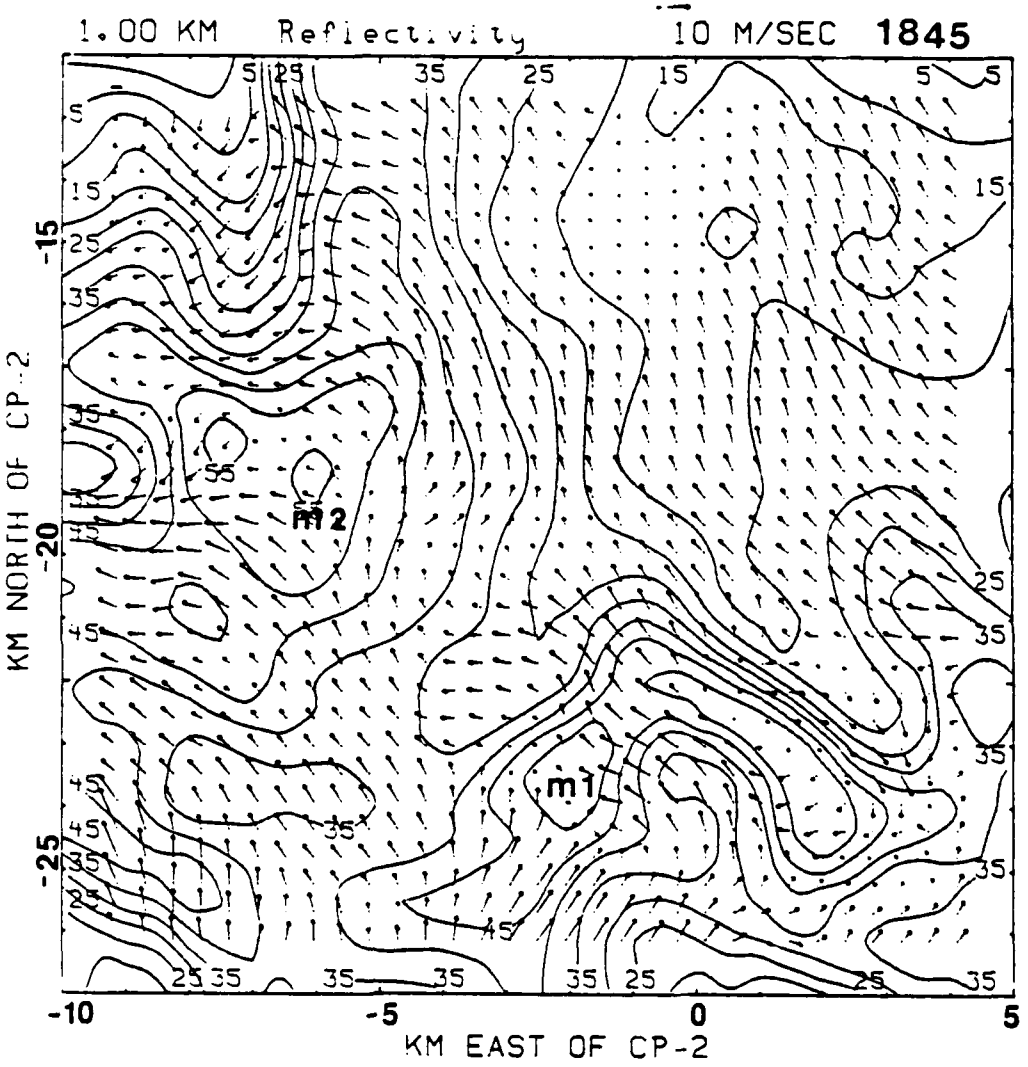

Fig. 6.21 Same as Fig. 6.13, except for 1.0 km.

located southeast of M1 and northwest of M2, towards the high reflectivity cores associated with the descending precipitation shaft. This suggests that entrainment of dry air is beginning to occur at this level. Also note the beginning of cyclonic curvature in the flow around the north sides of M2 and M1. However, the cyclonic curvature associated with the cyclonic circulation on the south end of the gust front is no longer present. The reflectivity pattern features a finger-like reflectivity pocket southwest of M1 at 0 km east of CP-2. This feature curls counter-clockwise up the grid and back towards M1. Another finger-like projection extends down the grid from the extreme northwest corner of the grid, pointing at M2. A higher level will be examined to confirm the existence of these features and establish a trend in development of the features.

Many structural features of the 1 km level are better organized at 1.25 km and more intense. For instance, the fingers of dry air intrusion are broader than 1 km and the crossing angle of the dry environmental air toward the high reflectivity core increases to nearly 90 deg. (Fig. 6.22). A general cyclonic turning of the winds occurs around microbursts M1 and M2. A distinct cyclonic circulation occurs with M1 at (-2,-23.5). Inflow of dry air into M1 is from the southeast, while inflow into M2 is from the north. Since M1 effectively scavenges and blocks the southeast environmental

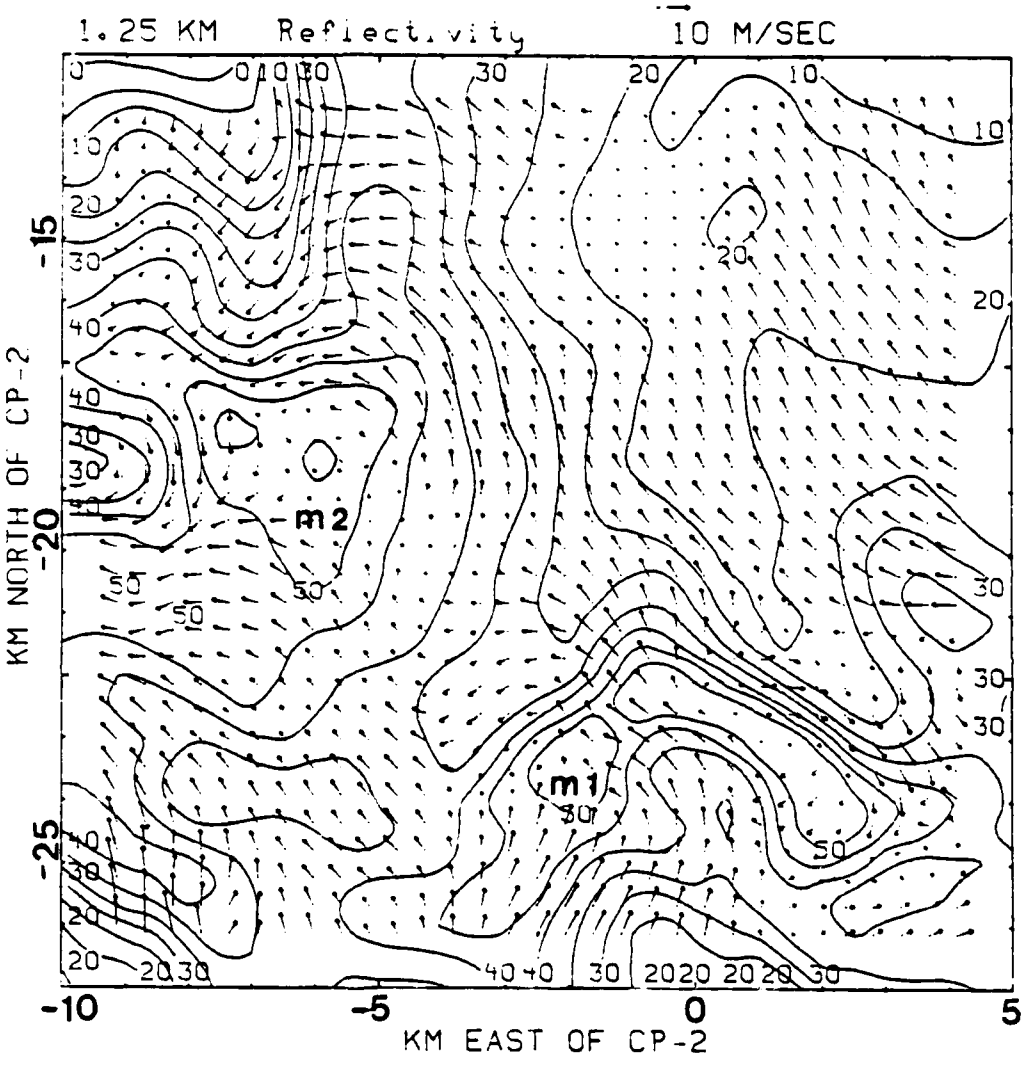

Fig. 6.22 Same as Fig. 6.13, except for 1.25 km.

wind, the M2 microburst circulation is forced to obtain its supply of dry air from the north. Unlike Fujita's (1985) description of the misocyclone structure, where he described the misocyclone's role as a collector of hydrometeors for the microburst, to enhance precipitation loading, I propose that the misocyclones act as pinwheels that funnel in and efficiently collect dry environmental air, which will enhance evaporative cooling by ventilating the saturated downdraft. The air is mixed with the downward rushing air to create evaporative cooling at least on the outside layer of the microburst and thus enhances negative buoyancy. This theory is supported by looking at the temperature pattern for 1.25 km, as shown is Fig. 6.22. A warm core (1 ^{o} C) at the downdraft center (-2.5, -24.5) with surrounding cool air (-2 ^{o} C) is noted. Also note the warm (3 ^{o} C) anomaly associated with the relatively warm, dry, environmental air entrained into the system. More evidence of the role played by the misocyclone will be discussed in Section 7. M2's circulation is considerably modified by M1, especially on its south side so comparison is difficult, but cooling is noted on the north semi-circle of the microburst and a warm anomaly is associated with the southward flowing entrained environmental air. Another warm anomaly at (0,-21) is associated with an area of low reflectivity and upward motion (Fig. 6.24) that may be associated with the outflow from the bow

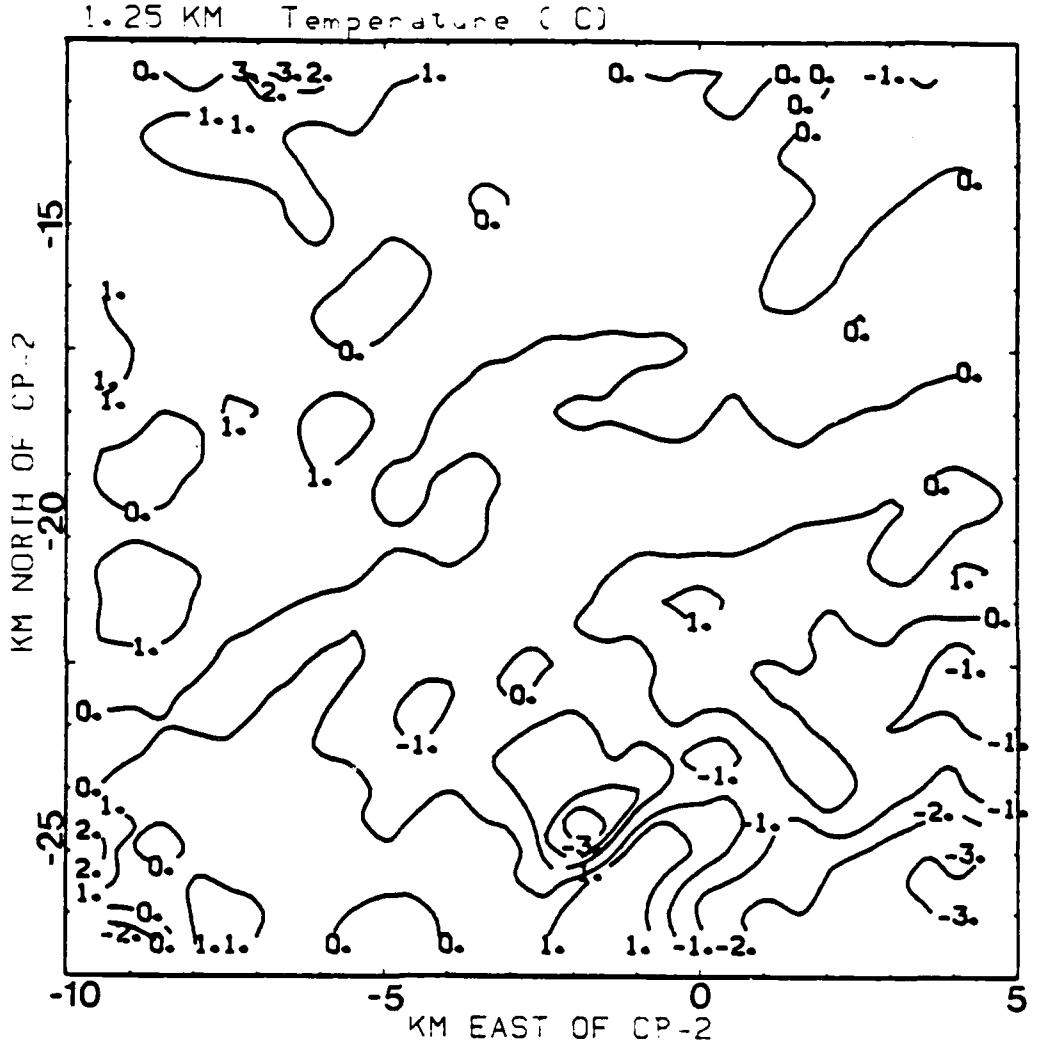

Fig. 6.23 Same as Fig. 6.14, except for 1.25 km.

echo. The bow echo is primarily a warm core, but surrounded by cooler air, probably due to entrainment processes. Inflow environmental air can be seen feeding into this feature from the southeast. As the warm environmental air is being horizontally entrained, it maintains a warm anomaly since it is only very slowly rising and cooling until it enters the main updraft. Additionally, it does not encounter evaporative cooling until it enters the updraft and meets the saturated region surrounding the updraft. When it enters the main updraft it also rapidly cools by dry adiabatic ascent; therefore, it rapidly becomes a cold anomaly. While the temperature pattern reveals a good deal of the storm's structure, the pressure pattern does not. The pressure pattern at 1.25 km (Fig. 6.25) reveals that the highest pressure is located in the southeast and northwest corners of the grid. Low pressure centers are located near the centers of cyclonic circulation, but offset by 2 km. The mass flow is therefore toward the cyclonic center from the surrounding domain not associated with the cyclonic gyre. This is analogous to water running down a drain.

The areas of downward motion are weakly warm at this level. Microburst M2 is definitely warm-cored, while the main updraft is neutral to slightly cool. One difference is that the distance between M1 and the main updraft is only two kilometers, while M2 is more than four kilometers removed from the

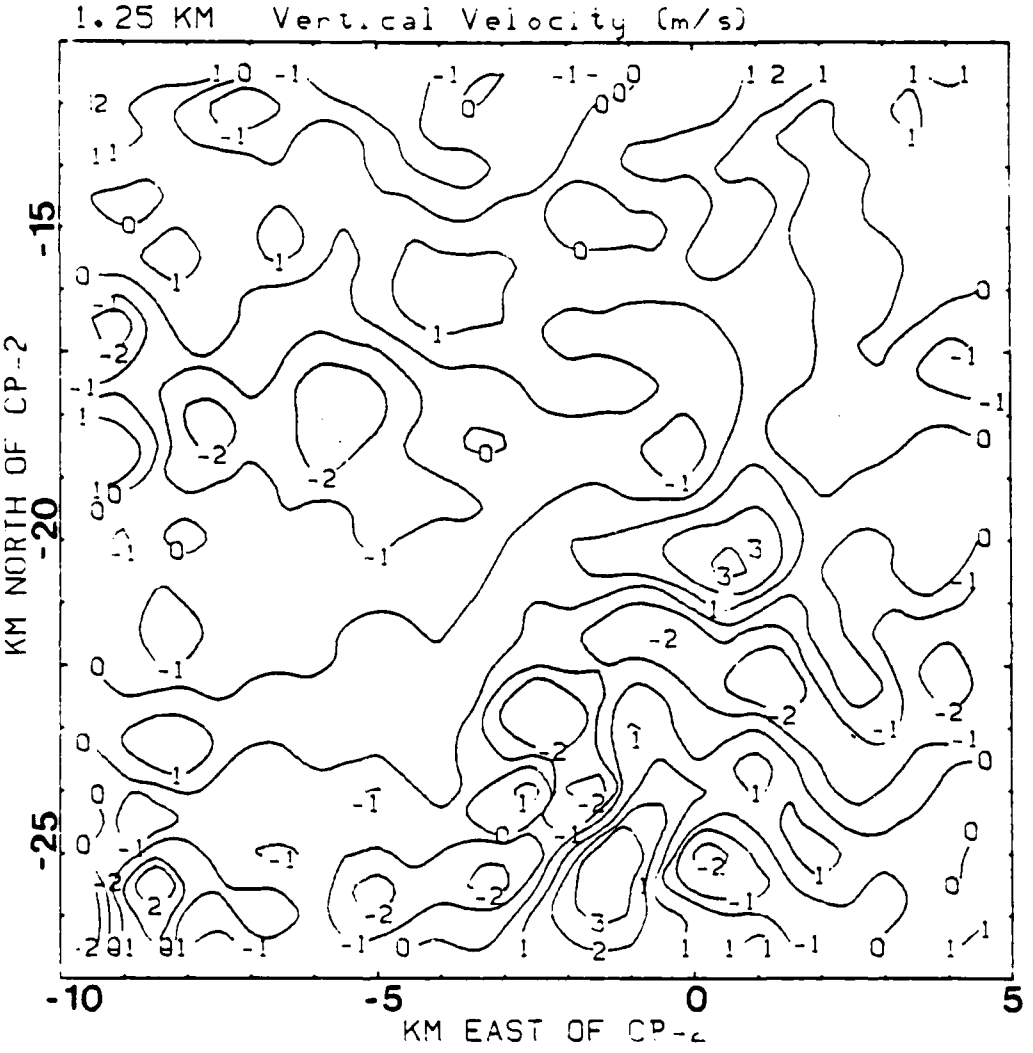

Fig. 6.24 Same as Fig. 6.17, except for 1.25 km.

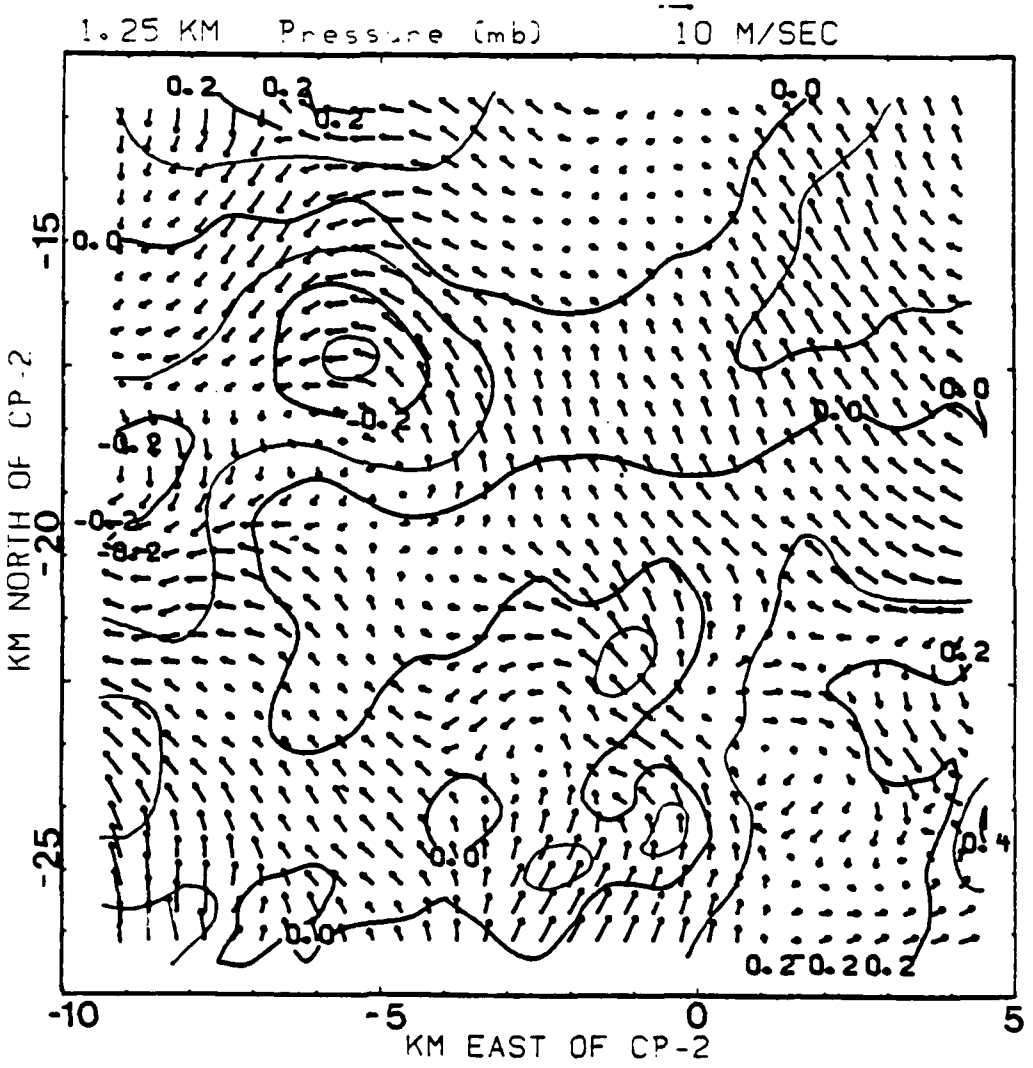

Fig. 6.25 Same as Fig. 6.18, except for 1.25 km.

updraft. At the relatively coarse grid scale of 0.5 km, the larger cold anomaly of the updraft may influence the weak warm anomaly associated with the downdraft. Some of the ascending cool air may be entrained into the misocyclone, which in turn may add additional negative buoyancy to the downdraft. The 1845 MDT time period revealed the presence of a complex system of several microbursts with associated gust fronts and misocyclones. An examination of a second time period at 1850 MDT will allow for an estimate of the consequences of various microburst interactions between themselves and the environment. A conceptual model may be formulated explaining how the storms are evolving.

6.2.2 Plan View for the 5 August 1982, 1850 MDT Case

The plan view of the 0.25 km level will be examined by looking at the 0.50 km grid spacing case and one that uses 0.25 km grid spacing. The 0.50 km grid (Fig. 6.26) shows that the wind circulation pattern undergoes some subtle but significant changes by 1850 MDT. The major change is the appearance of M3 at the eastern tail end of the bow echo, associated with M1. The 50 dBz contour has expanded and M3's appearance is coincident with the appearance of the 50 dBz contour. The gust front is very well defined, but it is bridged by M3 at its mid-

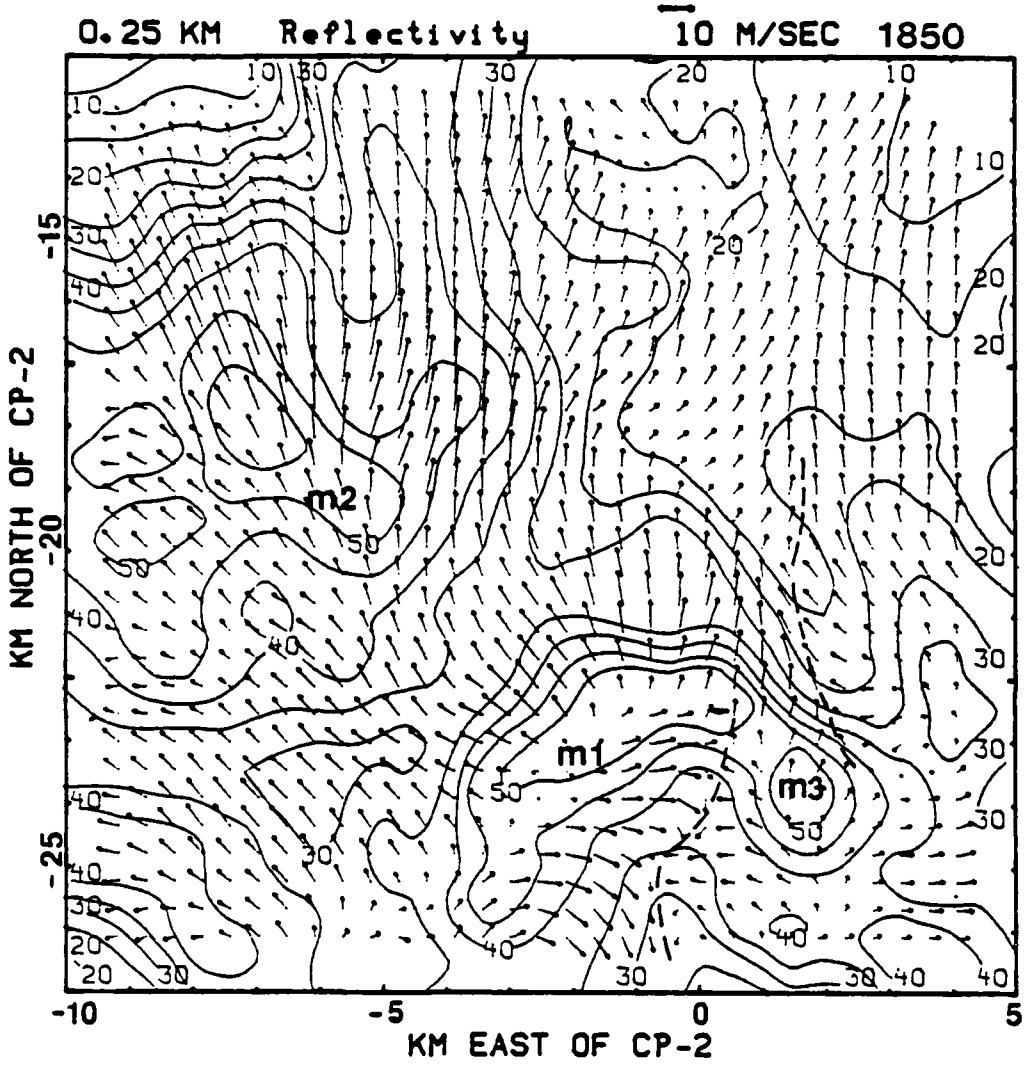

Fig. 6.26 Plan view of the horizontal wind and reflectivity field, for the 5 August 1982, 1850 MDT case at 0.25 km.

die point. M3 has also succeeded in disrupting the inflow into the cyclonic gyre on the gust front. The disruption of the inflow into the cyclonic gyre on the gust front has forced the cyclonic gyre southeast along the gust front to the edge of the grid. The movement south results from the southward shift in the area on the gust front that interacts with the southeast environmental flow. The area of greatest cyclonic shear combined with interaction with warm, buoyant environmental air occurs at this point. The gyre is in a weaker state of organization. The M2 microburst remains embedded within the outflow of M1 and the environmental flow; however, the M2 microburst does possess greater values of reflectivity at 1850 MDT with values of 55 dBz present. There is a strong flow of air toward lower dBz values of reflectivity. This suggests that precipitation cooled air is flowing toward and undercutting the warmer environmental air. Recall from the discussion of the 1845 MDT plan views, at higher levels, the flow is toward the high reflectivity values.

This level will now be examined at the smaller grid scale of 0.25 km (Fig. 6.27) to see what sensitivity the main features may have to a higher resolution grid. One difference is that the M1 bow echo now has reflectivities greater than 60 dBz, noted near the middle of the bow echo. The new microburst M3 remains a distinct feature and the M1 bow echo reveals that

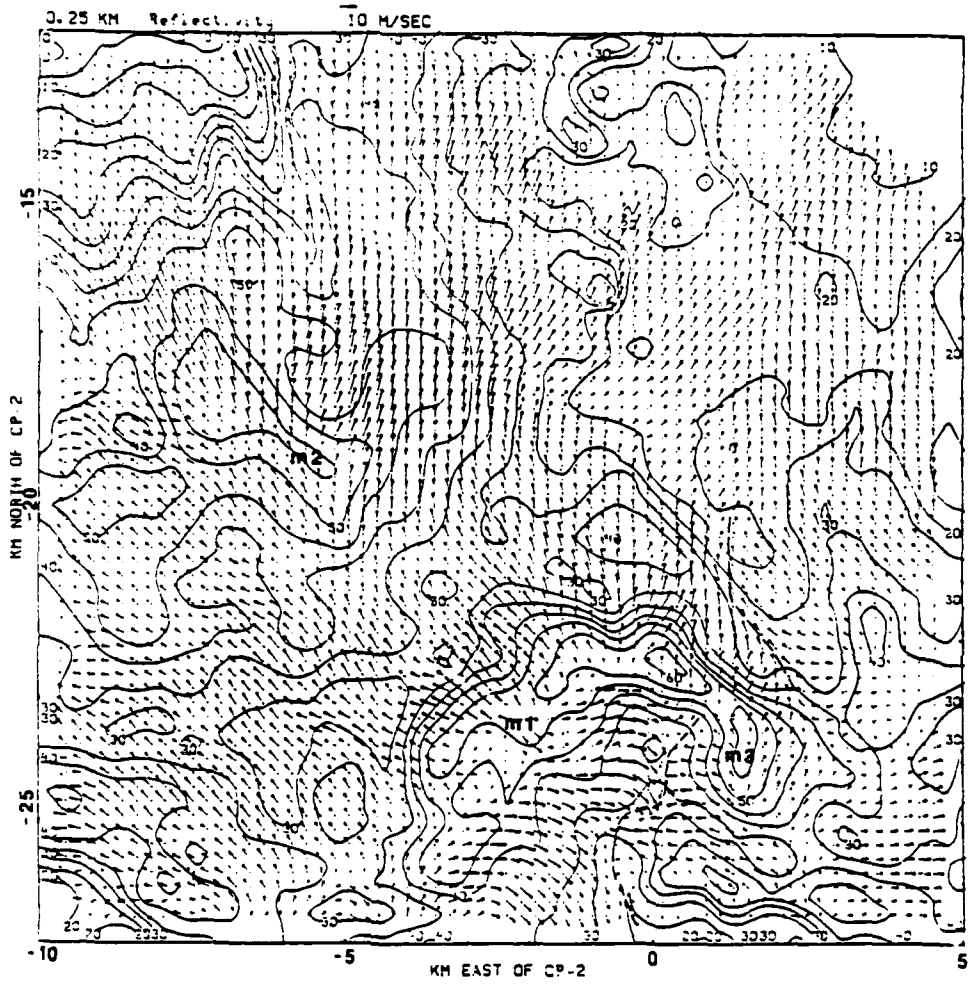

Fig. 6.27 Same as Fig. 6.26, except using a 0.25 km grid spacing.

it is composed of several distinct cells; whereas, at the 0.50 km scale it was rather amorphous. It is interesting to note that all three of the microbursts are embedded within an area of reflectivity greater than 55 dBz. Miller et al. (1988) used CP-3 and CP-4 radars to investigate a severe Colorado supercell. They noted that locations of hail reports were mostly inside the swath of the 55 dBz contour. The M2 microburst reveals that the reflectivity pattern appears to be evolving a bow shaped configuration. The general airflow appears to have a stronger northerly component to the east of CP-2 than the 0.50 km case. As in the 0.50 km case, the areas of strongest outflow are predominately on the north side of the microbursts, where the environmental winds and the microburst winds sum. Also of interest is the confluence zone to the east northeast of the 60 dBz maximum. This feature appears to be channeled flow caused by the interaction of the bow echo microburst complex with a microburst located to the east of the grid. This feature is much better defined at the smaller scale. The pressure pattern shown in Fig. 6.28, maintains the same general pressure pattern as for the 0.50 km case, but pressure gradients are generally 20 to 25% greater. The most striking change is the large pressure gradients that occur on the north side of the outflow areas. These areas reflect the underlying strong small scale wind fields. These wind fields are not resolvable at a 0.50 km

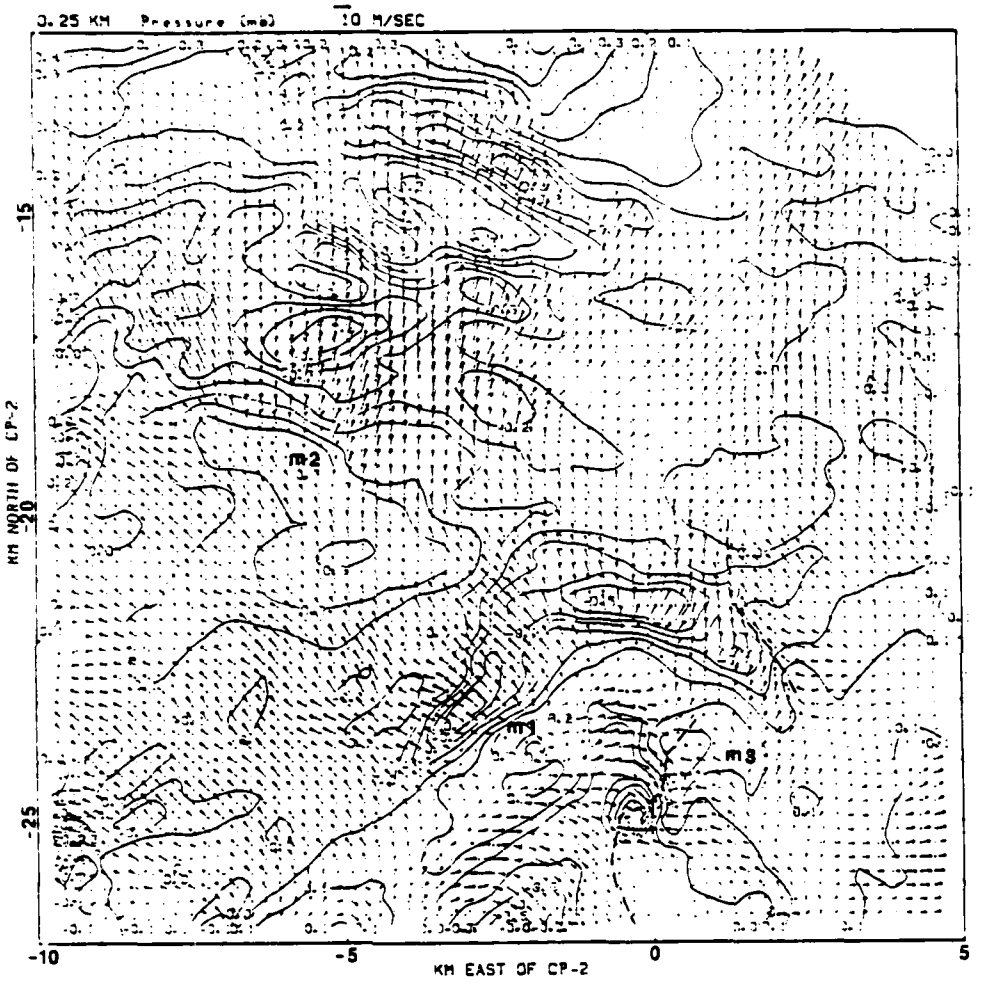

Fig. 6.28 Plan view of the perturbation pressure field, for the 5 August 1982, 1850 MDT case at 0.25 km, for a 0.25 km grid spacing.

scale due to the inherent smoothing of the Barnes (1973) scheme. The gradient in the area north of M2, between the microburst and the maximum outflow winds, approaches 1 mb between M2 and (-6, -17.5). Along the gust front, a sharp pressure gradient and low pressure mark the location of maximum convergence. This same feature has a value of upward motion of 2 m/s for the 0.25 km case (Fig. 6.29); whereas, the 0.50 km case had a value of 1 m/s. Downward vertical velocity of -1.5 m/s is associated with M1 for the 0.25 km grid spacing. The value of -1.0 m/s at the 0.5 km grid scale suggests that the updraft is more sensitive to the change in resolution, probably because the enhanced resolution of the high speed outflow near the outer edges of the microbursts produces enhanced convergence at the gust front boundaries. Additionally, the finer resolution allows for sharper definition and greater discontinuity of the wind flow near the gust front, which will result in greater values of convergence and upward motion. Other features include the confluence line to the northeast of the bow echo, associated with upward motion of 0.5 m/s, and the extreme upper left corner of the grid is an area of upward motion associated with a gust front emanating from M2.

The 0.50 km wind pattern, shown in Fig. 6.30, is essentially the same pattern as occurred at the 0.25 km level. Once again, the areas of strongest outflow are on the north side of

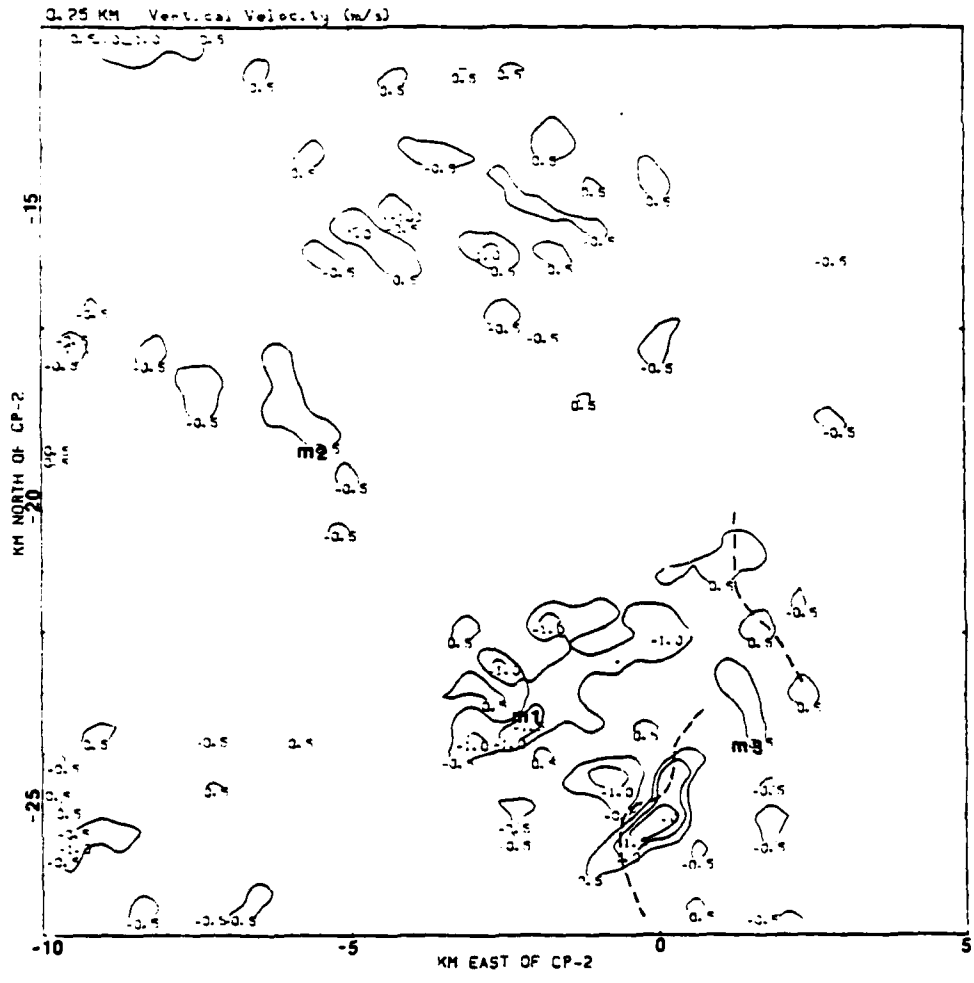

Fig. 6.29 Plan view of the vertical motion field, for the 5 August 1982, 1850 MDT case at 0.25 km, for a 0.25 km grid spacing.

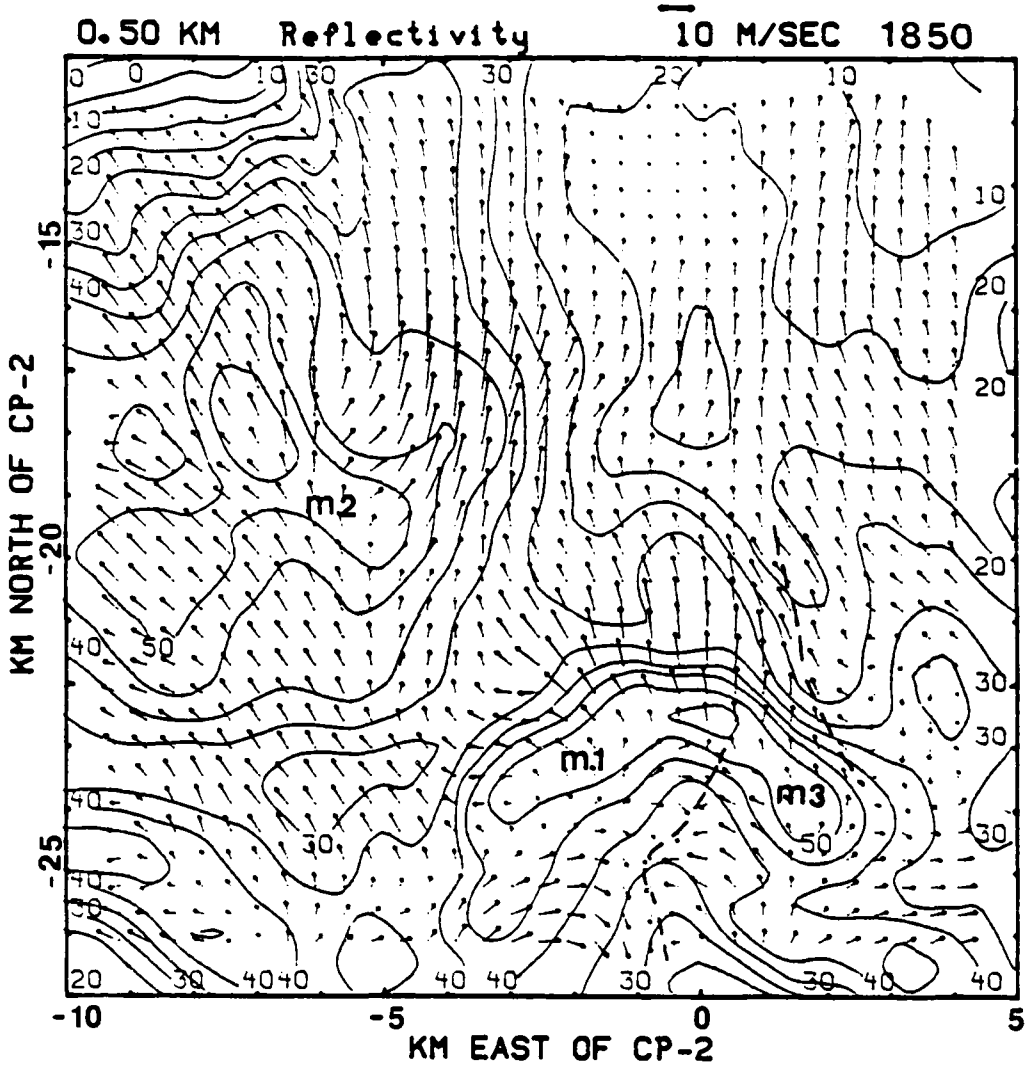

Fig. 6.30 Same as Fig. 6.26, except for 0.50 km.

the microbursts; however, between the outflow from M1 and the microburst M2, the winds are much reduced in magnitude. This suggests that M2 tries to oppose the combined M1 and environmental flow. The microburst M2 has its greatest intensity at this level. The wind flow, in general, is at a maximum at 0.50 km due to the lessened effect of surface friction and the better organization of the microburst. The vertical velocity field (see Fig. 6.31) features the bow echo containing M1 and M3, having a maximum value of -2 m/s near the M1 microburst. An updraft velocity of 2 m/s at (0,-25) is associated with the gust front between M1 and M3. This value is double the value for 1845 MDT. The downdraft M1 is the same magnitude as 1845 MDT, but M3 is assisting in making the bow echo an area of downward motion. A semi-circle of downward motion surrounds the updraft. The intensification of convergence and upward motion at the gust front appears due to M3's intensification. The M3 microburst will create a vigorous outwardly propagating gust front that occludes with the old gust front. At the triple point of the occlusion, the weakened cyclonic circulation is found. While the microburst M2 is not obvious from the horizontal wind pattern, it is more obvious from the vertical motion pattern. Notice how M2 is separated from M1 and M3 by an area of upward motion between the two systems. M2 was not classified as a separate system by storm cataloguers based on the horizon-

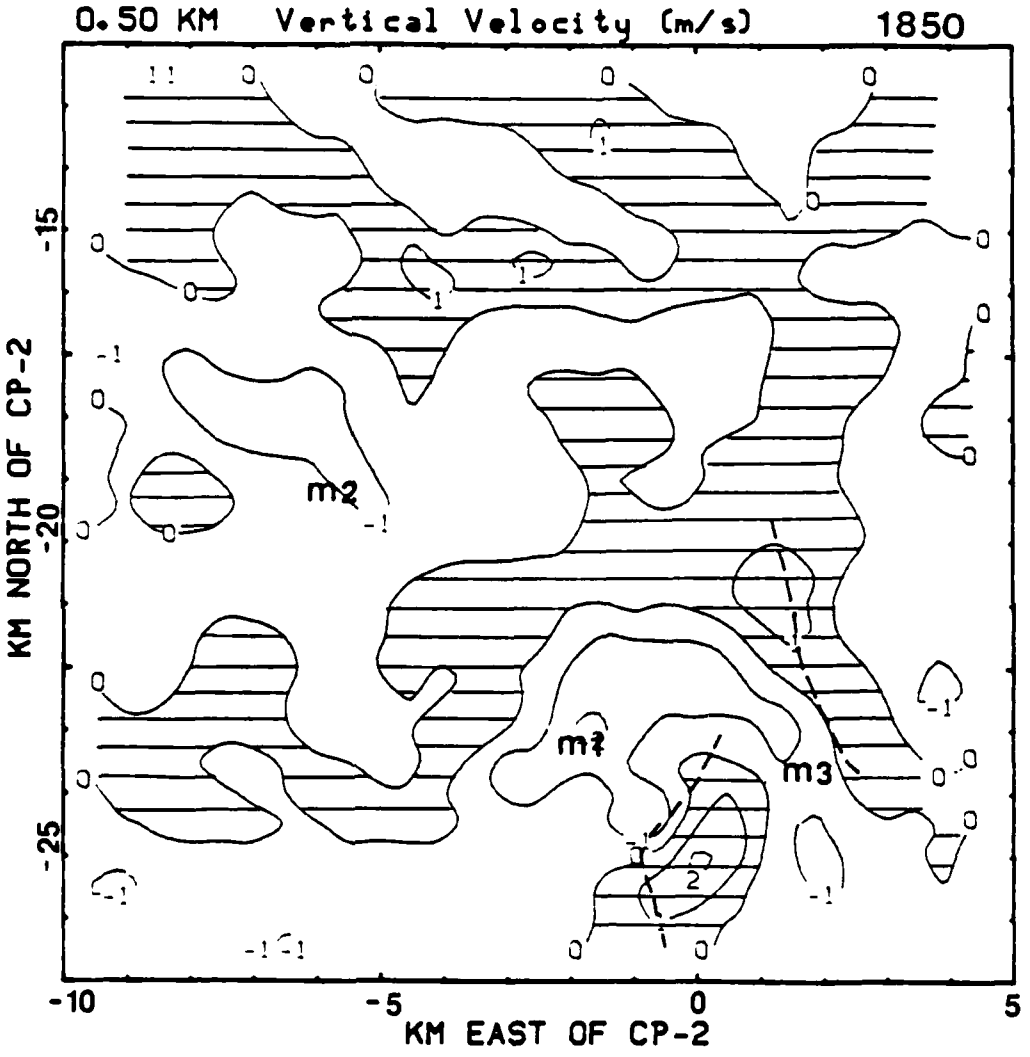

Fig. 6.31 Same as Fig. 6.29, except for 0.50 km and for a 0.50 km grid spacing.

tal wind shear requirements for a microburst. It is apparent from the vertical velocity field that two distinct centers of downward motion are present. Also, two distinct centers of 50 dBz plus reflectivities are noted. The result suggests that the present convention of classifying microbursts is based on the singular, isolated microburst event. A broader definition based on the total storm structure to include the vertical velocity field may prove more accurate. The perturbation pressure pattern at 0.50 (Fig. 6.32), reveals that the highest value of perturbation pressure is located on the upwind side (to the southeast) of the microburst. The pressure pattern reveals that M1, M2 and M3 are distinct systems. The maximum pressure gradient for this case exists between M2 and the low pressure to the north at (-5.5,-16.5). A value of 0.2 mb/km is observed. If tendency is included, the value of the pressure gradient is increased to .4 mb/km, not shown. The inclusion of tendency increased the amplitude of the microburst pressure field. The temperature structure should further define the microburst structure. The temperature pattern at 0.50 km (Fig. 6.33) reveals that the gust fronts are cool anomalies due to upward motion and adiabatic expansion found in the updrafts. The downdrafts are also cool at 1850 MDT, as they were at 1845 MDT. The 14 July 1982 case featured a warm-core microburst. The structural difference that accounts for part of the difference

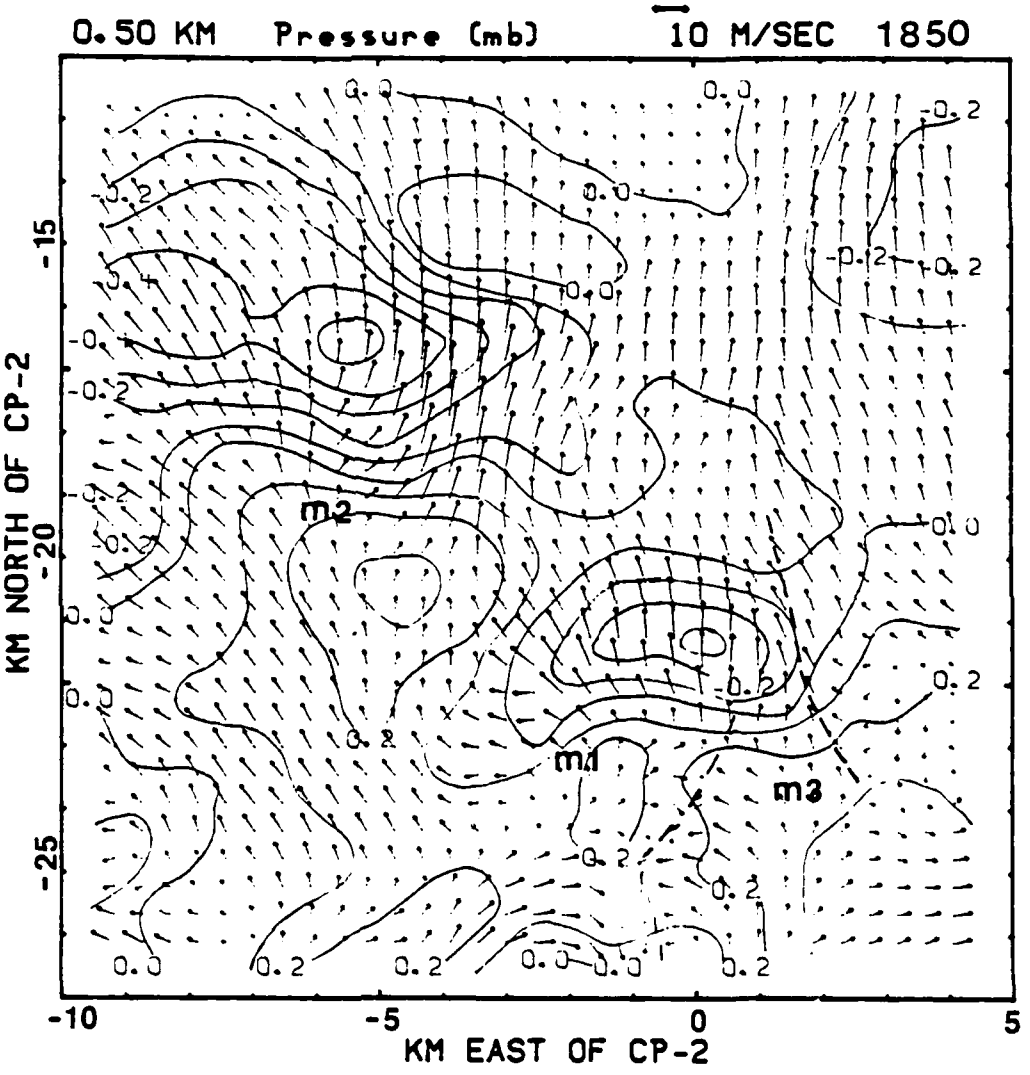

Fig. 6.32 Same as Fig. 6.28, except for 0.50 km and for a 0.50 km grid spacing.

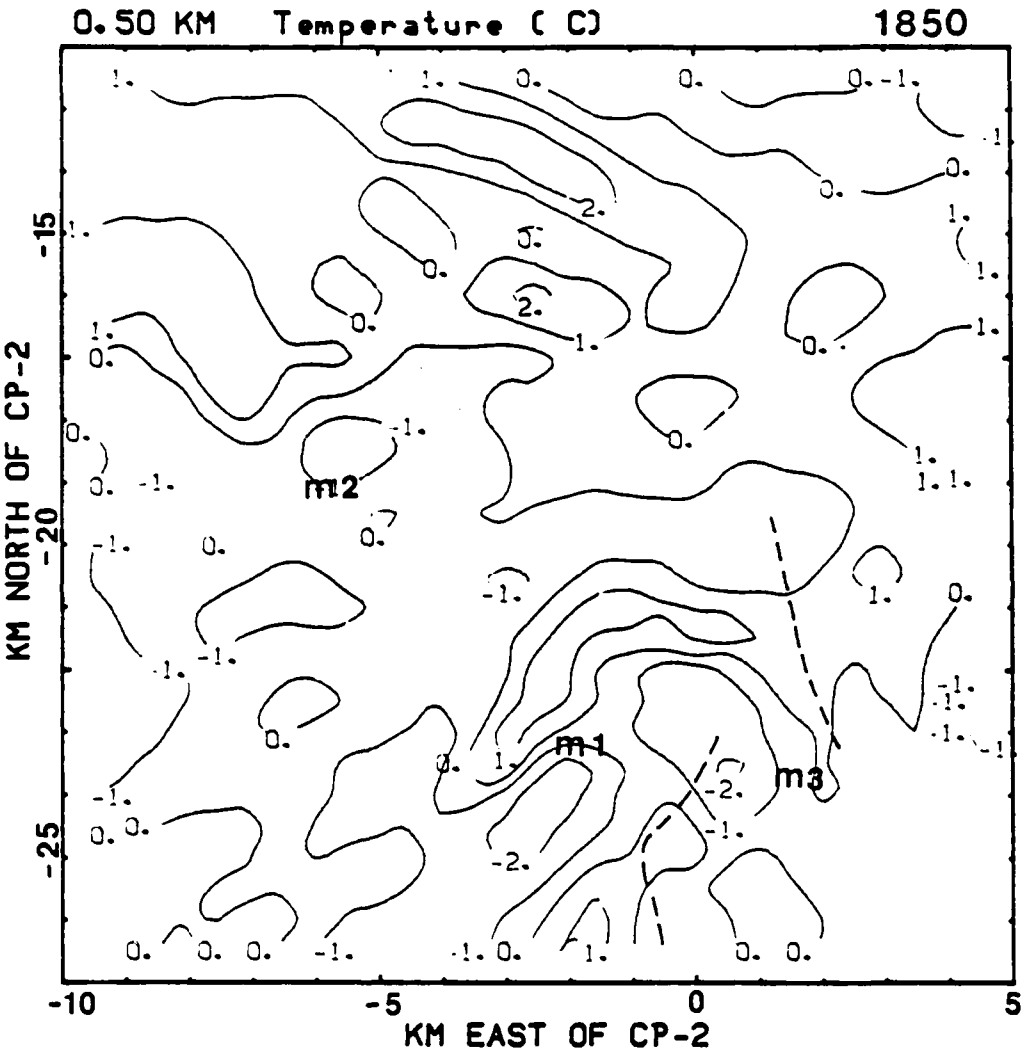

Fig. 6.33 Plan view of the perturbation temperature field, for the 5 August 1982, 1850 MDT case at 0.50 km.

between the two cases seems to be that the 5 August 1982 case features slower descending downdrafts, which allows the environmental dry air and the descending saturated air to mix and evaporatively cool. An additional cause for the discrepancy may include cooling from entrainment of the dry environmental air above 0.75 km, which may induce additional cooling of the updraft. To fully understand the role played by the misocyclone structure, which occurs above the 0.75 km surface layer microburst layer, the higher levels will be examined in turn.

The 0.75 km wind and reflectivity pattern (Fig. 6.34), shows the dominance of the environmental flow. As during the 1845 MDT case, the flow in the inflow region southeast of M1 and northwest of M2 is almost parallel to the reflectivity contours, except at the northern fringe of the M2 inflow. The gust front manages to maintain its structure at this height; whereas, at 1845 MDT, it had largely disappeared. The gust front apparently is enhanced, even at higher levels, by the growth of the M3 microburst. Unlike at 1845 MDT, the misocyclone has appeared at the head of the bow echo at (-3,-24.5) near M1. The descent of the misocyclone to 0.75 km from 1 km suggests that the microburst system has intensified. The greater reflectivity present suggests that as the reflectivity core descends, and the system spins up, the misocyclone can extend to lower levels because the spin up compresses the

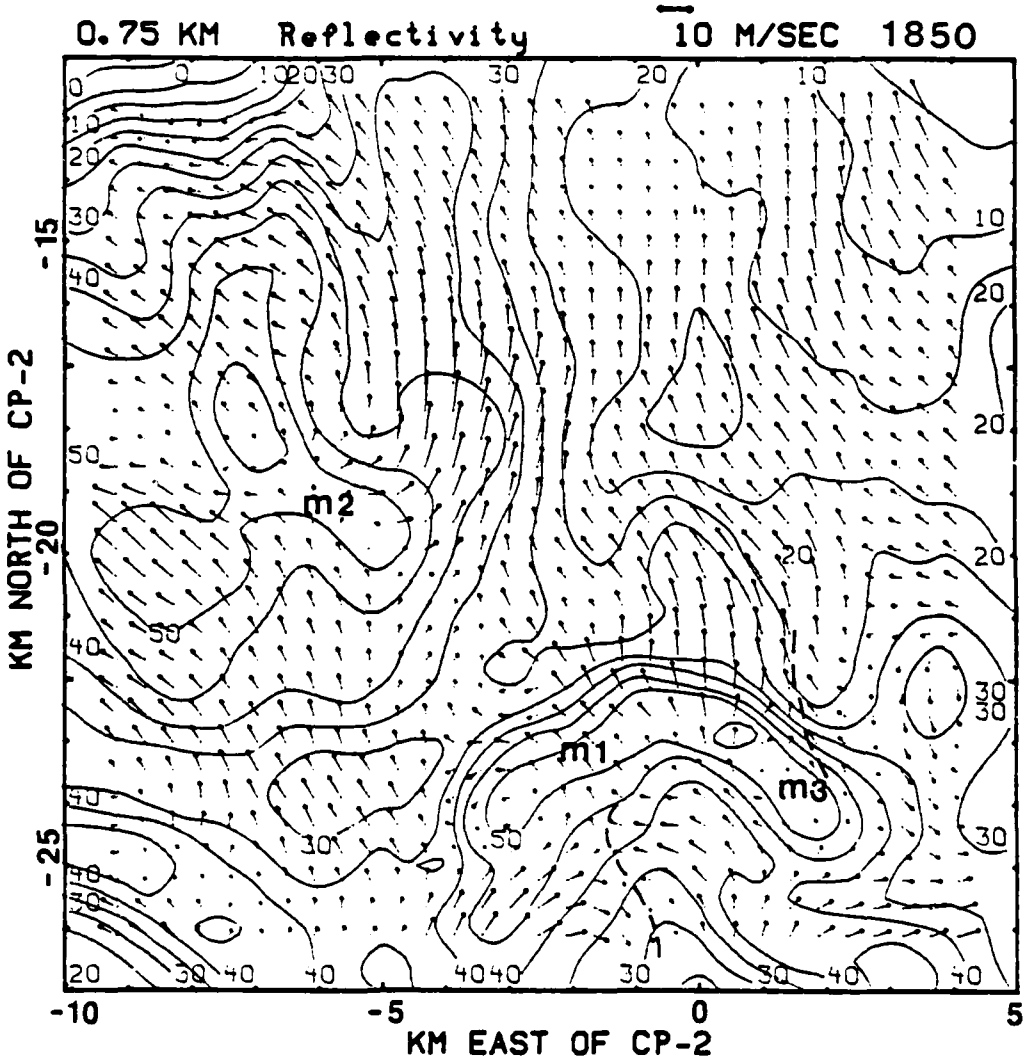

Fig. 6.34 Same as Fig. 6.26, except for 0.75 km.

circulation. The other levels may indicate whether the spin up results or may be induced by increased dry entrainment.

The 1 km wind and reflectivity pattern (Fig. 6.35) shows the increasing dominance of the misocyclone systems on the grid wind field. A cyclonic circulation has appeared, with the center located at (-6,-18.5) near M2, and the misocyclone near M1, at (-3.5,-24.5), is better defined. These features are not coincident with the surface microburst location, but rather tilt westward toward the environmental air, since the misocyclones are located on the stronger gradient of the reflectivity field. M3 has not produced a well-defined misocyclone. The lack of a misocyclone may be due to a time lag between microburst onset and spin up of the downdraft. This implies that the misocyclone does not play a role in the generation of the microburst. It is instead a result of the microburst formation. It may play a role in the maintenance of the storm by entraining microburst air into the downdraft, which it ventilates. The flow has reversed from flow to lower reflectivity values to flow toward greater reflectivity values. The thermodynamic quantities of perturbation pressure and virtual temperature will be examined to determine changes in its structure at the upper levels.

The wind and reflectivity pattern at 1.25 km (Fig. 6.36),

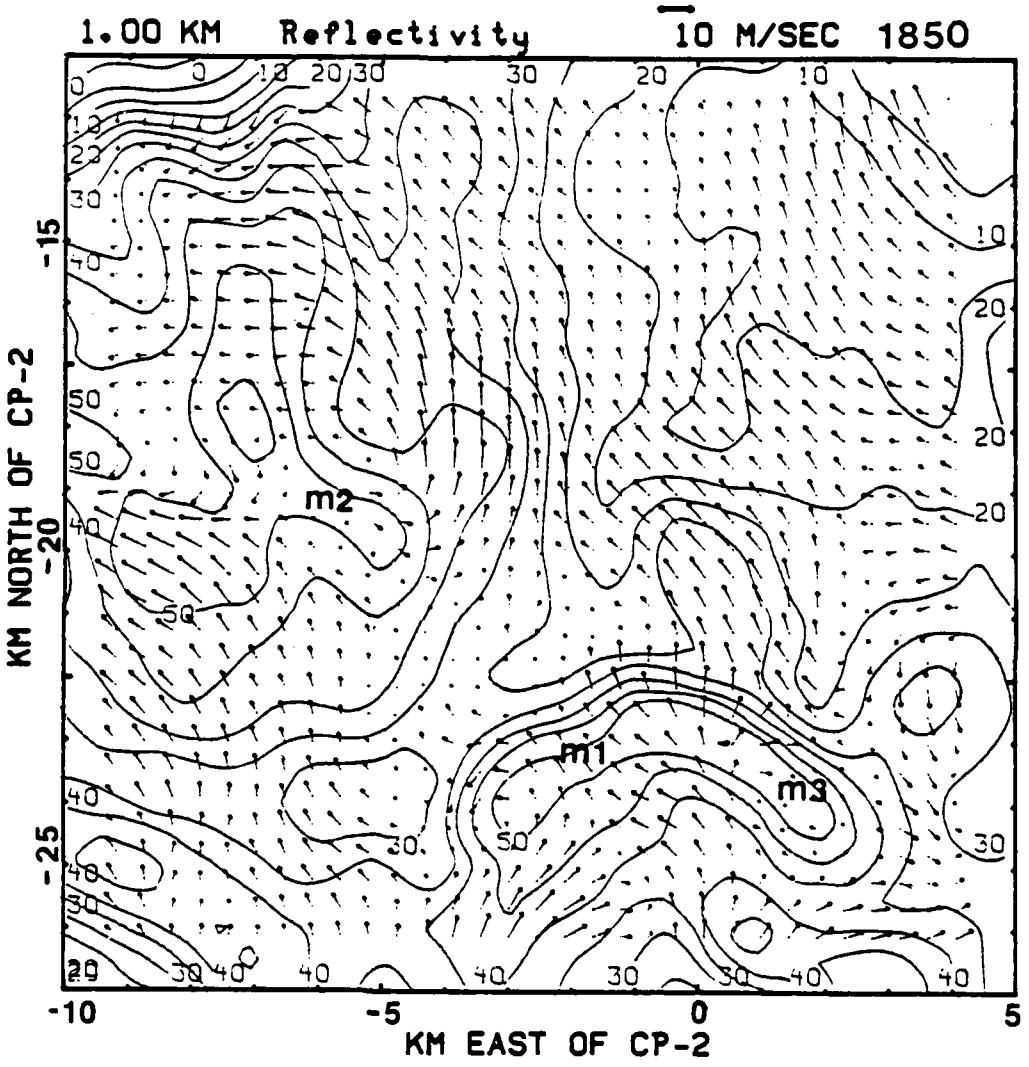

Fig. 6.35 Same as Fig. 6.26, except for 1.0 km.

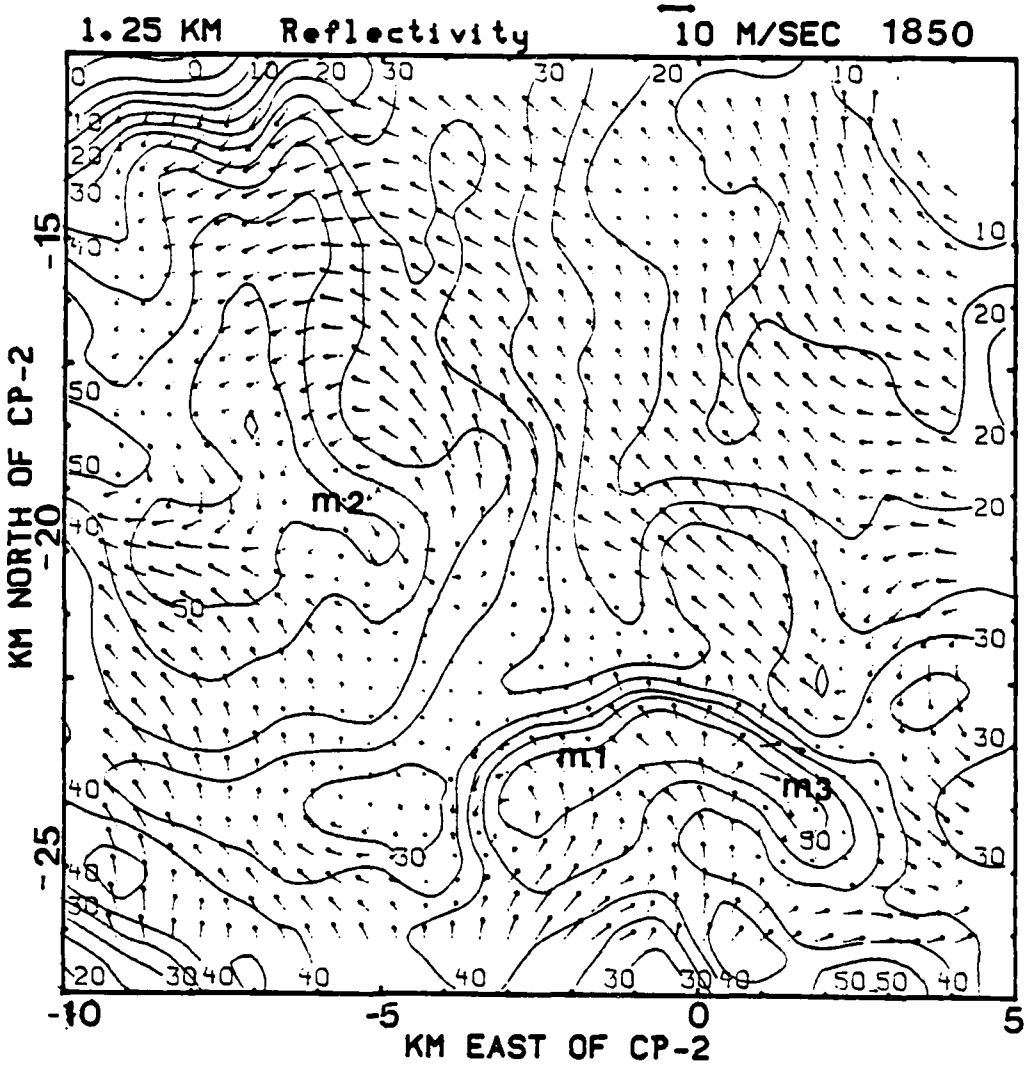

Fig. 6.36 Same as Fig. 6.26, except for 1.25 km.

shows that the misocyclones are now very well organized. The head of the M1 bow echo contains a well-defined misocyclone at (-3,-24.5). Even the M2 microburst has developed a well defined misocyclone, to its right at (-4.5,-19). The increased organization of the microbursts, coupled with the increased value of downward motion and the previously noted descent and compression of the misocyclone suggests that the spin up of the misocyclone parallels the increase in intensity of the surface layer microburst. The microburst systems are therefore intensifying. Additionally, the source region of dry environmental inflow into M2 now includes environmental air from the northeast of the misocyclone circulation. The reflectivity pattern is evolving from an amorphous triangular region at 1845 MDT to a bow shaped reflectivity return. The strong inflow winds to the rear of the bow echoes (south for M1 and east for M2) diminish as they cross the reflectivity gradient. The wind emerges on the other side at only a fraction of its former magnitude. There must be a momentum and kinetic energy transfer downward in the downdrafts to account for this discrepancy. The vertical velocity pattern (Fig. 6.37), shows that the bow echoes are elongated areas of downward motion. The gust front locations at lower levels remain areas of strong upward motion. The microbursts are surrounded by areas of upward motion caused by the influence of lower level gust fronts and other conver-

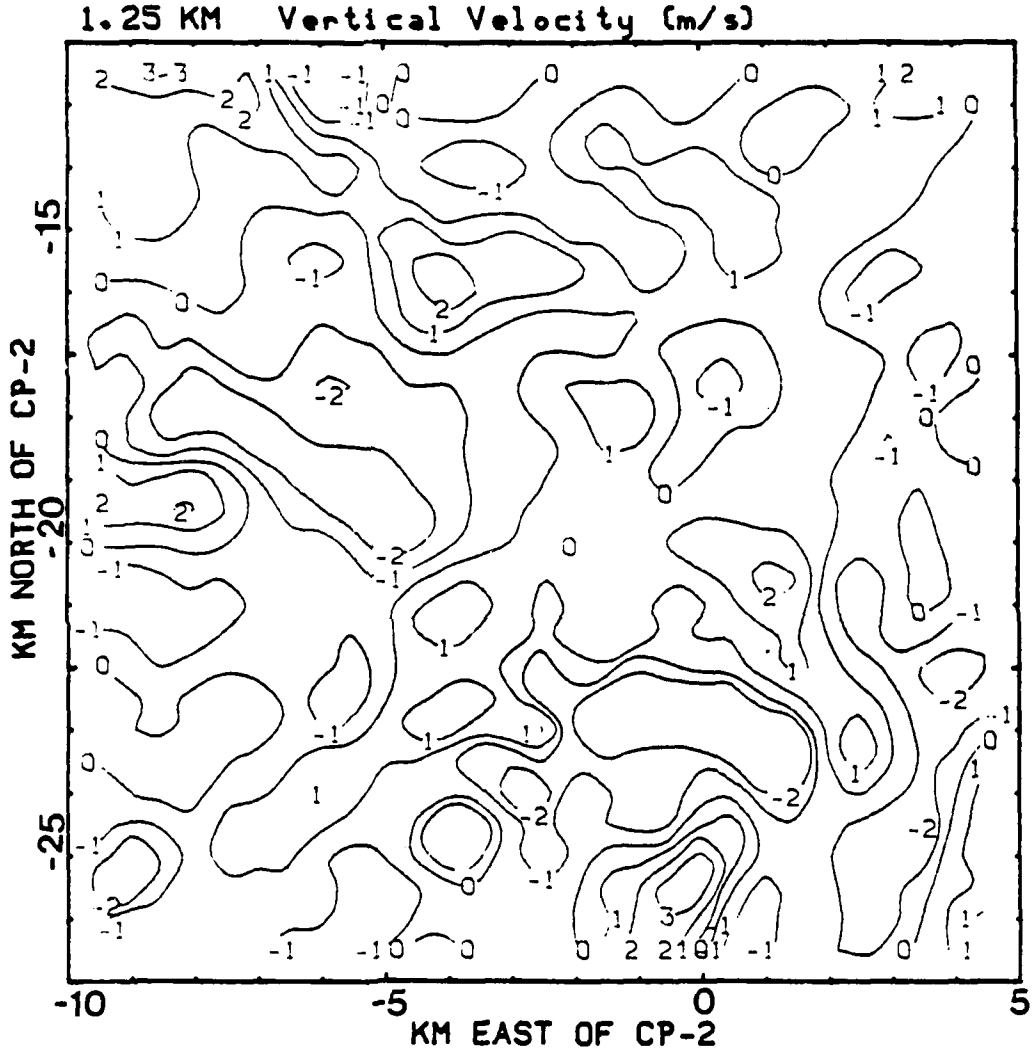

Fig. 6.37 Same as Fig. 6.29, except for 1.25 km and for a 0.50 km grid spacing.

gence zones. The magnitude of the updrafts and downdrafts has increased from the values present at 1845 MDT. The perturbation pressure at 1.25 km (Fig. 6.38) reveals that the misocyclones are accompanied by low pressure and M3 is also an area of low pressure, even though the cyclonic misocyclone is not present. Again, since M3 is just forming, the wind field is unable to adjust to the mass field. Over a span of several minutes, M3 is likely to develop a misocyclone circulation as M1 and M2 have. The dramatic drop in relative perturbation pressure and extensive coverage of the low pressure region suggests that M2 may be intensifying the fastest, which is also reflected in the increased organization of M2. The 1.25 km temperature perturbation pattern (Fig. 6.39) suggests that warm environmental air is channeled in a south to north flow toward the M1 microburst. The center of the misocyclone is warm-cored as the entrained inflow penetrates to the center of the misocyclone. The core is surrounded by cold air. This suggests that the precipitation cooled air mixes with the warm dry environmental air to produce an enhanced area of cold air ringing the misocyclone at its mature state (M1). The newly organized misocyclone (M2) appears to have a bipolar temperature field. One warm, associated with the environmental air, and one cold, associated with precipitation cooling effects, are noted. No evidence of misocyclone occlusion by cold air wrap around is seen. M1 is thought to be

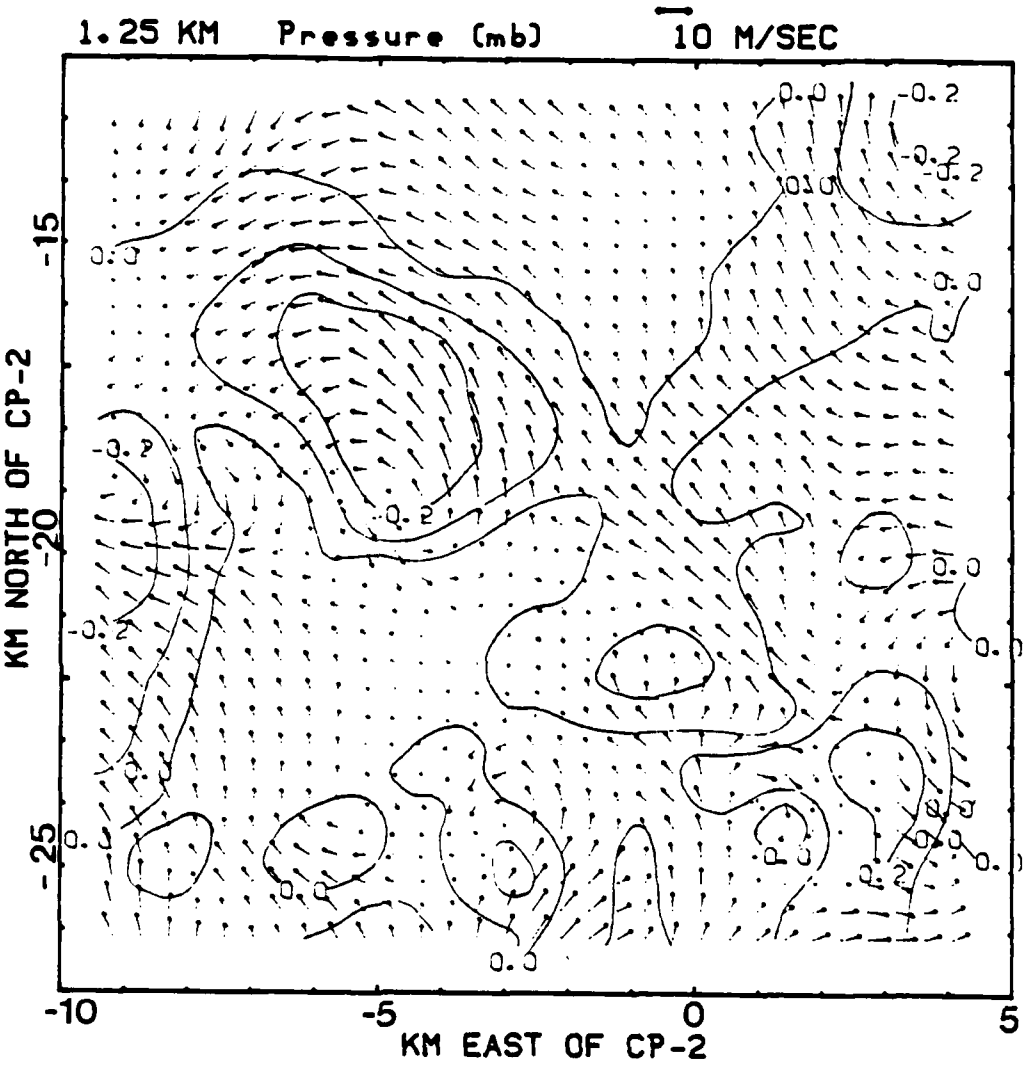

Fig. 6.38 Same as Fig. 6.28, except for 1.25 km and for a 0.50 km grid spacing.

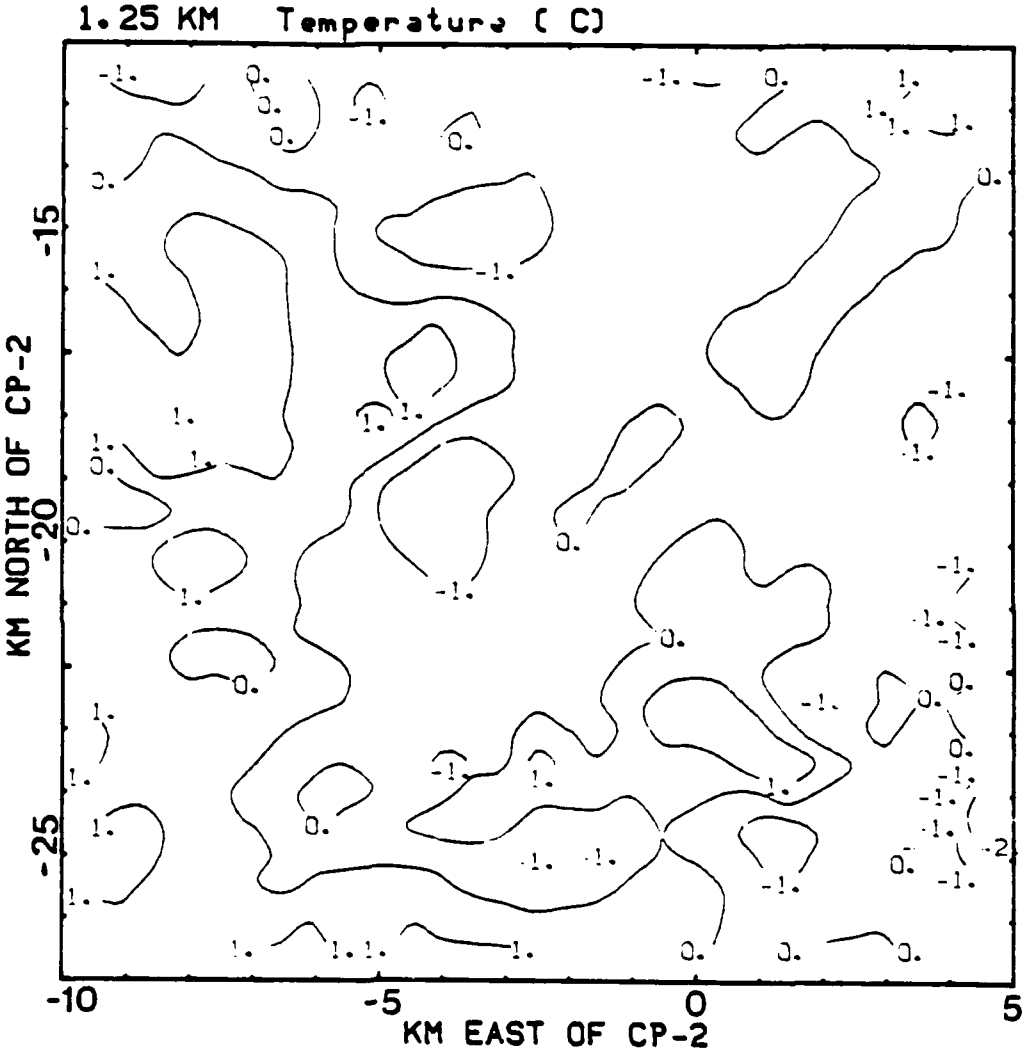

Fig. 6.39 Same as Fig. 6.33, except for 1.25 km.

close to total occlusion and an older entity than M1 or M3. The newly formed diffuse microburst, M3, does not have a well-defined misocyclone at 1850 MDT, but one appears to be forming. The diffuse circulation is cold cored, and is associated with a descending core of precipitation and precipitation cooled air. The thermodynamic quantities for the tendency case, reveals that difference consists of a greater pressure gradient in the tendency case (0.2 mb/km vs. 0.25 mb/km) for a comparable spatial distance across M1 (Fig. 6.40). The perturbation temperature pattern (Fig. 6.41) features a similar pattern as featured in the non-tendency case. The plan view may be complimented by cross-sections through areas of interest to provide a three dimensional view of the storm structure.

6.3 Cross-sections for the Complex Cases

The complex cases require further kinematic analysis to determine the extent of the interactions between the microbursts. Two cross-sections, one from northwest to southeast (NW-SE) and a second from west to east (W-E), were taken across the domain, see lines AB and CD in Fig. 6.13. The following subsections will examine these cross-sections at times 1845 MDT and 1851 MDT, 5 August 1982.

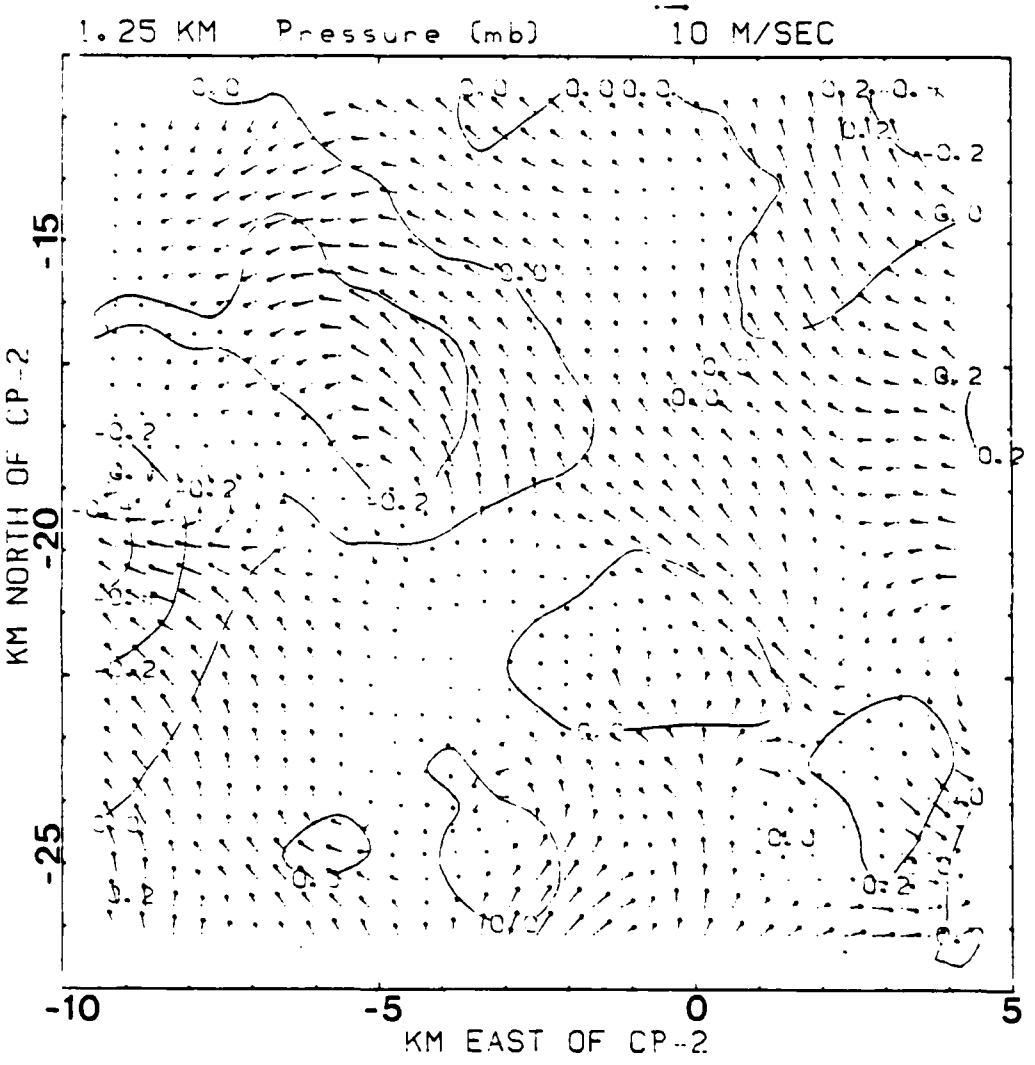

Fig. 6.40 Same as Fig. 6.28, except for 1.25 km with tendency included, and for a 0.50 km grid spacing.

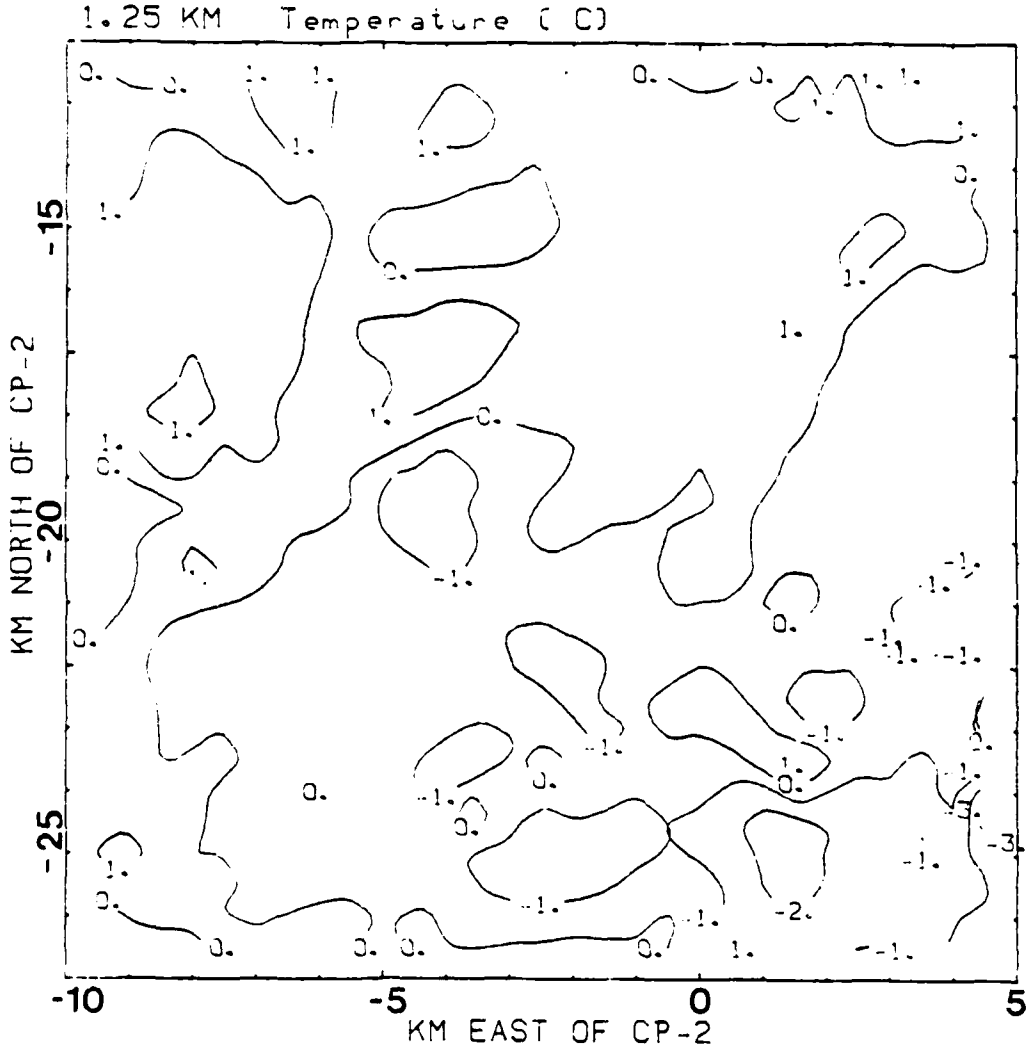

Fig. 6.41 Same as Fig. 6.33, except for 1.25 km with tendency included, and for a 0.50 km grid spacing.

6.3.1 Cross-section NW-SE for 1845 MDT, 5 August 1982

The 1845 MDT wind flow field (Fig. 6.42) shows that the fast flow is generally from the right (southeast) to the left (northwest) with an area between (0,-26) and (-2,-24), where the flow forms a cat eye type turbulent circulation. It is a vortex ring resulted by the interaction between the microburst outflow, and the environmental inflow (e.g., Fujita, 1988; Lin and Hughes, 1987).This circulation is the cross-section of the northern outflow boundary of M1. The horizontally spreading outflow from the microburst acts as an obstacle to the flow, but the flow induced a secondary circulation on the microburst similar to what occurs in separation as flow moves across a valley from an elevated ridge. Notice that at (-6,-19) some evidence of downward motion exists at 1.25 km. The right side of M1 is where the gust front occurs. The convergence is amplified at the surface by the return flow with the secondary circulation. To the left of M1, the flow descends and the secondary circulation accentuates the downward motion. Perhaps if this circulation extends through a deep enough layer, it may induce convection on the right side through focused upward motion and further microburst development on the left side by focused downward motion. The vertical velocity field confirms upward motion (Fig. 6.43) with the gust front on the right side of the microburst at (-0.5, -24.5), and downward motion on the

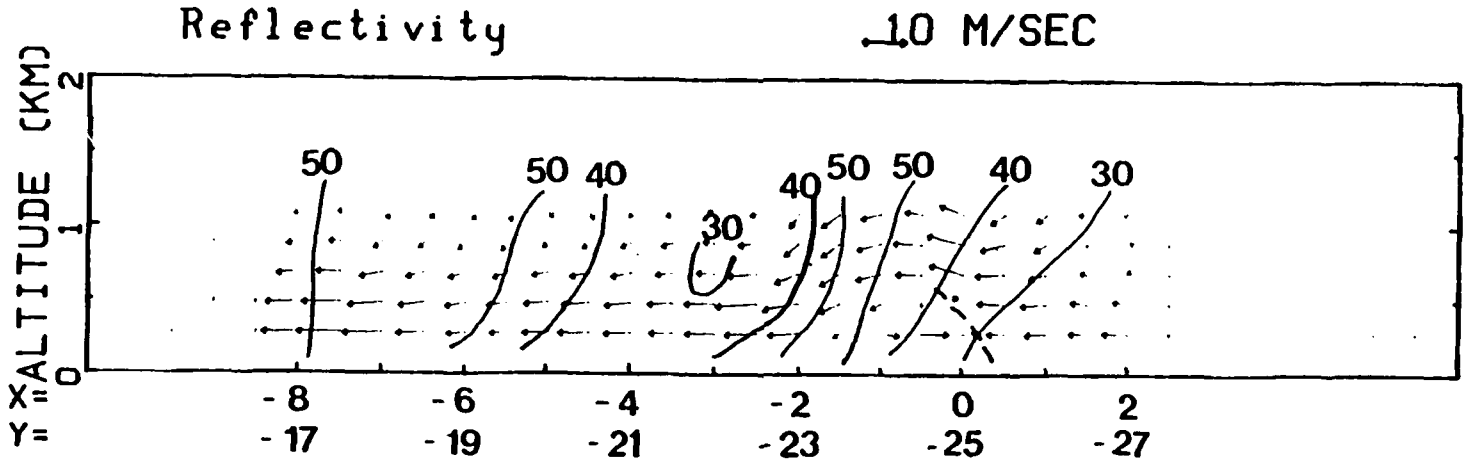

Fig. 6.42 NW-SE cross-section of the reflectivity and wind field, for the 5 August 1982, 1845 MDT case.

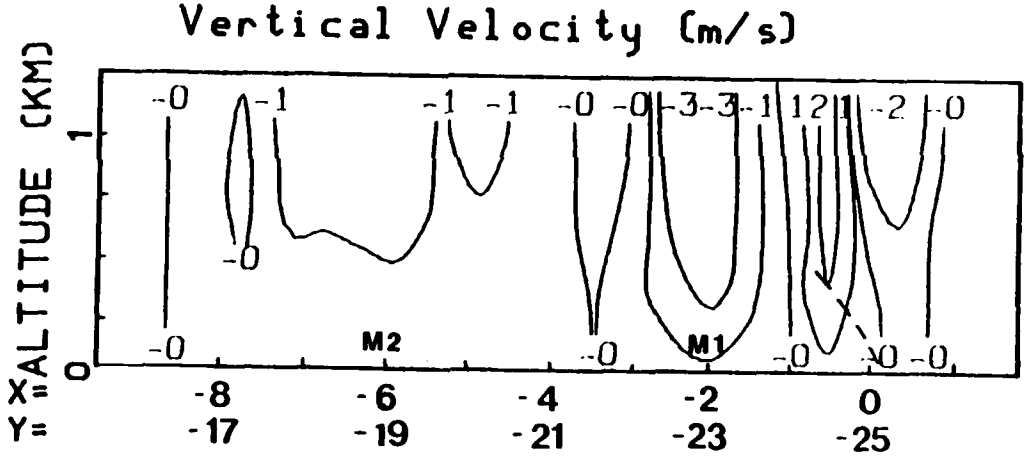

Fig. 6.43 NW-SE cross-section of the vertical velocity field, for the 5 August 1982, 1845 MDT case.

left side at (-2,-23). Another area of weak downward motion exists aloft at (-6,-19), which is associated with the descending and expanding microburst M2. The perturbation pressure gradient (Fig. 6.44) reveals that an area of highest pressure on the right side of the cross-section accelerates the flow to the left, through the strong perturbation pressure gradient between the perturbation pressure high and the low associated with the gust front. Notice that once the flow crosses the microburst outflow it descends and mass accumulates at (-1.5,-23.3). This creates a maximum value of perturbation pressure, which in turn creates a reverse pressure gradient; therefore, the flow reverses from left to right at low levels toward the pressure deficit associated with the gust front. The temperature pattern (Fig. 6.45) also reveals some interesting features. The air to the right of (0,-25) is warm environmental air. As the air enters the gust front it is forced to rapidly rise and adiabatically cool to form a cold pocket up to 0.6 km. As the flow becomes more horizontal west of the most intense cooling, the cooling is reduced and the cold pocket is less intense. Above 0.5 km at (-2.5, -22.5), a warm pocket in conjunction with the descending air. As the air nears the ground, the flow becomes more horizontal and the downward velocity weakens until a cool anomaly is formed near the surface, probably due to an evaporative cooling of the descending air. These patterns will be

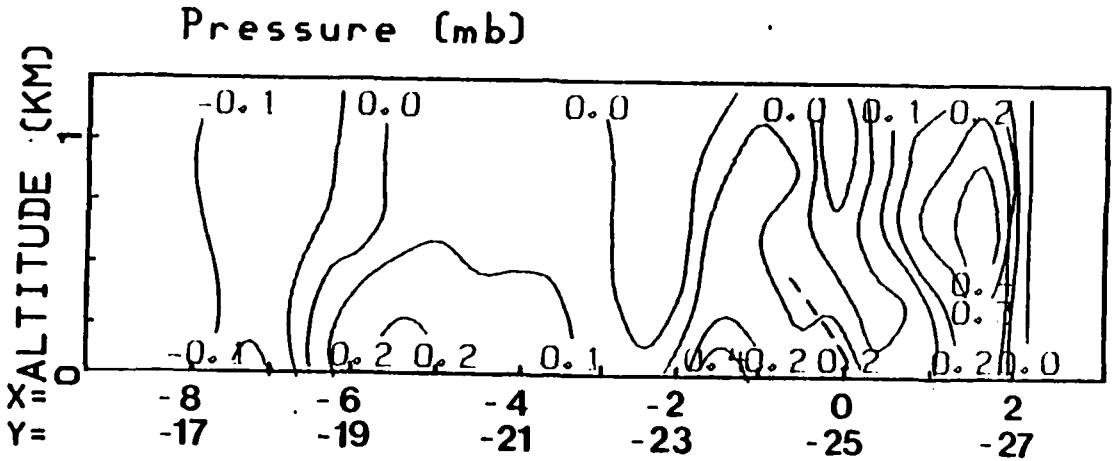

Fig. 6.44 NW-SE cross-section of the perturbation pressure field, for the 5 August 1982, 1845 MDT case.

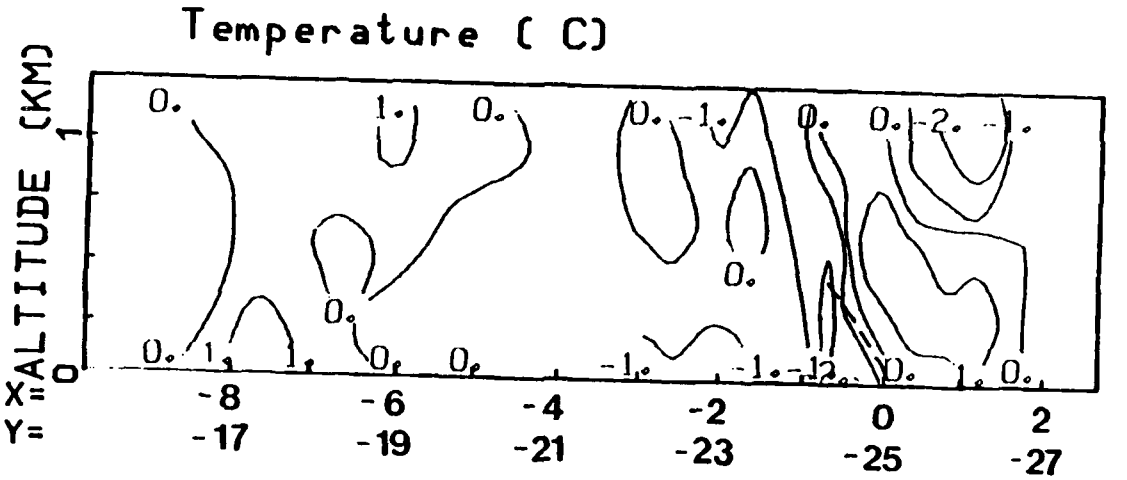

Fig. 6.45 NW-SE cross-section of the perturbation temperature field, for the 5 August 1982, 1845 MDT case.

checked for temporal evolution by examining the same cross-section at 1850 MDT.

6.3.2 Cross-section NW-SE for 1850 MDT, 5 August 1982

The 1850 MDT wind flow field (Fig. 6.46) shows that the cat eye pattern associated with M1 is intact with a slightly more organized circulation. A rotor aloft appears to be forming at (-4,-22) at 1.0 km. This feature forms in conjunction with the descent of M2 at (-6,-20). Note that the microburst's effect on the wind field does not extend to the lowest level. Winds at 0.25 km are still dominated by a right to left component, although winds to the southeast of M2 at upper levels do show convergence at (-5,-21) and a left to right flow. The vertical velocity field (see Fig. 6.47) shows the result of the intensification and organization of M1 and M2. The gust front again shows a +2 m/s value of upward motion. On the other side of the cat eye circulation, a value of -2 m/s occurs. At (-4,-22) the convergence zone between M1 and M2 produces a zone of upward motion, mostly aloft and above 0.5 km. M2 shows a dramatic increase in vertical velocity to -3 m/s at 1.25 km. The pressure pattern (Fig. 6.48) shows that the gust front associated with M1 is shown as a weak trough. The high pressure associated with M1 only extends to 0.5 or 0.75 km. M2 by con-

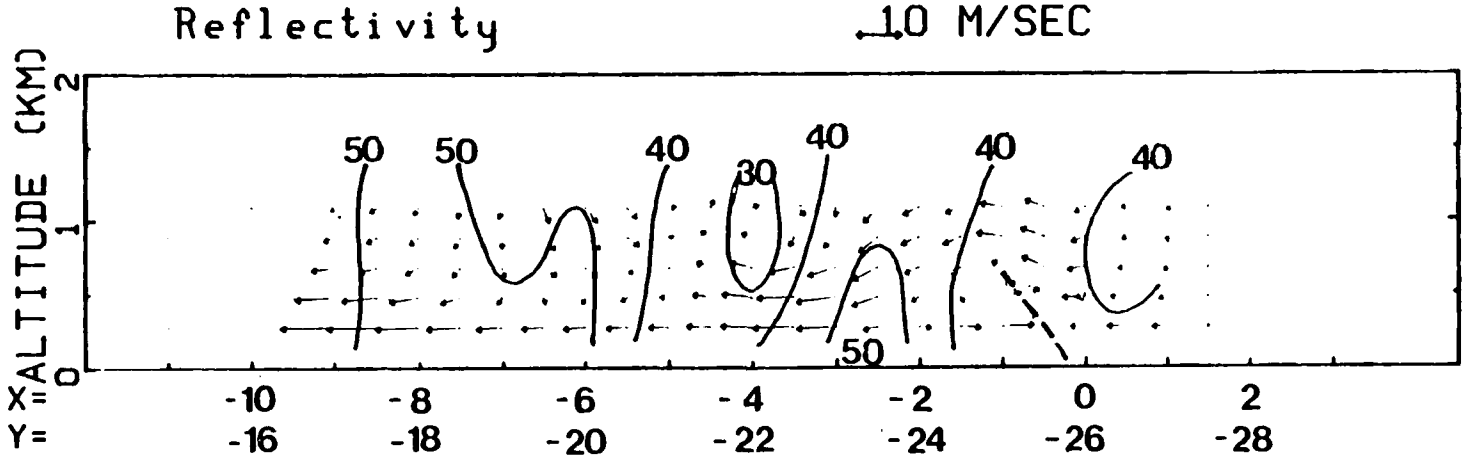

Fig. 6.46 Same as Fig. 6.42, except for 1850 MDT.

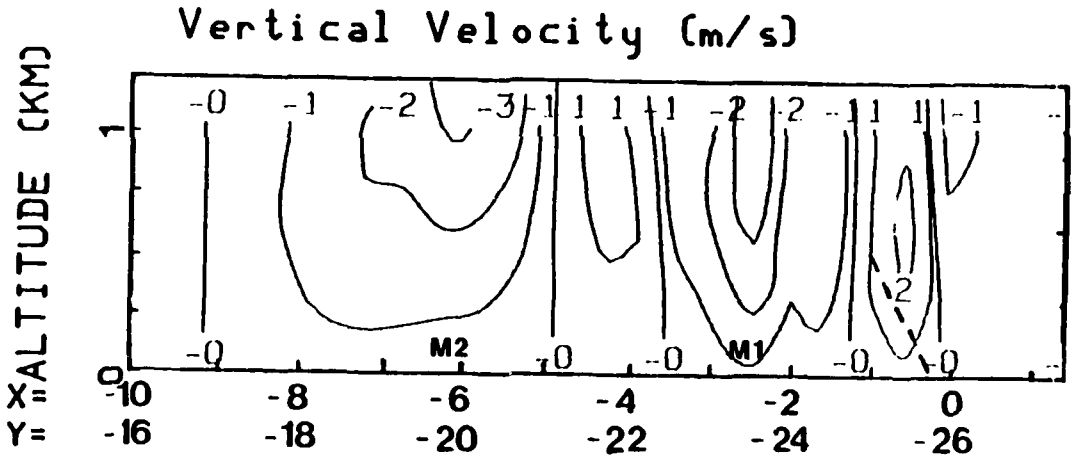

Fig. 6.47 Same as Fig. 6.43, except for 1850 MDT.

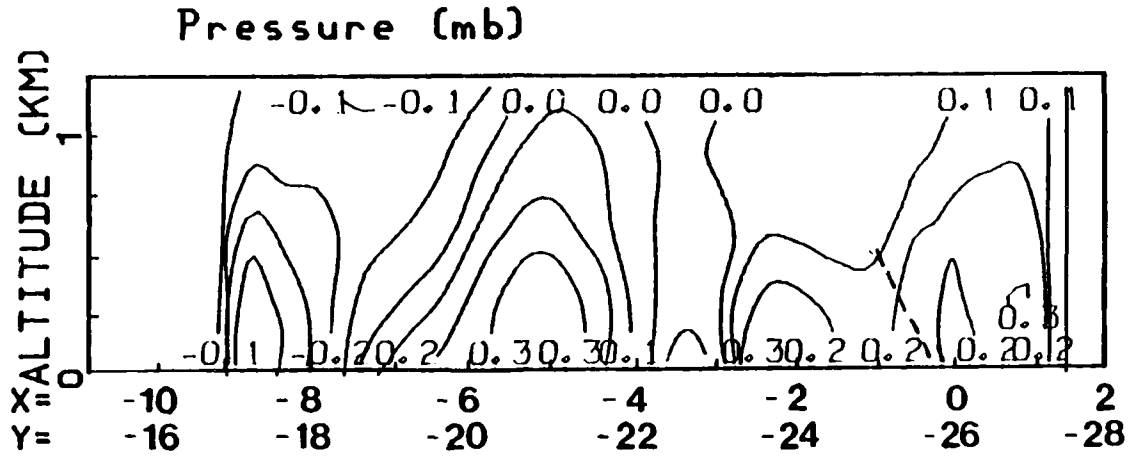

Fig. 6.48 Same as Fig. 6.44, except for 1850 MDT.

trast extends through the entire layer, reflecting the strong downward motion and accumulation of mass through the entire boundary layer. Between M1 and M2 a fairly sharp trough exists. The pressure pattern would predict a convergence between M1 and M2 at all levels, but the convergence does not extend to the lowest level. A possible explanation could be the dominance of the terrain induced flow, which is primarily felt at the lowest level for this terrain. A strong gradient of pressure to the left of M2 accelerates the flow to that direction. The temperature field (see Fig. 6.49) also shows the changes in structure of M1 and M2. The cool perturbation temperature, associated with the gust front near M1, is still present. The convergence zone above 0.5 km and between M1 and M2, reveals a cool pocket, as the rising air cools by adiabatic expansion. A warm anomaly occurs in the downward flowing air in the M1 cat eye circulation. Evidently, the warmer air that was aloft at 1845 MDT has reached the surface and the increased downward motion enhances compressional warming. M2 is associated with an approximate neutral temperature anomaly aloft, but a negative anomaly occurs at lower levels. An explanation for this phenomenon may be that as the air descends from aloft, it mixes at the lowest level, where environmental flow and terrain flow dominate. Mixing at the lowest level ensues as the moist downburst air mixes with the environmental air at the 0.25 to 0.50 km level. The

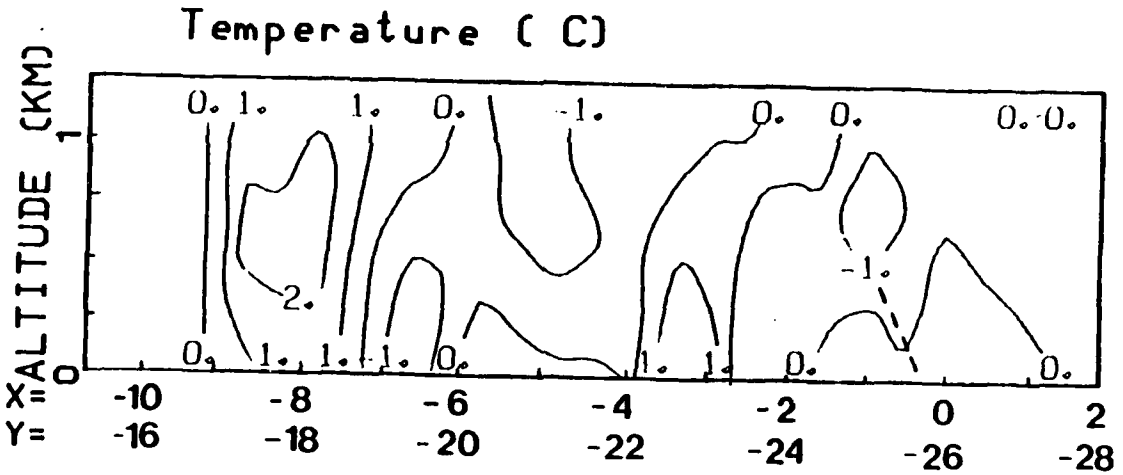

Fig. 6.49 Same as Fig. 6.45, except for 1850 MDT.

results with the tendency included causes a noticeable intensification of the pressure gradient of M1 versus M2 (Fig. 6.50). M2 is approximately the same in magnitude and dimensions. The temperature field (Fig. 6.51) reveals that the cold anomaly associated with the upward motion with the convergence zone between M1 and M2 is intensified by inclusion of tendency. The warm anomaly associated with M1 is reduced and the cold anomaly associated with M2 is also reduced in magnitude but not in sign. An east to west cross-section passing through M1 and M3 will be examined next to investigate the interaction between those microbursts.

6.3.3 Cross-section W-E for 1845 MDT, 5 August 1982

The wind flow pattern at 1845 MDT (Fig. 6.52) for the W-E cross-section shows a right (east) to left (west) flow with an area of strong downward motion at x = -2. The downward motion is associated with the M1 microburst. Note that strong downward motion extends to the top of the layer. Also note that the environment 1 air mixes with, and becomes part of, the downdraft from the right side of the downdraft. The warm dry environmental air contacts the precipitation loaded downdraft, and undoubtably precipitation cooling is the result. The downward rushing air is sufficiently slow to allow environmental

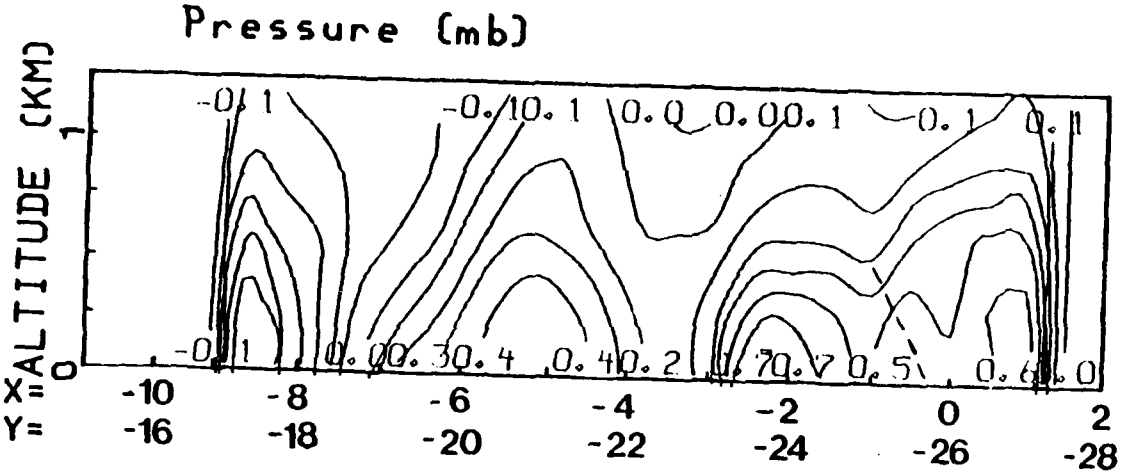

Fig. 6.50 Same as Fig. 6.48, except including tendency.

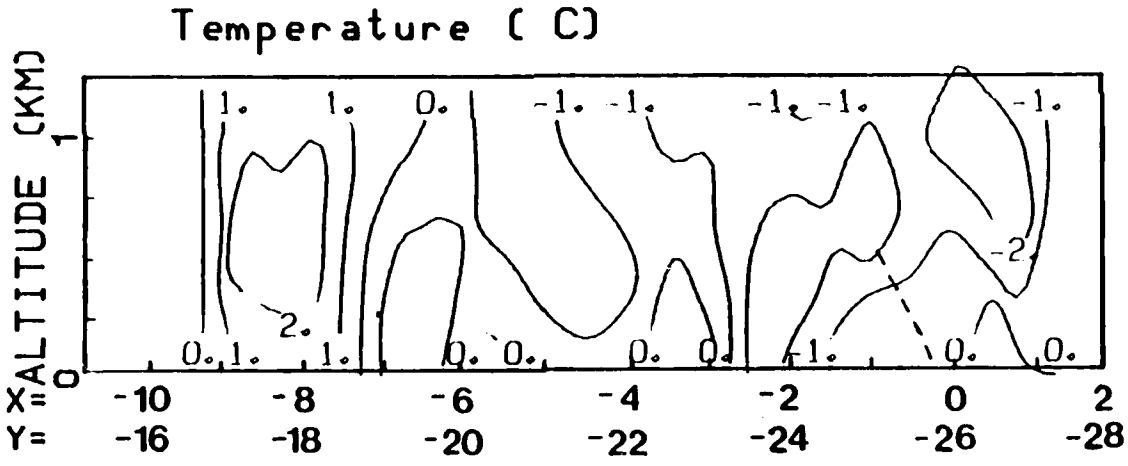

Fig. 6.51 Same as Fig. 6.49, except including tendency.

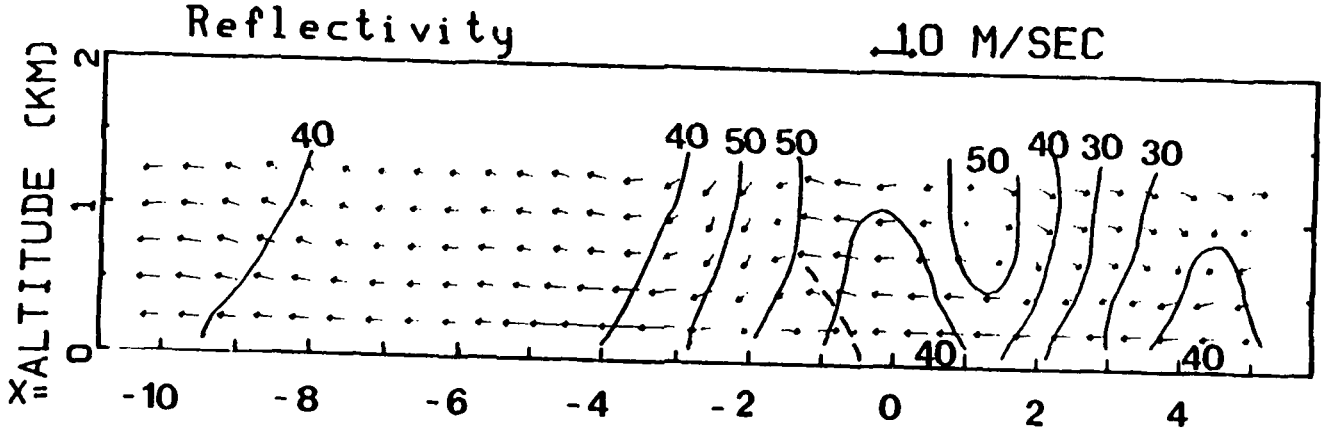

Fig. 6.52 W-E cross-section of the reflectivity and wind field, for the 5 August 1982, 1845 MDT case.

air to enter into the very center of the microburst. The downdraft is not insulated from its environment, because the strong downward flow of greater than -3 m/s present in very vigorous microbursts is not present (Fig. 6.53). Strong flow acts as an obstacle, which effectively insulates the downdraft core from entrainment and the parcel has little time to mix with environmental air. This mechanism was not present in this case. The area to the east of M1 is weakly descending, while the area to the west of M1 is weakly ascending. The vertical velocity field confirms this. A strong downdraft, extending to the surface, is located at -2. Weak downward motion occurs to the east of the microburst and weak upward motion occurs west of the microburst. The pressure pattern, shown in Fig. 6.54, features an area of high pressure on the easternmost side of the cross-section, associated with a microburst immediately to the east of the grid domain (M4, not shown). An area of intense pressure gradient and a large value of positive pressure perturbation is associated with the M1 microburst. Note that the positive anomaly extends upward through the entire layer, rather than remaining confined to a shallow layer, as is typical of a cat eye, roll vortex circulation. Low pressure exists to the left of M1. The pressure distribution would suggest a general flow from right to left across the cross-section. The temperature field (Fig. 6.55) is also very interesting. An area of rela-

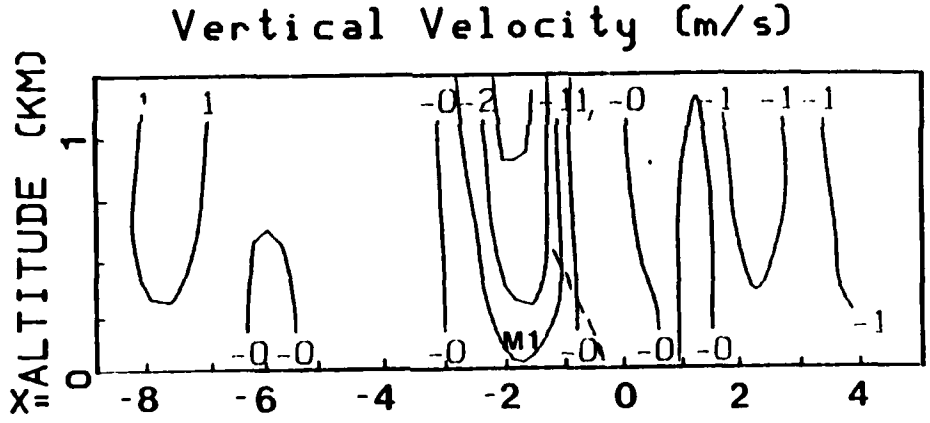

Fig. 6.53 W-E cross-section of the vertical velocity field, for the 5 August 1982, 1845 MDT case.

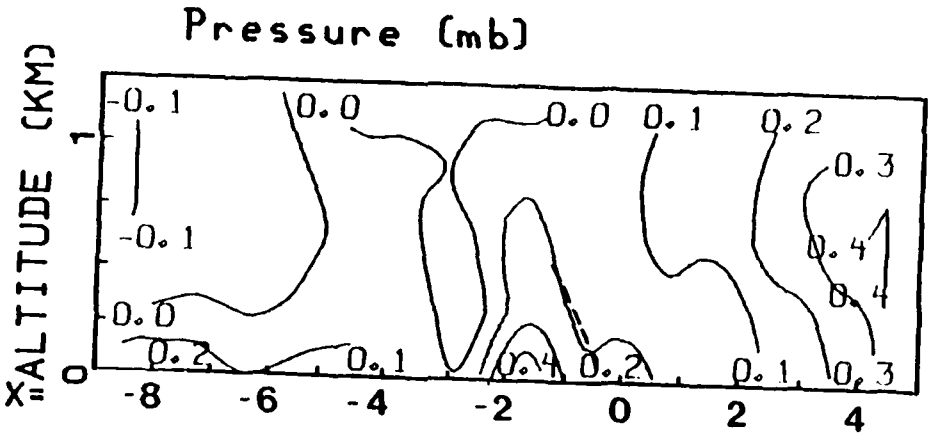

Fig. 6.54 W-E cross-section of the perturbation pressure field, for the 5 August 1982, 1845 MDT case.

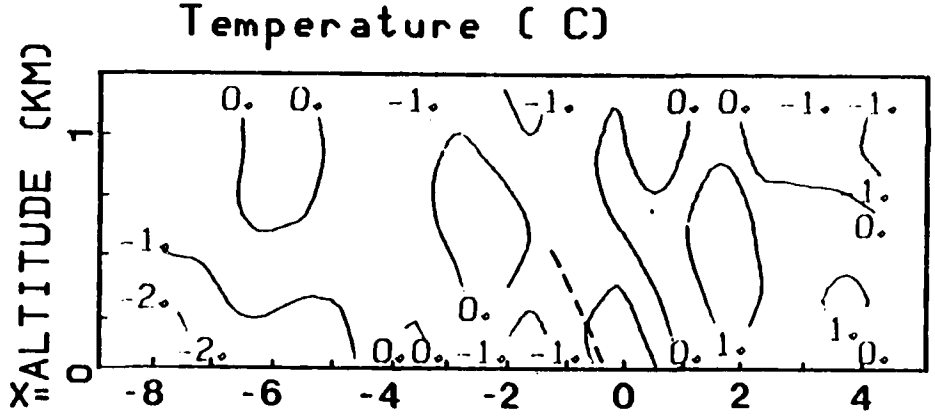

Fig. 6.55 W-E cross-section of the perturbation temperature field, for the 5 August 1982, 1845 MDT case.

tively warm air extends from x = 4 to x = 0. Notice that the prevailing right to left flow advects the warm environmental air into the finger like projection at x = 0 at a height of 0.75 to 1.0 km. A cold anomaly occurs with the microburst downdraft, which is especially noticeable near the 0.25 km level. A much weaker positive anomaly exists in the warmer environmental air west of the M1 microburst. This feature apparently is caused by compressionally warmed, downwardly induced air flow to the lee of the microburst. Obstacle flow is probably the cause. Another cold anomaly exists at the west end of the grid. The origin of this feature is not known. It may be the remains of a previous microburst event. The second time period will be used to document changes in the vertical structure of the microbursts.

6.3.4 Cross-section W-E for 1850 MDT, 5 August 1982

The wind flow at 1850 MDT (Fig. 6.56) is characterized by an increase in turbulent motion, as the microbursts intensify and become better defined. The main microburst, M1, appears to be split into two areas of strong downward motion on either side of x = 0. This twinning may be due to an accumulation of mass at lower levels having a higher density, because mixing with warm dry environmental air will cool as precipitation is

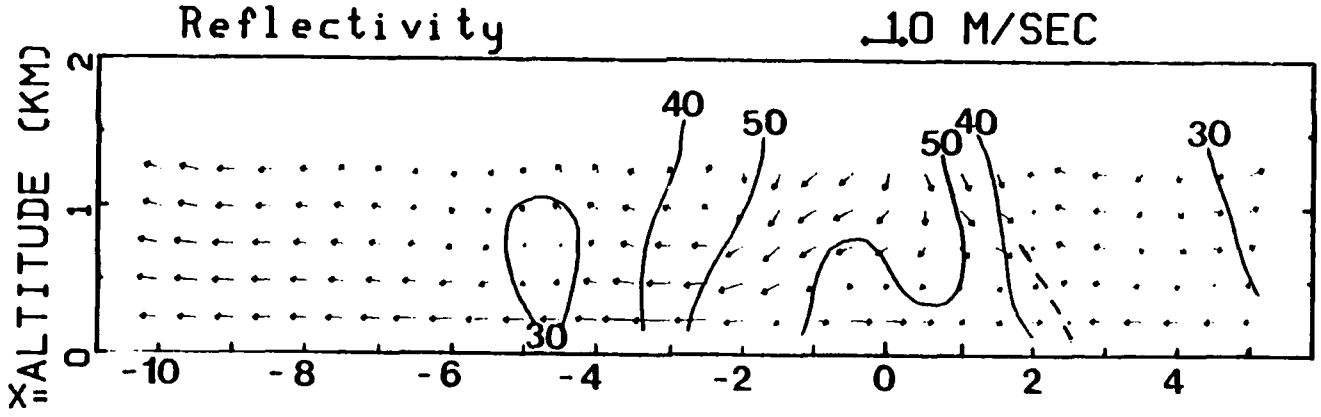

Fig. 6.56 Same as Fig. 6.52, except for 1850 MDT.

mixed with it. The denser air then accumulates at the lowest levels. As warmer lighter air descends from aloft, it flows down the flanks of the pocket of denser air, leaving a relatively undisturbed region at the microburst center. The vertical velocity field, shown in Fig. 6.57, also illustrates some major changes. At x = 4 an incipient downdraft is observed at levels above 0.50 km. This feature is part of the M3 microburst. Another area of weak downward motion occurs above 0.75 km at x = -6. This area corresponds with the outermost fringe of the M2 microburst system. It is likely associated with the downward and inwardly flowing air entrained by the misocyclone associated with M2. At 1845 MDT the misocyclone was very disorganized and this feature was not present. At 1850 MDT it became better organized and larger in area. The vertical velocity depicts, from right to left; (1) an area of weak descending air associated with M4, (2) a narrow corridor of rising motion associated with the gust front, (3) a double structure microburst downdraft, which has increased in magnitude from 2 to 3 m/s ,showing M1 and M3, (4) an area of weak upward motion associated with the gyre between M1 and M2 and (5) the weak area of downward motion between x = -4 and -6 associated with the fringe of M2. The descent of M2 and intensification of M1 has produced a gyre between them aloft at x = -3. A similar event occurred during the evolution of the M1 cat eye circulation and

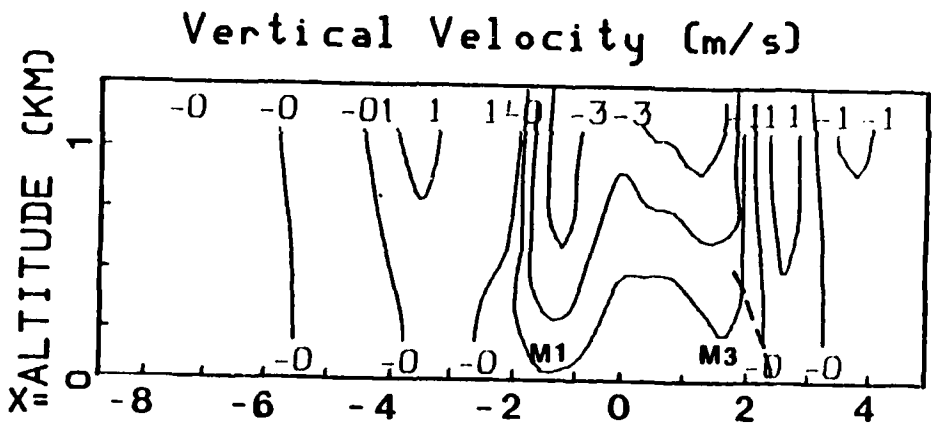

Fig. 6.57 Same as Fig. 6.53, except for 1850 MDT.

M2 microburst for the NW-SE cross-section. Apparently, the gyres and associated strong turbulence develop and maintain themselves when directional shear is established between two microburst circulations. At least for weak microbursts, an interaction between microbursts may be useful in creating gyres and strong turbulence. The strongest turbulence can thus be expected to occur between microburst events at the 0.75 and 1.25 km level. The pressure field (Fig. 6.58) shows a trough at x = 2 extending upwards. The centers of M1 and M2 are located at x = -1.5 and x = 1.5, respectively. The microburst extends upwards to 0.75 km as a distinct system. The temperature field (Fig. 6.59) shows a sharp thermal trough at x = 3, associated with warm air in the updraft region. Above 0.75 km at x = 1, the temperature anomaly is warm. This suggests that the descending downdraft is initially warm, but at approximately 1 km dry, warm environmental air is able to enter and mix with the descending unsaturated air. The evaporatively cooled air becomes increasingly cool as it descends. The pressure pattern with tendency (Fig. 6.60) suggests that M2 is amplified and better defined. The gyre between M1 and M2 becomes defined as a trough of low pressure and the amplitude of the M1 gust front to the east of M1 is less sharply defined. The temperature pattern (Fig. 6.61) confirms the features present in the non-tendency case, and it also increases the magnitude and coverage

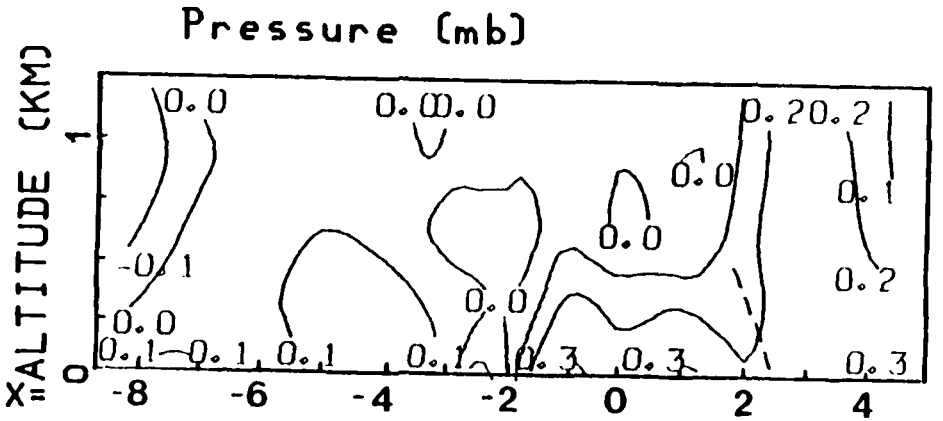

Fig. 6.58 Same as Fig. 6.54, except for 1850 MDT.

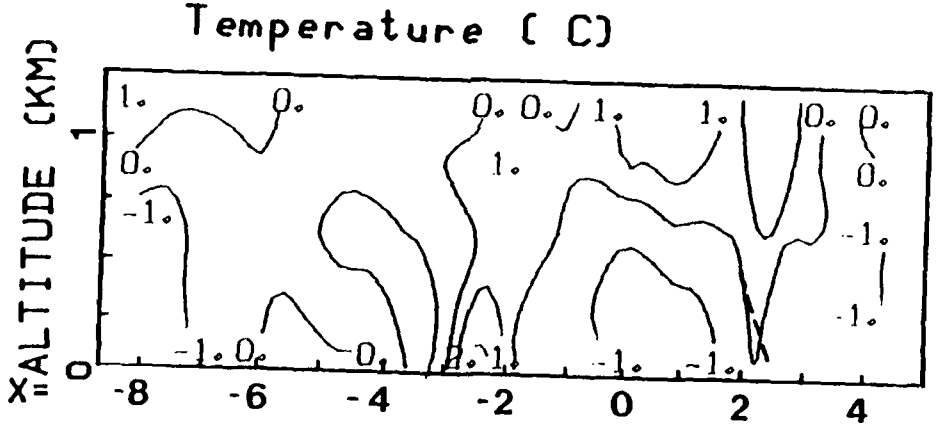

Fig. 6.59 Same as Fig. 6.55, except for 1850 MDT.

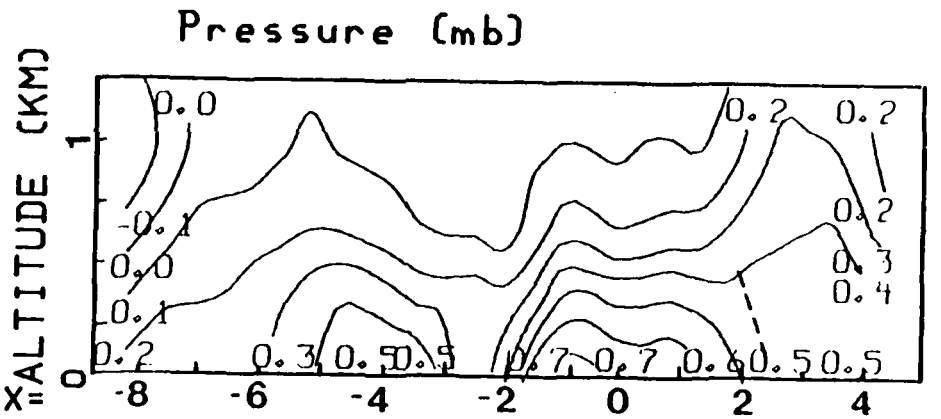

Fig. 6.60 Same as Fig. 6.58, except including tendency.

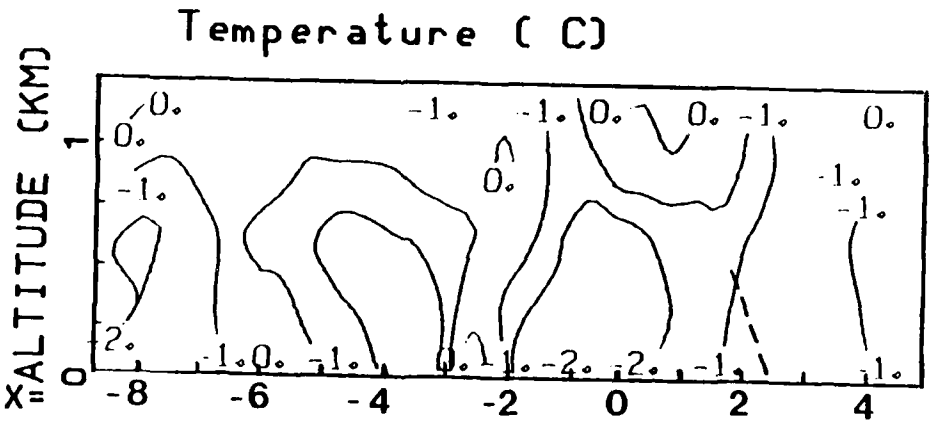

Fig. 6.61 Same as Fig. 6.59, except including tendency.

of the cold anomaly associated with M2.

The three-dimensional view of the microburst for two different time periods reveals an intensifying microburst structure consisting of a descending reflectivity core, accompanied by increasing downward motion. The downward motion is fed by the entrainment of dry, warm environmental air from the upper layers. This high speed air is fed into the bow echo and much of the momentum and kinetic energy appears to be transferred downward in the downdrafts. The initially warm downdraft cores are ventilated by the inwardly spiraling environmental air fed in by the misocyclone. The misocyclone intensifies and becomes vertically compressed as the vertical velocity increases, as the vorticity of the column becomes stretched. The stretched column spins down when the downdraft nears the surface. The cyclonic circulation reaches a neutral point near the 0.75 km level then develops an anticyclonic circulation beneath that point. The 5 August 1982 case contains hail and this may be critical to initiating the microburst in the relatively moist environment of this storm. The 14 July 1982 case may not have any significant amount of hail. This may be expected, since it forms in a drier environment; hence, evaporative cooling alone can initiate and maintain the microburst. The simple case does not have a well-defined misocyclone. This may be due to the fact that the stronger horizontal winds results in a

modification of the misocyclone structure. Both the simple and the complex cases feature entrainment of dry, warm high-speed air into the windward side of the bow echo. The interactions between the microburst and its environment are limited to gust fronts in the simple case. The complex case interactions results in microbursts that enhance gust front developments, development of enhanced areas of upward motion rotors and a microburst embedded in a stronger microburst. These observations may be further justified by examining the results of the eddy kinetic energy budgets and momentum budgets.

6.4 The Momentum Budgets

The momentum budgets presented in this section are for the 1845 and 1850 MDT, 5 August 1982 cases. In addition some comparisons will be made with the 1649 MDT 14 July 1982 case, but the results will not be shown because of the relative simplicity of the result and because of the emphasis placed on the complex case for this research. The cases will be examined in two parts. The first part will consist of the local turbulent eddy momentum fluxes. The second part will consist of the total momentum flux budget, as patterned after LeMone (1983).

6.4.1 The Local Turbulent Eddy Momentum Fluxes

The vertical components of local turbulent u- and v-momentum fluxes (u'w' and v'w') produce a picture of how momentum is being transferred by the turbulent eddies. The following analysis will show how horizontal eddy momentum is being transferred by vertical motion, which features are predominately responsible for the momentum transfer, and how features are temporally evolving.

6.4.1.1 The Local Turbulent Momentum Flux at 1845 MDT

The first eddy flux quantity examined will be the u'w' momentum flux, along the vertical cross-section (see Fig. 6.13). A gain, represented by a positive anomaly centered at 0.75 km, near M1 (Fig. 6.62), is caused by downward motion ($w' < 0$) of westward ($u' < 0$) momentum air. General gains occur in a column of air above microburst M1 for the same reason. To the right and above the gust front (dashed line), a small intense area of loss of momentum occurs. This area corresponds to westward moving air within the updraft, showing the u-component of eddy momentum is being transferred downward ($u'w' < 0$) in the updraft column. The momentum transfer appears to be one of loss (downward) from the updraft region with gain (upward) in the M1 microburst region. Recall from the kinematic analysis of the

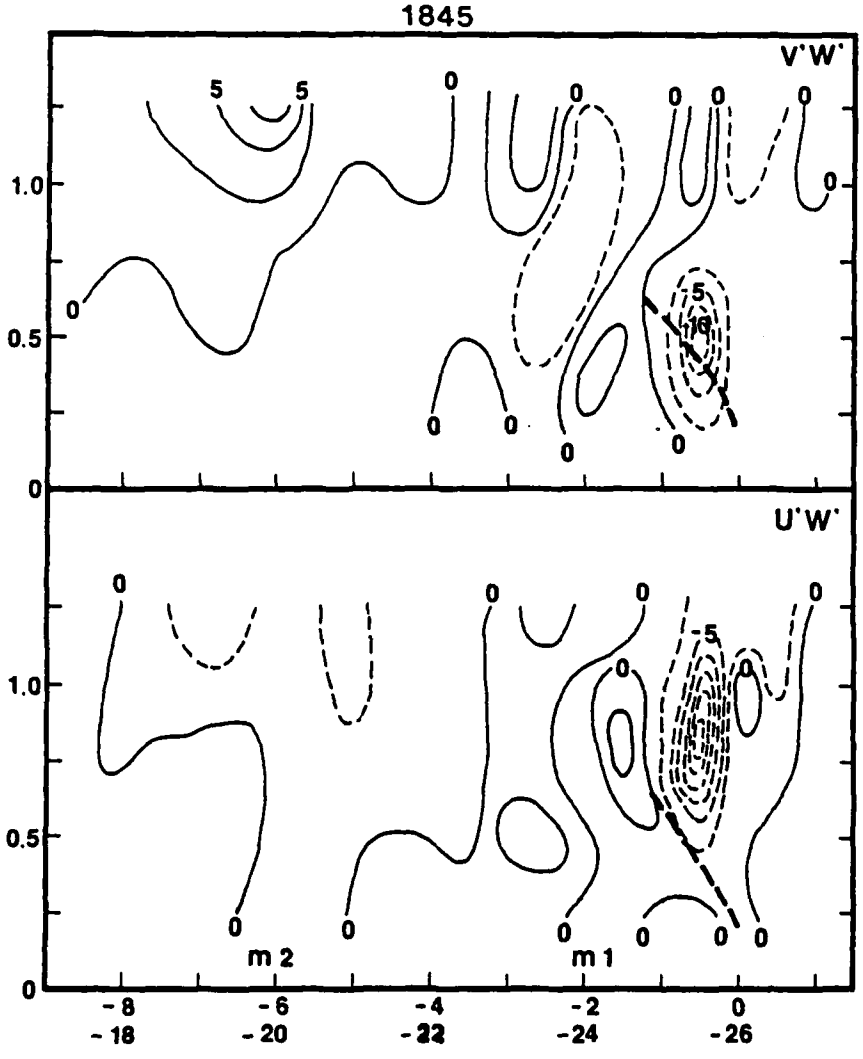

Fig. 6.62 NW-SE cross-section of the u'w' local turbulent momentum flux, for the 5 August 1982 case at 1845 MDT.

Fig. 6.63 Same as Fig. 6.62, except for v'w'.

west to east cross-sections, the area between the loss and gain centers is the area of westward horizontal flow from the loss region to the gain region. The areas of positive u'w' show a discrete maximum within the atmospheric column over M1. The M2 microburst is not very active in terms of momentum flux at 1845 MDT. There is a weak loss of momentum near the top of the domain at 1.25 km, due to the downward motion of eastward moving air.

The v'w' momentum flux (Fig. 6.63) reveals that the gust front is the major sink (downward transport) of v-momentum, as it was for u-momentum. Notice that the sink is at 0.5 km instead of 0.75 km for the u'w' case. Since the gust front is mostly a discontinuity in the v-component of the wind for this case, and the discontinuity only extends to between 0.50 and 0.75 km, the maximum sink occurs at 0.5 km. Also note that a negative value of u'w' above 0.75 km corresponds with a weak positive value of v'w'. This implies some u-momentum may be converted to v-momentum in this area. Notice that within the M1 atmospheric column, a positive value of v'w' occurs at the lowest levels with negative values above. This suggests that v-momentum is lost in the vicinity of the misocyclone, and is transported downward to the lower boundary layer, where the M1 microburst is located. The M2 circulation shows a source (upward transport) of v'w' momentum flux at the highest level,

corresponding to the southward v-momentum ($v' < 0$) being transferred downward within the downdraft column of M2. The kinematic analysis showed a general intensification of the microburst features by 1850 MDT. An analysis of the turbulent momentum fluxes should provide information on how that transformation occurred.

6.4.1.2 The Local Turbulent Momentum Flux at 1850 MDT

The u'w' momentum flux for 1850 MDT (Fig. 6.64) shows that the gust front remains active, but it is no longer the area of greatest momentum flux. The atmospheric column above M2 represents a large sink (downward transport) of u-momentum, indicative of the eastward u-momentum ($u' > 0$) being transferred downward within M2. Most of the loss occurs above 0.75 km with the largest value at 1.0 km. The explosive growth of the sink in u'w' occurs simultaneously with the rapid organization and growth of the M2 misocyclone at those levels. The implication of this development suggests that the downward vertical motion has intensified the removal of mass and momentum from levels above 0.75 km, and transported it towards the surface. M1 has likewise intensified with a large positive u-momentum accumulation near 0.75 km with a weak negative sink in u-momentum near 1.25 km. The v'w' (Fig. 6.65) momentum flux

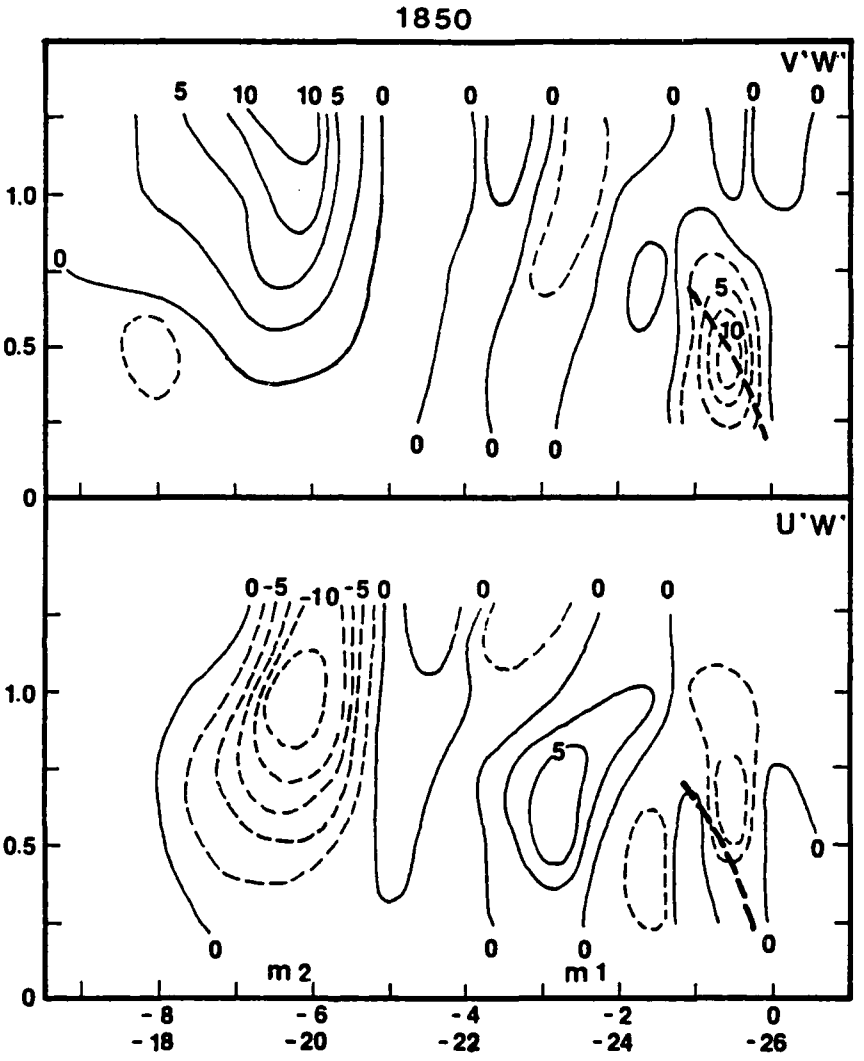

Fig. 6.64 Same as Fig. 6.62, except for 1850 MDT.

Fig. 6.65 Same as Fig. 6.62, except for 1850 MDT and v'w'.

reveals that the large sink of u'w' associated with M2 is coincident with the large source of v'w'. This implies a conversion of momentum from u'w' to v'w' by the misocyclone microburst circulation. The momentum flux v'w' for the M1 microburst seems static in comparison to the explosive growth exhibited by M2. It appears that M1 is more nearly quasi-stationary than M2, and likely near the peak of its development process.

A pattern of general upward or downward flux of momentum for the entire domain may be seen by examining the vertical profiles for 1845 and 1850 MDT (Fig. 6.66). The <u'w'> profile at 1845 MDT suggests a flux of momentum upward to misocyclone levels and downward to the microburst level. This result suggests that the misocyclone is losing momentum, the microburst is gaining momentum, and the mid-level is largely losing momentum with little gain to offset the loss. This result shows that the misocyclone circulation provides momentum to the low levels. The misocyclone circulation is also the site of accumulation, as momentum is transferred from below in the updrafts which is horizontally spiraled inward into the misocyclone circulation. At 1850 MDT the pattern of downward flux to low levels continues with a slight reversal at 0.25 km. The v'w' profile at 1845 MDT suggests a pattern of momentum flux to higher and lower levels, but a general transfer downward is evident. The pattern at 1850 MDT changes dramatically as M1 intensifies.

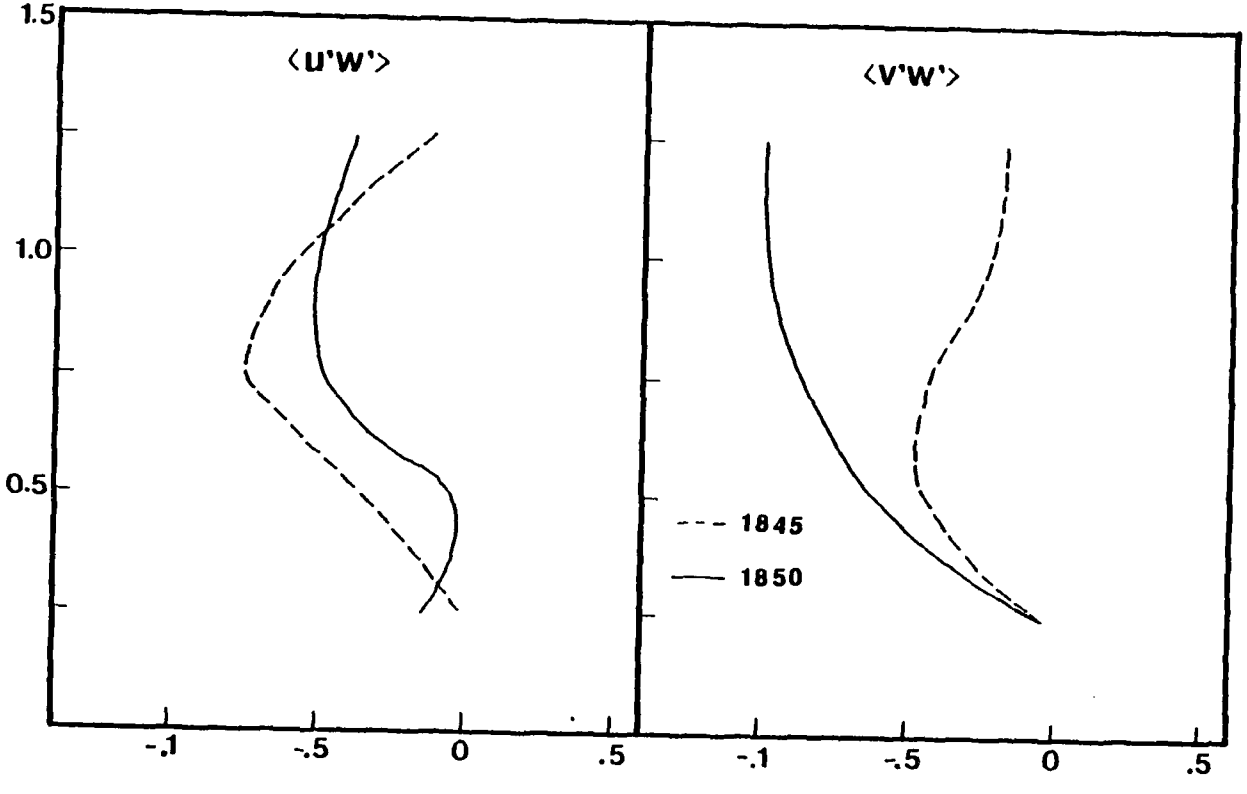

Fig. 6.66 Area mean ⟨u'w'⟩ and ⟨v'w'⟩ profiles for the 5 August 1982, 1845 and 1850 MDT cases.

The slope shows large losses aloft with the smallest or loss at 0.25 km. The pattern coincide with the kinematic analysis. The kinematic analysis showed that the 0.75 km level was virtually devoid of eddy motion, which is predominately composed of the v-component of motion; therefore, u-momentum is predominately present in the turbulent flow above and below 0.75 km, while u-momentum is present at all levels with maximum values present in the strong winds at 0.25 and 1.25 km. U-momentum is continuously extracted from levels above 0.50 km and is added to the misocyclone for transport downward to enhance the eddy motion of the microburst.

While the local turbulent momentum budgets are useful in tracking the sinks and sources of the eddy momentum, a momentum budget containing representations of the underlying physical mechanisms is necessary to determine the source of the momentum transformations.

6.4.2 The Total Momentum Budgets

The momentum budgets, as derived by LeMone (1983), will be used to examine the large scale domain given by the 13 by 13 array within the 15 X 15 km array. A second smaller domain, taken to isolate the momentum budget processes within M1 was taken across a 4 X 4 km array centered on the M1 microburst for

the 5 August 1982 case, and the singular microburst for the 14 July 1982 case. This nested approach may help isolate mechanisms associated with the interactions of the microbursts versus those mechanisms that are important to only the microbursts. The 1845 and 1850 MDT, 5 August 1982 cases will be examined sequentially with comparisons with the 1649 MDT, 14 July 1982 case, which will not be shown.

6.4.2.1 The Momentum Budgets for the 1845 MDT Case

The large domain, momentum budgets at 1845 MDT (Tables 2,3) reveal that the balance in the momentum budget is largely maintained by a balance between the buoyancy term (B), which acts as the source and the pressure velocity interaction term (P) that acts as a sink. Since a large amount of the outflow from the cold-cored microbursts, particularly M1, flows to the west, the buoyancy term is positive at low levels. At misocyclone levels much of the cold inflow is associated with eastward moving air; therefore, the buoyancy becomes a negative, for the v-momentum budget.A different scenario occurs in the v-momentum case with the large warm anomaly north of M1 associated with northward moving air at low levels. The pressure velocity interaction term is a sink for both the u and v-momentum budgets at the lowest two levels. The u-momentum

TABLE 2

Results of the u-momentum flux (u'w') budget calculation, averaged over the whole storm domain (15 x 15 km) for 1845 MDT. Units are in 10^{-3} m^2 s^{-3}.

Z (km)	Term A $\frac{\partial u'w'}{\partial t}$	Term B S	Term C T_r	Term D B	Term E P	Term F D_x	Term G D_y	Term H D_z
0.25	-2.34	0.07	0.69	53.79	-56.83	-0.07	-0.02	0.03
0.50	-4.06	0.44	0.29	18.75	-23.80	-0.01	0.26	0.01
0.75	-3.35	0.29	-0.97	-2.84	-0.73	0.14	0.76	-0.01
1.00	-3.37	0.03	-2.10	-15.28	12.68	0.35	0.86	-0.01
1.25	-4.81	-5.02	-1.12	-16.27	16.70	0.22	0.66	0.00

TABLE 3

Results of the v-momentum flux (v'w') budget calculation, averaged over the whole storm domain (15 x 15 km) for 1845 MDT. Units are in 10^{-3} m^2 s^{-3}.

Z (km)	Term A $\frac{\partial v'w'}{\partial t}$	Term B S	Term C T_r	Term D B	Term E P	Term F D_x	Term G D_y	Term H D_z
0.25	-2.30	0.02	0.63	54.87	-57.83	0.00	0.03	-0.02
0.50	1.75	0.48	0.37	14.97	-14.17	0.26	-0.14	-0.01
0.75	1.54	1.87	-0.26	-11.43	10.97	0.85	-0.47	0.02
1.00	2.10	3.13	-0.84	0.41	0.54	0.86	-0.97	0.03
1.25	2.91	6.77	-0.54	2.59	-4.88	0.82	-1.85	0.00

budget accurately reflects, that at the outer edges of the microburst, upward motion is expected. This does not hold above 0.50 km, because the microburst no longer dominates. The environmental wind, which is predominately northerly in direction, is sufficiently strong to modify the misocyclone circulation in favor of a positive contribution to the momentum budget from the pressure wind interaction term.

The shear (S) and transport (Tr) terms are secondary contributors to the u- and v-momentum budgets at low levels. The transport term features a source in the layer between the surface and 0.5 km, and a sink aloft for both cases. The shear term reveals a source of momentum at all levels except at the highest level. The misocyclone circulation is extracting mean u-momentum from aloft and transporting it downward. The v-momentum shear term is increasingly a source of momentum with height. This suggests that the shear term transports u-momentum, extracted from the mean flow, downward in the microburst/misocyclone circulation. Since the environmental flow is south to north and the environmental component increases with height, the vertical motions associated with the microburst are able to add momentum to the eddy scale from the mean scale to help support the v-momentum budget.

The tertiary contributors to the momentum budgets are the

horizontal divergence of u- and v-transport and the vertical divergence of w-transport. The most significant aspect is that the divergence of u-momentum contributes more positively to v-momentum than the u-momentum budget, and is a sink for the v-momentum budget. This suggests there is an exchange or conversion of momentum between the u and v direction. The larger scale interactions reveal that buoyancy balances the pressure velocity interactions as the main contributors. The secondary contributors of shear and transport reveals that the misocyclone extracts energy from the mean u-wind flow through the shear term, with a gain in v-momentum occurring at all levels as a result of the vertical motion of the updrafts and downdrafts acting on a negative mean v-wind shear. The transport term confirms the results from the local momentum flux. The momentum, both u and v, is being extracted by the misocyclone at upper levels and transported downward to the microburst. What is interesting to note, is that the u-momentum experiences a loss of momentum at all levels, while the v-momentum budget experiences a gain at all levels but the lowest. The microburst influences the domain of interest, but to examine only the microburst structure a smaller domain is required. By examining the microburst structure it may be possible to pinpoint the relative importance of transport in the overall microburst structure.

The M1 microburst momentum budgets (Tables 4,5) reveals that the buoyancy and velocity pressure interaction terms remain important, but the shear and transport terms become primary contributors at the microburst levels. Even the Dx and Dy terms become significant at the misocyclone level. Another development of note is the emergence of the local time derivative term, as a primary term. This confirms that the most rapid changes in the larger scale domain are a result of changes in the microbursts. The microbursts largely dominate the larger scale flow for this meso-γscale domain.

The buoyancy term remains a source for the v-momentum case. It becomes very large below 0.50 km, because the cold temperature anomaly is combined with the strongest southward motion. The buoyancy term for the u-momentum case becomes a negative at upper levels, as the warm anomalies become combined with easterly flow, and the entrainment flow within the misocyclone is predominately easterly. At larger scales the broader westerly inflow dominates. At the smaller scale the constricted inflow near the misocyclone center is easterly and a negative contribution is made. The pressure velocity interaction term behaves in a manner similar to the large scale. The shear term becomes a more important component. It becomes the most important term at the misocyclone level for both budgets. Its basic behavior remains unchanged, but its importance to the budget

TABLE 4

Results of the u-momentum flux (u'w') budget calculation, averaged over the reduced storm domain (4 x 4 km) for 1845 MDT. Units are in 10^{-3} m^2 s^{-3}.

Z (km)	Term A $\frac{\partial u'w'}{\partial t}$	Term B S	Term C T_r	Term D B	Term E P	Term F D_x	Term G D_y	Term H D_z
0.25	-2.82	0.07	0.22	56.01	-59.21	0.07	0.00	0.02
0.50	-3.84	0.44	0.03	16.42	-20.98	0.13	0.14	-0.01
0.75	-2.62	0.28	-0.82	-2.34	0.07	-0.15	0.37	-0.04
1.00	-2.70	0.03	-1.83	-14.31	12.87	-0.16	0.70	-0.01
1.25	-4.15	-4.69	-1.11	-17.10	17.95	-0.01	0.81	0.01

TABLE 5

Results of the v-momentum flux (v'w') budget calculation, averaged over the reduced storm domain (4 x 4 km) for 1845 MDT. Units are in 10^{-3} m^2 s^{-3}.

Z (km)	Term A $\frac{\partial v'w'}{\partial t}$	Term B S	Term C T_r	Term D B	Term E P	Term F D_x	Term G D_y	Term H D_z
0.25	-3.44	0.02	0.45	61.81	-65.76	0.02	0.04	-0.01
0.50	0.61	0.48	0.07	13.03	-12.95	0.05	-0.08	0.02
0.75	-0.26	1.81	-0.54	-13.52	12.02	0.00	-0.10	0.07
1.00	0.53	2.96	-1.08	5.94	-7.68	0.05	0.29	0.05
1.25	3.41	6.33	-0.71	12.97	-15.84	-0.01	0.66	0.01

increases, particularly at the misocyclone level where the vertical velocity increases. The transport term also becomes a major contributor, particularly at the misocyclone level. This development confirms the role of the misocyclone, as a transporter of momentum downward within the larger circulation. This implies that the misocyclone is a gatherer and transporter of momentum downward. The importance of Dx and Dy in the respective budgets of the u and v-momentum budgets at the misocyclone level suggests that a large amount of turbulent exchange occurs there. More importantly, the role of Dx and Dy in the respective u and v-momentum budgets is reversed from the large scale case. The Dx term becomes a source for the u-momentum budget, and Dy becomes a source for the v-momentum budget. Apparently, there is a scale interaction between the microburst/misocyclone system, and the larger scale environment within this term. The environment dominates at the large scale, where a momentum exchange between the u and v-momentum budgets occur. At the microburst scale, the exchange between budgets does not appear to be present at the misocyclone level, but rather a direct gain or loss of momentum occurs within the same directional scale.

The results of this examination may be further substantiated by examining the second time period, 1850 MDT.

6.4.2.2 The Momentum Budgets for the 1850 MDT Case

The large domain budgets at 1850 MDT (Tables 6,7) confirms the results from the 1845 budgets. The buoyancy term balances the pressure velocity interaction term. The shear and transport terms are secondary contributors and the divergence terms (Dx, Dy and Dz) are tertiary terms. Even small scale features, such as the extraction of u-momentum by the shear term at microburst level, remains virtually unchanged. The main points of interest are therefore the differences. A major difference is the weakening of the magnitude, but not the sign of the transport term. This suggests that either the intensification of the microburst, accomplished by enhanced downward transport from misocyclone levels may be leveling off or a counter circulation has developed. The main intensification phase of the microbursts, particularly M2, may be over by 1850 MDT. M3 is developing at 1850 MDT, but it is such a small feature that M1 and M2 dominate the budget. Another difference is the reversal of the role that Dx and Dy play in the momentum budgets. The Dx term now contributes positively to the u-momentum budget and Dy contributes positively to the v-momentum budget. This may be due to the expanding and intensifying microbursts dominating these processes at the expense of the environment, or perhaps a reversal of roles played by the microburst and the larger scale environment. Only an examination of the microburst domain

TABLE 6

Results of the u-momentum flux (u'w') budget calculation, averaged over the whole storm domain (15 x 15 km) for 1850 MDT. Units are in 10^{-3} m^2 s^{-3}.

Z (km)	Term A $\frac{\partial u'w'}{\partial t}$	Term B S	Term C T_r	Term D B	Term E P	Term F D_x	Term G D_y	Term H D_z
0.25	-1.70	0.05	0.03	23.92	-25.27	0.06	-0.06	-0.07
0.50	3.90	0.49	0.03	6.64	-3.60	0.36	-0.18	-0.12
0.75	1.78	0.96	-0.03	-17.01	18.06	0.48	-0.30	-0.09
1.00	-2.87	0.63	-0.15	-7.60	5.37	0.31	-0.17	0.08
1.25	-3.19	-5.07	-0.10	-3.39	6.28	-0.07	-0.02	0.09

TABLE 7

Results of the v-momentum flux (v'w') budget calculation, averaged over the whole storm domain (15 x 15 km) for 1850 MDT. Units are in 10^{-3} m^2 s^{-3}.

Z (km)	Term A $\frac{\partial v'w'}{\partial t}$	Term B S	Term C T_r	Term D B	Term E P	Term F D_x	Term G D_y	Term H D_z
0.25	-3.77	0.07	0.37	24.87	-29.23	-0.02	0.12	0.03
0.50	-0.11	0.89	0.34	20.96	-22.34	-0.06	-0.05	0.04
0.75	2.07	2.68	0.87	10.82	-11.39	0.01	-0.90	-0.03
1.00	12.54	4.40	2.05	5.60	2.96	0.23	-2.62	-0.08
1.25	4.30	7.50	1.35	8.84	-10.77	0.72	-3.30	-0.04

budgets may provide the answer.

The microburst domain budgets at 1850 MDT (Tables 8,9) reveal that the Dx and Dy term retain the same role played at 1845 MDT. Therefore, the growth and development of the microburst circulations may have been sufficient to dominate the larger scale flow. The transport term increased in importance at the microburst scale, although it is less important to the large scale. The intensification of the microbursts have increased the transport downward within the microburst domain; therefore, the likely cause of the weakening in the magnitude of the transport of momentum at large scales is due to feedback effects brought on by secondary circulations. As the microbursts intensify, the gust fronts and vertical motions between them intensify. This was discussed in the kinematic study as the intensification and creation of intense gust fronts, vertical rotors, and convergence lines brought on by the interactions between the microbursts. These secondary contributors counter the microburst at larger scales, by transporting some of the momentum brought down from aloft. I speculate that decay of the microburst/misocyclone circulation begins, when the counter processes cross the equilibrium point towards a positive flux of momentum upward.

In comparison to the 5 August 1982 case, the 1649 MDT, 14

TABLE 8

Results of the u-momentum flux (u'w') budget calculation, averaged over the reduced storm domain (4 x 4 km) for 1850 MDT. Units are in 10^{-3} m^2 s^{-3}.

Z (km)	Term A $\frac{\partial u'w'}{\partial t}$	Term B S	Term C T_r	Term D B	Term E P	Term F D_x	Term G D_y	Term H D_z
0.25	7.50	0.15	-3.90	-45.61	49.11	0.11	-0.18	0.03
0.50	-13.80	1.42	4.39	-17.77	-1.68	0.00	-0.10	-0.06
0.75	-12.93	2.51	-1.78	-2.19	-10.83	0.15	-0.61	-0.18
1.00	-10.69	1.38	-11.08	1.53	-2.67	0.69	-0.46	-0.09
1.25	-16.40	9.46	-6.92	-5.63	3.28	1.06	0.97	0.02

TABLE 9

Results of the v-momentum flux (v'w') budget calculation, averaged over the reduced storm domain (4 x 4 km) for 1850 MDT. Units are in 10^{-3} m^2 s^{-3}.

Z (km)	Term A $\frac{\partial v'w'}{\partial t}$	Term B S	Term C T_r	Term D B	Term E P	Term F D_x	Term G D_y	Term H D_z
0.25	-19.94	0.21	2.94	69.22	-91.31	-0.06	-0.61	-0.33
0.50	-6.07	2.60	-2.07	49.80	-54.26	0.15	-2.02	-0.28
0.75	4.78	7.04	-8.00	35.82	-28.44	0.54	-2.01	-0.16
1.00	8.04	9.70	-4.85	9.00	-6.05	0.92	-0.70	0.05
1.25	14.62	14.01	-0.38	2.50	-2.85	0.94	0.32	0.08

July 1982 case contains the following characteristics. Unlike the 5 August 1982 case, the balance of the momentum budget is more complicated. The balance at low levels is maintained by the transport, buoyancy, and pressure velocity terms. At mid levels the balance is maintained by the shear and buoyancy terms, while at upper levels the shear, transport and buoyancy terms dominate. These results are indicative of the differences in structure between the 5 August and the 14 July 1982 cases. The latter case has a low level jet at 3.5 km (Lin and Hughes, 1987), a downdraft 50% or greater in magnitude, and an updraft an order of magnitude larger than the 5 August 1982 case. The result is that the larger vertical motion and strong wind shear provided more momentum to drive the conversion of momentum from the mean to the eddy flow within the shear term. The shear term is a negative for the u-momentum case, and a positive for the v-momentum case. The eddies extract energy from the mean v-momentum and add it to the mean u-momentum. The transport is a maximum, because of the large value of downward vertical velocity and divergence in the microburst domain. A large positive magnitude at the low levels suggests that the momentum is accumulating below 0.50 km, while the large negative magnitude at the upper levels reveals that momentum is transported downward. The pressure velocity term is a minimum, because the updraft and downdraft in this case were of roughly the same magnitude,

and they tend to offset each other. This may suggest that this microburst is entering the later stages of its development, as the secondary circulations assume greater importance. The comparison has shown that microbursts contain unique dynamics that change from case to case. A study of many cases may be required to definitively identify and describe the complete structure and development of microbursts.

The research shows that the momentum budgets appear to be physically consistent with the kinematic analysis. There is some evidence to suggest that the mean flow is providing support to the eddy flow. By examining the eddy kinetic energy budget, the degree of the support and its physical mechanisms are the objects of interest.

6.5 The Eddy Kinetic Energy Budgets

The eddy kinetic energy budget will be examined to determine if the energy transformations agree with changes in the kinematic and momentum budget fields. The role of mean and eddy interactions can be studied, which will shed light on how scale interaction influences the microbursts. The energy budgets first examined will consist of the vertical flux of eddy kinetic energy, $w'E'$. This term is thought to be important in maintaining the microburst through transport of kinetic energy.

The total budget will be subsequently examined to determine the relative role of vertical transport to the entire budget. A further understanding of how the physical mechanisms represented within the budget interact to produce and maintain the microburst/misocyclone circulation is sought.

6.5.1 The Vertical Flux of the Eddy Kinetic Energy

The eddy kinetic energy is useful in identifying the turbulent kinematic features. The vertical flux of kinetic energy may provide information on how the turbulent kinematic features transport eddy kinetic energy to maintain the major features in the domain of interest. The following sections will examine the vertical flux divergence of eddy kinetic energy at 1845 and 1850 MDT, 5 August 1982, respectively.

6.5.1.1 The Vertical Flux of Eddy Kinetic Energy at 1845 MDT

The 1845 MDT case (Fig. 6.67) illustrates the importance of the gust front and the misocyclone circulation. The gust front features a maximum of eddy kinetic energy (E') both at the surface below the gust front, and extending upward from there. A smaller positive area to the left of M1 corresponds to the area of contact between M1 and M2. Although a gust front is

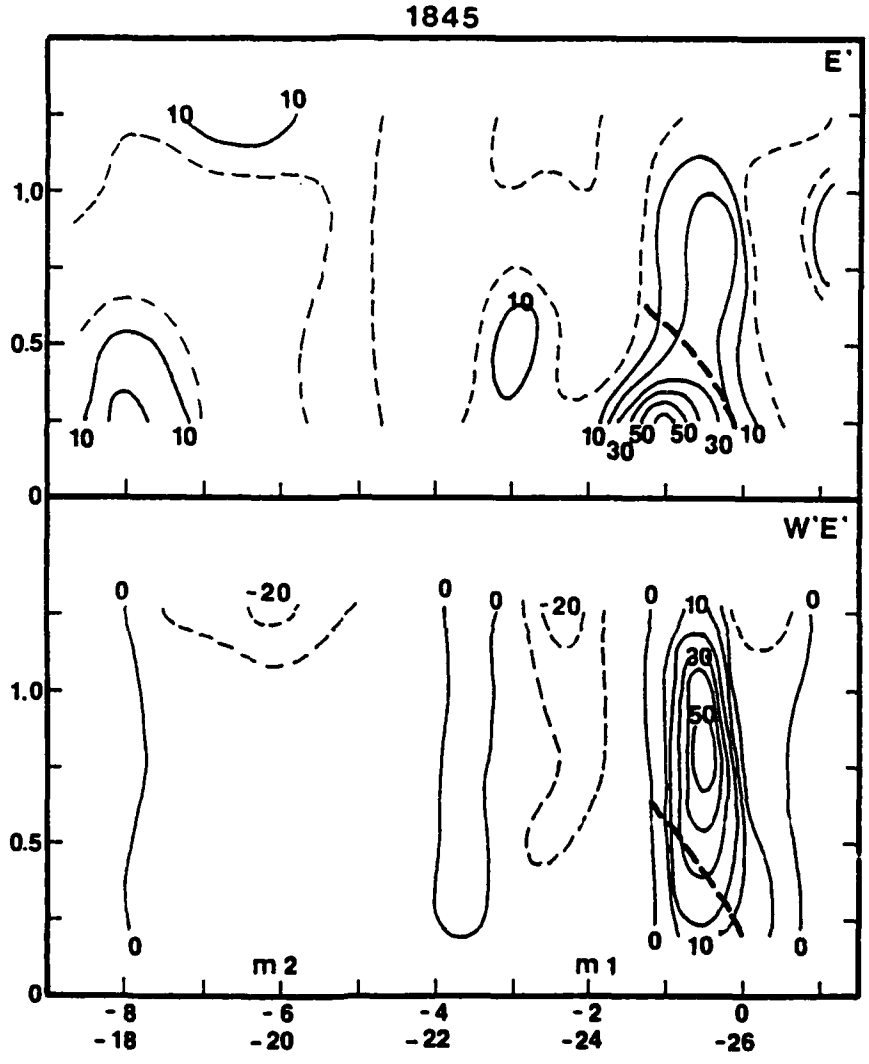

Fig. 6.67 NW-SE cross-section of the eddy kinetic energy and the vertical flux of eddy kinetic energy, for the 5 August 1982, 1845 MDT case.

not present, this feature suggests a separation of the microbursts. The vertical flux of eddy kinetic energy provides insight on how the eddy kinetic energy is circulated by the microbursts and the gust front. The vertical transport of eddy kinetic energy (W'E') plot clearly shows that the reservoir of eddy kinetic energy close to the surface, near the gust front, is transported upward by the updraft associated with the gust front. The flux upward of eddy kinetic energy contrasts with the large losses of eddy kinetic energy that are maximized at the M1 and M2 misocyclone circulations present at 1.25 km. The loss (downward transport) of eddy kinetic energy, associated with M1, extends to 0.5 km; whereas, M2 is largely above 1.0 km. This suggests that M1 has fully descended to the surface, while M2 has not. Both misocyclones are clearly responsible for transporting eddy kinetic energy toward the surface, where the maximum of eddy kinetic energy occurs. A narrow corridor of positive vertical flux between M1 and M2 clearly delineates the location of the boundary between M1 and M2. The evolution of the vertical flux and eddy kinetic energy may determine which systems are evolving the fastest.

6.5.1.2 The Vertical Flux of Eddy Kinetic Energy at 1850 MDT

The 1850 MDT case (Fig. 6.68) reveals that the maximum of

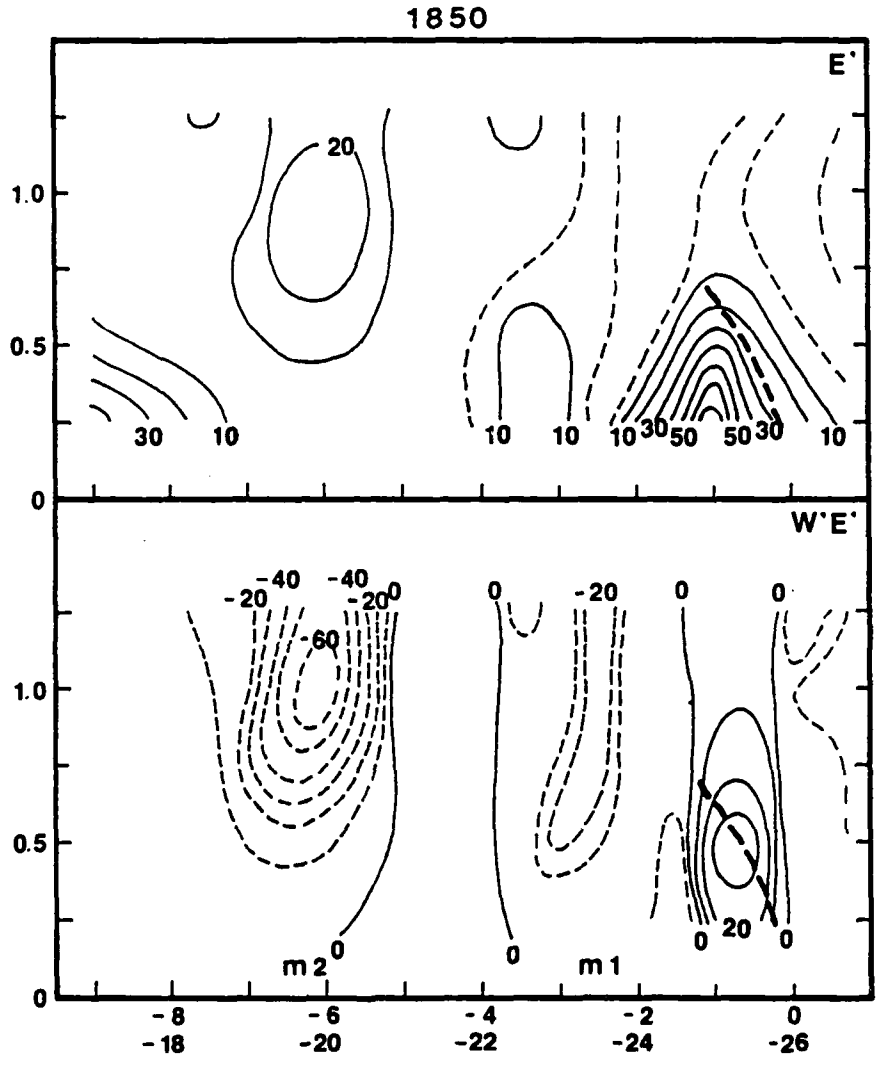

Fig. 6.68 Same as Fig. 6.67, except for 1850 MDT.

E', associated with the gust front, remains. The structure of the M1 microburst is perhaps slightly accentuated by an increase in the area coverage of the positive eddy kinetic energy. M2 by contrast reveals a lowering and intensification of the positive anomaly of eddy kinetic energy. The vertical flux of eddy kinetic energy shows that the growth of the positive anomaly in E' corresponds to the explosive growth of negative flux of E'. The kinematic analysis and momentum flux budgets examined previously suggested that M2 was intensifying more rapidly than M1. The vertical flux of E' has isolated the mechanism responsible for the rapid intensification of M2, the misocyclone. The rapid intensification of M2 and its lowering by vertical contraction, brought on by spin up causes a rapid increase of E' and a lowering of the feature. The intensified and organized misocyclone is able to efficiently draw in dry environmental air, which mixes with the high E' air within the misocyclone. The added negative buoyancy dramatically increases the downward motion with a dramatic increase in W'E'. The increased downward motion stretches the column and spins the misocyclone at a faster rate. Undoubtably, there is a strong feedback mechanism between the misocyclone's ability to entrain dry air and increase the downward motion, and the role that a stronger updraft has on spinning up and organizing the misocyclone. The M2 misocyclone was weak at 1845 MDT, so it is doubt-

ful that the misocyclone played a role in the initiation of the microburst, but it clearly plays a role in the intensification of M2. M1 does not intensify as rapidly as M2 does. Recall that the M1 misocyclone was well-developed at 1845 and 1850 MDT. The W'E' profile at 1850 MDT looks similar to the 1845 MDT profile. The 1850 MDT case reveals that the narrow shaft of downward flux of E' has intensified slightly. Other features include the increase of positive area in W'E' between M1 and M2. As M2 increases in intensity, it becomes better able to oppose the combined outflow of M1 and M2, since M2 becomes a greater obstacle in M1's outflow. Another interesting feature is the decrease in W'E' associated with the gust front. This may be a reflection of the weakening of that section of the gust front. The E' and W'E' profiles were useful in confirming previous speculation about intensification trends in the M1 and M2 microbursts. It also confirmed speculation about the role the misocyclone circulation plays in the intensification and maintenance of the microburst circulation. It does not identify specific physical processes that contribute to the growth of the microbursts. This missing key may confirm the role of dry entrainment in the misocyclone circulation. The missing key may be provided by examining the eddy kinetic energy budget for the 1845 and 1850 MDT time periods.

6.5.2 The Complete Eddy Kinetic Energy Budget

The eddy kinetic energy budget will be examined at the 1845 and 1850 MDT time periods and for the 1649 MDT case too. At 1850 MDT two cases will be considered. One case includes friction, and one case does not. The eddy kinetic energy budget will be further subdivided to include the budget for the entire grid, and a nested budget that includes only the microburst domain, as was done for the momentum budget studies. The eddy kinetic energy budget may provide information on the physical mechanisms responsible for the intensification of the microburst/misocyclone system.

6.5.2.1 The Eddy Kinetic Energy Budget at 1845 MDT

The 1845 MDT case (Table 10) reveals that the dominant terms in the budget are the HFD, VFD' and HFD' terms. The total buoyancy (BUP + PDG) is also a major term in the budget. The generation term (WPG) is significant at levels above 0.75 km, while frictional dissipation (FDI) is a major contributor at the lowest layer. The microburst/misocyclone can be shown as a mechanism for transferring energy from the turbulent state to the mean state for this particular microburst event. The intensification of the microburst might seem to predict a movement of energy from the mean to the eddy state, but recall that the

TABLE 10

Results of the eddy kinetic energy (E_t) budget calculation, averaged over the 10 by 10 km horizontal domain at 1845 MDT 5 August, 1982, which does not include tendency. Units are in 10^{-3} W m^{-3}. The definition of each term is given in the text.

Z(km)	HFD	VFD	WPG	HFD'	VFD'	FDI	WRS	BUP	PDG	LTE
0.25	2.41	0.34	-0.06	-0.42	-7.39	0.00	-2.61	0.12	0.46	-7.15
0.50	1.45	0.22	0.99	-1.39	-4.99	-0.09	-0.07	0.08	0.30	-3.50
0.75	2.43	0.10	0.24	-1.02	-2.21	-0.17	-0.11	-0.06	-0.62	-1.42
1.00	1.63	-0.02	-0.39	-0.59	1.73	-0.15	-0.38	0.76	-0.56	2.03
1.25	0.61	-0.14	-0.12	-1.68	5.21	-0.14	-0.79	-0.01	0.61	3.55

energy source is believed derived from the misocyclone level. The mean to eddy transformation (term WRS > 0) is more likely to occur with the misocyclone than with the surface layer microburst. At levels above 1.0 km, there is a increasingly positive gain in eddy kinetic energy through the VFD' term, as energy is extracted from the mean state via the misocyclone. A corresponding loss occurs in the VFD term, representing the mean flow. The mean kinetic energy is extracted from the high speed flow at upper levels by convergence and entrainment processes within the misocyclone. At lower levels the energy contained within the eddy flow descending within the microburst is converted back into the mean flow at low levels. Thus, the microburst tends to balance the difference in energy levels between the top and bottom of the misocyclone/microburst layer. As the storms intensify, the generation term serves as a sink, caused by an inability of the mass field to adjust to the wind field. The high speed air brought down from aloft enhances the flow from the low pressure at upper levels to the high pressure associated with the surface stagnation high. This process destroys kinetic energy. The total buoyancy term is dominated by the precipitation drag component. Precipitation loading is an important factor in the maintenance of the eddy kinetic energy budget, and in maintaining the strong downdraft. The friction term is important in the lowest layer, where it is a relatively

large sink of kinetic energy. It remains a sink above the lowest layer, although it is two orders of magnitude smaller. It increases at upper levels. This is associated with the turbulent eddy motion and shears associated with the misocyclone at those levels. This result is consistent with the observed maximum of the turbulent components of the momentum budget. The dominant mechanism present in the eddy kinetic energy budget is the flux divergence of kinetic energy from the mean to the eddy flow in the misocyclone, and from the eddy to the mean flow in the outflow surface layer of the microburst. The intensification of the misocyclone/microburst circulation at 1850 MDT will be examined to see if any changes occur in the eddy kinetic energy budget.

6.5.2.2 The Eddy Kinetic Energy Budget at 1350 MDT without Tendency

The 1850 MDT case (Table 11) is similar to the 1845 MDT case. The flux divergence is still the predominate mechanism with precipitation drag also important. Several important differences are noted. The first of these is the increase in the magnitude of the flux divergence terms and the generation term. The large value of kinetic energy destruction present at 1845 MDT is more pronounced at 1850 MDT. The lack of strong

TABLE 11

Results of the eddy kinetic energy (E_t) budget calculation, averaged over the 10 by 10 km horizontal domain at 1850 MDT 5 August, 1982, which does not include tendency. Units are in 10^{-3} W m^{-3}. The definition of each term is given in the text.

Z(km)	HFD	VFD	WPG	HFD'	VFD'	FDI	WRS	BUP	PDG	LTE
0.25	4.63	0.63	0.21	-17.66	-0.38	-2.75	0.05	0.35	0.87	-14.05
0.50	3.32	0.40	-1.96	-8.44	0.22	-0.51	0.13	1.97	2.41	-2.46
0.75	2.32	0.13	-3.13	-3.68	1.00	-0.03	0.40	1.30	2.87	1.18
1.00	1.15	0.11	-0.91	-1.30	0.78	-0.33	0.36	-0.66	3.27	2.47
1.25	0.56	0.13	-0.95	0.92	0.38	-0.52	-0.53	-5.46	3.62	-1.85

horizontal pressure patterns and associated eddy circulations at 0.75 km results in a dominance of the generation term by vertical interaction of the wind field with the pressure field. Downward flow toward high pressure at 0.75 km will thus produce a destruction of energy. Enhanced downward flow also appears to increase the magnitude of the precipitation drag term. Enhanced downward motion with a large value of precipitation drag serves to enhance the spin up of the misocyclone through vertical vorticity stretching. It also suggest a lowering of the reflectivity cores within the microbursts. The spin up and compression of the circulation allows VFD' to achieve a positive value even at 0.50 km. The horizontal flux divergence of eddy kinetic energy achieves a large value of dissipation at levels below 0.75 km. The increased outflow associated with the intensified microburst is reflected in the large value of the horizontal flux divergence of eddy kinetic energy. A large increase in negative buoyancy at 1.25 km reflects the rapid intensification of the M2 misocyclone. The M2 misocyclone is warm-cored at 1.25 km, since the mixing of dry air by misocyclone entrainment is not yet sufficient to create a cold core downdraft. The sinking of warm air creates a negative value of buoyancy. The dominant physical mechanism associated with the microburst is the extraction of mean energy by the misocyclone and transporting it downward to the microburst level. The microburst transfers

eddy kinetic energy back to the mean flow. It appears that the larger the loss of mean flow at the misocyclone level, the greater the intensification of the entire circulation. At 1850 MDT the conversions of kinetic energy are not as large. Perhaps the greatest intensification of the system has occurred between 1845 and 1850 MDT. An examination of a separate case with tendency included in the perturbation pressure calculation is included for rough comparison purposes only.

6.5.2.3 The Eddy Kinetic Energy Budget at 1850 MDT with Tendency

The inclusion of tendency has produced profound changes in the BUP and WPG terms of the equation (Table 12). The generation term retained the sign of the previously calculated WPG term for the non-tendency case. The magnitude of the term has increased by a factor of three to five. The buoyancy term changed sign to a positive value and increased in magnitude by a factor of three to five. The result suggests, for a rapidly evolving complex microburst event, the pressure calculation must include the tendency term. The inclusion of tendency will affect pressure gradients, which in turn affects those terms of the equation that are a function of the pressure gradient. The exact nature of the difference and its physical significance

TABLE 12

Results of the eddy kinetic energy (E_t) budget calculation, averaged over the 10 by 10 km horizontal domain at 1850 MDT 5 August, 1982, which includes tendency. Units are in 10^{-3} W m^{-3}. The definition of each term is given in the text.

Z(km)	HFD	VFD	WPG	HFD'	VFD'	FDI	WRS	BUP	PDG	LTE
0.25	4.63	0.63	-0.34	-17.66	-0.38	-2.75	0.05	2.22	0.87	-12.73
0.50	3.32	0.40	-3.03	-8.44	0.22	-0.51	0.13	6.97	2.41	1.47
0.75	2.32	0.13	-8.23	-3.68	1.00	-0.03	0.40	9.78	2.87	4.56
1.00	1.15	0.11	-5.41	-1.30	0.78	-0.33	0.36	8.71	3.27	7.34
1.25	0.56	0.13	-3.90	0.92	0.38	-0.52	-0.53	2.31	3.62	2.97

will not be examined in this study. This type of work should be accomplished for a case that contains three or more time periods at two minute intervals to maximize temporal resolution.

6.5.2.4 The Eddy Kinetic Energy Budget at 1649 MDT

The final case examined will be the eddy kinetic energy budget for the simple case microburst. The table is not shown because of the relative simplicity of the result. The domain considered is the microburst domain (4 X 4 km). The balance is almost exclusively between the flux divergence terms and the buoyancy term. The most interesting difference is that the simple case shows a conversion of mean to eddy flow at all levels and of a similar magnitude. It also shows a gain of eddy kinetic energy at the lowest levels with a deficit at levels above 1.0 km, which is a similar pattern to the complex case. A common characteristic of these two very different microburst is the role that eddy kinetic energy flux divergence plays.

The vertical flux profiles of eddy kinetic energy and the eddy kinetic energy budgets for 1845 and 1850 MDT, 5 August 1982 have identified the misocyclone as the structural mechanism responsible for the intensification of the M2 microburst. The eddy kinetic energy budget confirmed the key role played by

the misocyclone in the microburst intensification by extracting energy from the mean flow and transporting it downward through the downdraft to low levels, where the horizontal outflow converts the eddy kinetic energy transported downward from aloft, to the low level mean flow. The results of the kinematic analysis, the momentum budgets, and the eddy kinetic energy budgets may be integrated with results of previous research to provide a comprehensive conceptual model of the mechanisms and interactions that have occurred within the complex and simple microburst domains.

7. Hypothesized Conceptual Model of a Microburst

The results of the previous sections are combined to produce a conceptual model of how these microbursts may have been formed and are maintained.

The simple case is characterized by a microburst embedded within a descending reflectivity core ($Z < 55$ dBz). The downward vertical motion associated with the microburst was greater than 5 m/s. A bow echo circulation was present in this case with the microburst descending from near the rotating head. The momentum budgets and eddy kinetic energy budgets revealed the importance of the downward transport of high-momentum air. This result confirmed that downward transport was occurring within the subcloud layer. A similar result was also noted by Lin and Condray (1988) for the 1647 MDT case, which preceded the simple case. They also noted the presence of a 3.5 km jet. The strong wind shear near the 3.5 km jet ensures that a very turbulent environment prevails with eddy motion interacting with the downdrafts to produce downward transport of high-momentum air, probably due to the tilted nature of the updrafts and downdrafts. The dry high-momentum air enters the bow echo from the rear, where it encounters the concave back edge of the bow echo. Mixing ensues, which creates precipitation-cooled air

that transports the air further downward. The stronger environmental wind present assures that the environmental scale will dominate the meso γ-scale of the microburst. No well-organized misocyclone is present, because of the dominance of the larger scale winds and the lack of directional shear in the environmental winds. Srivastava (1987) has shown that microbursts may be initiated and maintained by dry entrainment processes. The key to this type of microburst seems to be the flux rate of high-momentum, dry, environmental air across the concave back edge of the bow echo. The greater the flux, the greater the mixing rate, which increases the downward transport of air. The rapidly descending air is compressionally warmed to create a warm core microburst, because of vertical motion in excess of 5 m/s. This is a sufficiently rapid descent to not allow the saturated downdraft to mix with the environmental air. The air descends nearly dry adiabatically instead of moist adiabatically. These results were produced or observed in a simple one-dimensional model, Srivastava (1985,1987); PAM station observations Fujita (1985); and in a study using dual-Doppler data, Lin and Hughes (1987). The microburst centers were found to be centers of high perturbation pressure. The simple case is simple in part, because the larger scale flow can dominate the small scale flow; therefore, eddy motions of misocyclone circulations are suppressed or are of secondary importance, the

microburst is isolated with interactions limited to the outer edges of the microburst, and these types of storms can be predicted by techniques based on the presence of mid-level moisture and a deep, dry, well-mixed layer, in the manner of Caracena et al. (1983). Of primary interest is what are the driving forces behind the complex case of a multiple microburst case that occurs in a microburst-producing storm not predicted by present forecasting techniques.

The complex case is characterized by several microbursts, within a small domain. These storms interact with each other to produce gust fronts, and rotor circulations, and they distort each other's outflow patterns. There are similarities with the simple case. The bow echoes do develop after the onset of the surface microburst. These bow echoes are aligned perpendicular to the mean, environmental, high-momentum air, associated with a low level wind maximum. The microbursts are coincident with the high reflectivity cores. Inflow into the bow echo, at levels above 1 km, is mixed with the saturated downdraft. Subsequently, the high-momentum wind is collected above 1 km, then carried down to the surface layer of the microburst. The role of transport and buoyancy processes seems common to both types of microbursts. The microburst in a general conceptual model may be thought of as a mechanism for transporting mass, energy, and momentum, between the boundary layer ($z < 1$ km) and the

subcloud/parent storm, which occurs above 1 km (AGL). A microburst is simply a meso -scale, organized, turbulent eddy. The structural features responsible for the microburst development, and the physical processes that maintain them are not unique.

The structural features for the complex case feature a turbulent upper layer above 1 km, dominated by a misocyclone circulation, a weakly divergent, weakly eddying, mid-level at 0.75 km that was dominated by the mean flow, and a very turbulent surface layer below 0.75 km, which was dominated by the microbursts and their secondary circulations. Of particular interest is the structure and development of the misocyclone at upper levels, and the microburst circulation at low levels.

The structure of the storm can be understood by examining how the microburst may have developed. The complex case is not conducive to forecasting, using techniques based on negative buoyancy from a deep, dry, mixed layer (Caracena et al. (1983)). Dry entrainment and evaporative cooling are not sufficient to initiate the microbursts for this type of storm. Precipitation loading is not the likely cause, because tropical and subtropical convection features heavy rains with comparatively mild horizontal surface winds. Hail has been noted within the core of microbursts, even within thunderstorms occurring in the moist gulf coast region. Wakimoto (1988) used

dual-polarization data from the CP-2 radar to locate a 65 dBz hail shaft within the microburst core. He suggested that the presence of a hail shaft may be indicative of the presence of a microburst. A study of a Colorado supercell using the CP-3 and CP-4 radars was conducted by Miller et al. (1988). The results indicated that the location of hail reports were mostly inside the swath of the 55 dBz contour. The hail sizes noted were 2-3 cm in diameter with a maximum reflectivity of 65-75 dBz. Using modeled data, Foote (1984) showed that hailstones of 1.0 cm in diameter lose 73% of their mass during descent through warm air. Many researchers, including Hjelmfelt (1984) and Parsons et al. (1985) have noted that cyclonic circulations aloft are associated with appendages of very high reflectivity. Parsons et al. (1885) indicated that for a 30 June 1982, JAWS case, the microburst downdraft initially formed close to a small core of reflectivity embedded within a larger 'arm' of reflectivity. An intense cyclonic circulation centered about a reflectivity appendage, with continuity to heights above cloud base, was noted by Hjelmfelt (1984). He also noted that peak surface reflectivities were attained prior to the maximum microburst divergence intensity. Also, evidence of low relectivity notches in the neighborhood of the microburst downdrafts suggested that melting provides an additional source of energy. From a three-dimensional model, Proctor (1988) showed that a warm core may

be present. Hail is too small to compensate for compressional heating, unless the vertical velocity of the downdraft is very small. Since hail plays a relatively minor role in maintaining the microburst, its role may be in a different capacity. The main problem in distilling the answer from the evidence is to determine if the presence of the microburst is the result of the hail or the hail is the result of the presence of a microburst. Hail falling in strong downdrafts has a significant advantage over hail that does not, in that it can spend considerably less time in the warm air before reaching the ground. A comparison of the 1649 MDT, 14 July 1982 and the 1845 and 1850 MDT, 5 August 1982 cases shows that the cloud base is higher for the former case. The lower reflectivities encountered in the simple case suggests that the hail was incidental to the microburst. However, the complex case occurred in an environment of higher available latent heat for melting. Also, the downward motion within the microburst was one-half of the magnitude experienced in the simple case. This suggests that hail may be responsible in part, for the microburst, since a larger volume of hail is necessary to maintain the high reflectivity values in the complex case, where the melting rate is higher, due to a slower descent of the hail in the microburst downdraft, relative to the simple case, and the greater availability of environmental latent heat. If there was another causal

mechanism present, the reflectivity core should have been lower or the same as the simple case. I believe that a main causal mechanism for the complex case microburst was hail melt processes, but dry entrainment processes associated with the misocyclone circulation and downward momentum transport of energy extracted from the mean state to the eddy state maintained the microburst at lower levels. New forecasting techniques, to consider the role played by hail, are necessary to forecast microbursts for relatively moist soundings. By examining the conceptual model in a temporal sense, the microburst synthesis is clearer.

It is postulated that the evaporative cooling from precipitation initiates the downdraft, see Srivastava (1985), but the focus for the microburst is provided by the descending hail shaft. The hail melt contributes the necessary additional negative buoyancy, when combined with evaporative cooling, to create a sufficient downward flux of mass and momentum to produce the microburst. The hail melts below the freezing level, with the maximum contribution of hail melt to negative buoyancy occurring at the bottom of the descending microburst. At that level, the melting is maximized, as the cool microburst air mixes with the warm subcloud layer. A commonly observed event with microbursts is a descending reflectivity core, accompanied by a 'melting level depression'. The contribution from hail

melt to the microburst diminishes, once the microburst impinges upon the surface. The air through the subcloud layer has been cooled; therefore, melting slows down with time. This is confirmed by the descending reflectivity core and the melting level depression. As the hail shaft becomes more insulated, the hail melt contribution to negative buoyancy is limited to the outer edge of the reflectivity core. Since hail melt no longer becomes a major factor in the microburst's development, some other mechanism must be evolving to take its place.

The misocyclone is not present during the early stages, as confirmed by M3 in the 5 August 1982 case. As the downdraft and microburst progress downward toward the surface, the atmospheric column, through which the downdraft descends, becomes stretched. The stretching occurs in a light wind environment of environmental winds less than 10 m/s, but with strong directional shear of the winds backing with height. Since the meso γ-scale dominates the meso -scale winds, the stretching of the vorticity initiates a cyclonic gyre above 0.75 km. The gyre entrains dry, high-momentum, environmental air into the downdraft, where it mixes with the cool saturated downdraft. The enhanced dry entrainment with evaporative cooling, downward flux of momentum, and enhanced precipitation drag due to the precipitation core, become the primary maintainers of the microburst. The weak reflectivity notches, noted in this

study, are a manifestation of this process. The evolution of the bow echo parallels the development of the misocyclone. In this study the rotating head of the bow echo (Fujita (1985)) was coincident with the steady state of the 1649 MDT case, and M1 of the 5 August 1982 case.

The surface microburst is a direct result of the downdraft impinging upon a horizontal surface. The stretched downdraft, becomes compressed as its downward velocity is slowed from contact with the ground. The compression results in a spin down of the downdraft. The cyclonic circulation undergoes spin down to a neutral condition at 0.75 km. Below that level, a rapid spin down creates a highly divergent circulation. The microburst sets up secondary circulations on its margins. A cat's eye roll vortex forms on the outer edge of the microburst, when the horizontal shear between the microburst outflow opposes each other. The higher density flow will determine the sense of rotation. Interieri et al. (1988) used Doppler lidars to show that uneven flows produce gyres and cat's eye circulations. In addition the gust front and environmental flow combine to create an updraft that stretches the surface vorticity to create a spinning updraft. At misocyclone level, the misocyclone and mesocyclone-like circulation interact. The mesocyclone-like circulation facilitates the entrainment of environmental air into the misocyclone, thus becoming a

feedback mechanism within the misocyclone/microburst circulation.

Finally, a summary of the main points of the conceptual model and the microburst structure are presented as follows: lmicroburst structure are presented as follows: 1) Fujita's (1985) criteria of the microburst are to be updated. The new criteria should include the downward vertical velocity, reflectivity, and the maximum horizontal wind shear; 2) the role of the misocyclone circulation, occurring above 0.70 km, is to be investigated; 3) the role of a circulation occurring where the environmental wind and the gust front wind shear are a maximum, should be further researched. As other microbursts affect the interaction between storm and environment, the position of the mesocyclone-like cyclonic circulation shifts to the new area of highest shear. 4) The mesocylone-like circulation interacts with the misocyclone to feed dry environmental air into the misocyclone. 5) The microburst occurs before the creation of the misocyclone and the bow echo. The misocyclone and the bow echo intensify in unison. The rotation head of the echo is coincident with the misocyclone. 6) The misocyclone assists in entraining and mixing the dry environmental air with the saturated downdraft. 7) The inflow into the downdraft/bow echo occurs at the concave back edge. This edge is aligned perpendicular to the environmental flow. 8) The downdraft, for the

wet Colorado microburst, appears to originate from a reflectivity core of at least 45 dBz. 9) The momentum flux and eddy kinetic energy flux were downward within the microburst. This indicates a net transport of mass and momentum to the surface from aloft. 10) Frictional parameterization and the inclusion of the local tendency term improves the momentum check (Table 13). 11) The microburst center is an area of high perturbation pressure, with an area of relative low pressure surrounding the microburst. 12) Roll vortices occur at the microburst's edge. A maximum of vortice generation occurs between colliding outflows from separate microbursts, with a secondary maximum where the environmental wind and the microburst outflow intersect at a wind discontinuity of 180 deg.. 13) For downward motion of less than 3-4 m/s, a cold core microburst results. If the downdraft is of a greater magnitude, a warm core will result.

The conceptual model, derived from this study, is based on a composite of the present research and findings from previous work. Additional work is required to confirm or modify this model, and to answer questions implied by the present research but not answered.

TABLE 13

Results of the momentum check comparison of the perturbation pressure outputs. The domain is (14 x 14 km) for 1850 MDT, 5 August 1982. The values are non-dimensional.

Z (km)	Without Tendency Without Friction	Without Tendency With Friction	With Tendency With Friction
0.25	.2548	.2520	.2320
0.50	.3702	.3605	.3238
0.75	.3638	.3661	.3588
1.00	.3462	.3417	.3479
1.25	.3889	.3689	.3628
Avg.	.3448	.3378	.3251

8. Suggested Topics for Future Research

Much work needs to be conducted to verify or modify these results. The following is a list of possible topics for future study: 1) A trajectory study using data from this case and similar cases. 2) A study of pressure retrieval using a microphysical parameterization of hail melt should be conducted to determine if it may or may not have a significant impact on the perturbation pressure recovery and the perturbation temperature recovery. 3) A study using dual-Doppler data could be conducted, using a two minute interval, centered difference, velocity tendency term for calculating the perturbation pressure. 4) A numerical model should be used to confirm or modify the conceptual model. 5) A study using a 0.25 km grid spacing should be conducted to examine the impact of the inherent smoothing of the Barnes's (1973) scheme on the small scale features. 6) A study using a 0.125 km grid level (AGL) may show more detailed structure of the storm at the lowest level, and a more accurate result from the upward integration of the anelastic continuity equation. 7) Several data sets from different geographical regions should be used to conduct similar studies. 8) A study on how sensitive the individual components of the budget equations are to random errors should be conducted. 9) Additional work on the 5 August 1982 case should

include the 1847 MDT time period to allow the researcher more insight into the microburst's evolution. 10) A vorticity budget should be conducted to see how stretching of the vorticity influences the growth and decay of the misocyclone and the microburst.11) A forecasting limiting index to indicate if hail is necessary to generate a microburst, and to what degree would that be indicated by examining the reflectivity return, should be developed. 12) A correlation study between observed reflectivity values, the wet bulb of the subcloud layer, and the microburst intensity should be conducted, as a method for forecasting the severity of microburst events.

Appendix A: Frictional Parameterization

Friction nay be conceptually thought of as cellular mixing circulations that efficiently transmit energy between areas of deficit and surplus, principally down-gradient. Except at the microscale, below several millimeters, where molecular dissipation is significant, mesoscale and synoptic scales are dominated by eddy transport of momentum, heat and moisture. Since eddy circulations are two-dimensional eddies, the degree of correlation between the magnitudes of perturbations of the three-dimensional components of the mean wind indicates the strength and efficiency of the frictional eddies. The eddy strength is stated symbolically and may be calculated directly, if data response time is sufficiently rapid, as:

$$\tau_{ij}^{*} = -\bar{\rho}\,\overline{u_i' u_j'} \qquad \text{Eq. (1)}$$

where $\bar{\rho}$ is the mean air density, and i and j vary from 1 to 3. This method produces a qualitative field of eddy stresses, which describes the momentum flux exchange conducted by the eddies, but are sensitive to error for quantitative calculations.

The quantitative method used to calculate the τ_{ij} and Km values for the eddy momentum and kinetic energy budget begins

with the Reynold's equations of motion in tensor form:

$$\frac{\partial \bar{\rho}\bar{u}_i}{\partial t} + \frac{\partial}{\partial x_j}(\bar{\rho}\bar{u}_i\bar{u}_j) + \frac{\partial}{\partial x_i}(\bar{\rho}\overline{u_i'u_j'}) + 2\varepsilon_{ijk}f_k\bar{\rho}\bar{u}_j = -\bar{\rho}\frac{\partial \bar{\Phi}}{\partial x_i} + \frac{\partial}{\partial x_j}(\bar{\tau}_{ij}) \quad \text{Eq. (2)}$$

where the overbar represents the mean of the quantity, the prime represents an anomaly, eddy motion, ε_{ijk} is a unit tensor. τ_{ij} is the molecular stress tensor and other variables are by standard convention. Substituting Eq. (1) into Eq. (2) results in

$$\underbrace{\frac{\partial \bar{\rho}\bar{u}_i}{\partial t}}_{A} = \underbrace{-\frac{\partial}{\partial x_i}(\bar{\rho}\bar{u}_i\bar{u}_j)}_{B} - \underbrace{2\varepsilon_{ijk}f_h\bar{\rho}\bar{u}_j}_{C} - \underbrace{\bar{\rho}\frac{\partial \bar{\Phi}}{\partial x_i}}_{D} + \frac{\partial}{\partial x_i}\left(\bar{\tau}_{ij} + \overline{\tau}_{ij}\right) \quad \text{Eq. (3)}$$

where Term A = local time rate of change in mean momentum, per unit volume, Term B = flux convergence/divergence of momentum by mean motion, Term C = Coriolis force, per unit volume, Term D = geopotential gradient force, per unit volume, and Term E = flux convergence/divergence of momentum by eddy and molecular motion.

The pressure gradient force is contained within term E due to the molecular stress (τ_{ij}). Klemp and Wilhelmson (1978) parameterized the eddy stress gradient of the subgrid turbulent momentum terms, $\underset{\sim}{f}_i$, as:

$$\underset{\sim}{f}_i = \frac{\partial}{\partial x_j}(\tilde{\tau}_{ij}^{*}) = -\frac{\partial}{\partial x_j}(\bar{\rho}\overline{u_i'u_j'}) \quad \text{Eq. (4)}$$

The local momentum flux may be defined as the loss of momentum to other scales of motion from the total subgrid-scale

eddy kinetic energy as follows:

$$\overline{u_i' u_j'} = -K_M \left(\frac{\partial \bar{u}_i}{\partial x_j} + \frac{\partial \bar{u}_j}{\partial x_i} \right) + \frac{2}{3} \delta_{ij} E \qquad \text{Eq. (5)}$$

where Km is the eddy momentum transfer coefficient, δ_{ij} is the Kronecker constant, and E is the subgrid-scale eddy kinetic energy, per unit mass, symbolically stated as:

$$E = \frac{1}{2} (\overline{u_i'^2}) \qquad \text{Eq. (6)}$$

Ideally one would like to be able to calculate friction directly with fast response sensors (Doppler radar is not). Doppler radar data are actually sample volumes, not points, which are linearly, temporally interpolated. Since this isn't conducive to direct calculation of turbulance at the subgrid scale and the energy, E, contained within the eddies, the following technique is used.

To solve this problem, parameterization is used. From Smagorinsky (1963) we get a form of Km originally used to calculate Km at a larger scale of motion from the deformation tensor. Deardorff (1972) proposed that for unstable environments, the subgrid-scale eddy coefficient, c, is 0.21. The value, c, is an efficiency type quantity that parameterizes the energy cascade to lower scales. The result is as follows:

$$K_M = \frac{c^2 \ell^2}{\sqrt{2}} \left| \frac{\partial u_i}{\partial x_j} + \frac{\partial u_j}{\partial x_i} \right| \qquad \text{Eq. (7)}$$

Knowing Km one can obtain E by dimensional grounds as pro-

and

$$(K_m)_{zz} = \frac{c^2 \ell^2}{\sqrt{2}} \left| 2 \frac{\partial w}{\partial z} \right| \qquad \text{Eq. (13)}$$

The Reynold's stresses may be expanded in similar fashion:

$$\tau^*_{xx} = \bar{\rho}\left\{(K_m)_{xx}\left(2\frac{\partial u}{\partial x}\right) - \frac{2}{3}\frac{(K_m)^2_{xx}}{c^2 m \ell^2}\right\} = \bar{\rho}\left\{\frac{c^2\ell^2}{\sqrt{2}}\left|2\frac{\partial u}{\partial x}\right|\left(2\frac{\partial u}{\partial x}\right) - \frac{1}{3}\frac{c^4\ell^2}{c_m^2}\left|2\frac{\partial u}{\partial x}\right|^2\right\},$$

$$\tau^*_{xy} = \tau^*_{yx} = \bar{\rho}\left\{(K_m)_{xy}\left(\frac{\partial u}{\partial y} + \frac{\partial v}{\partial x}\right) - \frac{2}{3}\cancel{\delta_{12}}^{0} E\right\} = \bar{\rho}\left\{\frac{c^2\ell^2}{\sqrt{2}}\left|\frac{\partial u}{\partial x} + \frac{\partial v}{\partial y}\right|\left(\frac{\partial u}{\partial x} + \frac{\partial v}{\partial y}\right)\right\},$$

$$\tau^*_{xz} = \tau^*_{zx} = \bar{\rho}\left\{(K_m)_{xz}\left(\frac{\partial u}{\partial z} + \frac{\partial w}{\partial x}\right) - \frac{2}{3}\delta_{13} E\right\} = \bar{\rho}\left\{\frac{c^2\ell^2}{\sqrt{2}}\left|\frac{\partial u}{\partial z} + \frac{\partial w}{\partial x}\right|\left(\frac{\partial u}{\partial z} + \frac{\partial w}{\partial x}\right)\right\},$$

$$\tau^*_{yy} = \bar{\rho}\left\{(K_m)_{yy}\left(2\frac{\partial v}{\partial y}\right) - \frac{2}{3}\frac{(K_m^2)_{yy}}{c_m^2 \ell^2}\right\} = \bar{\rho}\left\{\frac{c^2\ell^2}{\sqrt{2}}\left|\frac{\partial v}{\partial z} + \frac{\partial w}{\partial x}\right|\left(\frac{\partial v}{\partial z} + \frac{\partial w}{\partial x}\right)\right\},$$

$$\tau^*_{yz} = \tau^*_{zy} = \bar{\rho}\left\{(K_m)_{yz}\left(\frac{\partial v}{\partial z} + \frac{\partial w}{\partial y}\right) - \frac{2}{3}\delta_{23} E\right\} \qquad \text{Eq. (14)}$$

$$= \bar{\rho}\left\{\frac{c^2\ell^2}{\sqrt{2}}\left|\frac{\partial v}{\partial z} + \frac{\partial w}{\partial y}\right|\left(\frac{\partial v}{\partial z} + \frac{\partial w}{\partial y}\right)\right.$$

$$\tau^*_{zz} = \bar{\rho}\left\{(K_m)_{zz}\left(2\frac{\partial u}{\partial z}\right) - \frac{2}{3}\frac{(K_m)^2_{zz}}{c_m^2 \ell^2}\right\} = \bar{\rho}\left\{\frac{c^2\ell^2}{\sqrt{2}}\left|2\frac{\partial w}{\partial z}\right|\left(2\frac{\partial w}{\partial z}\right) - \frac{1}{3}\frac{c^4\ell^2}{c_m^2}\left|2\frac{\partial w}{\partial z}\right|^2\right\}$$

The Reynold's stresses were calculated from Eq. (15) and were utilized in the pressure calculation and the turbulent kinetic energy budget.

Appendix B: Additional Error Analysis

The following scale analysis was calculated to show the impact of possible error and uncertainty of hail on the three-dimensional wind field. This process is important not only to determine the validity and relevance of the derived fields, but also to demonstrate their sensitivity to error.

The first possible source of error that will be examined is the impact of hail and attendant reflectivity uncertainty on the computation of the three-dimensional wind field, Armijo (1969). The complete set of equations was derived in Section 3.

Assume a point very close to both radars with hail occurring with a terminal fall speed of 20 m/s. In a shallow volume such as the one used in this study, the elevation angle was never more than 10^{o} and the closest point to a radar was 6.5 km. The highest level analyzed was 1.25 km for this case, the 5 August 1982 case, see Fig. (B1). The result from calculation.

$$\tan = y/x = \tan 10 \text{ deg.} = y/20 \text{ m/s}$$

$$y \sim 3.5 \text{ m/s}$$

This condition requires the entire pulse volume to behave as one hailstone. Realistically, a size distribution for hail, given by Auer (1972), gives a more physically meaningful result

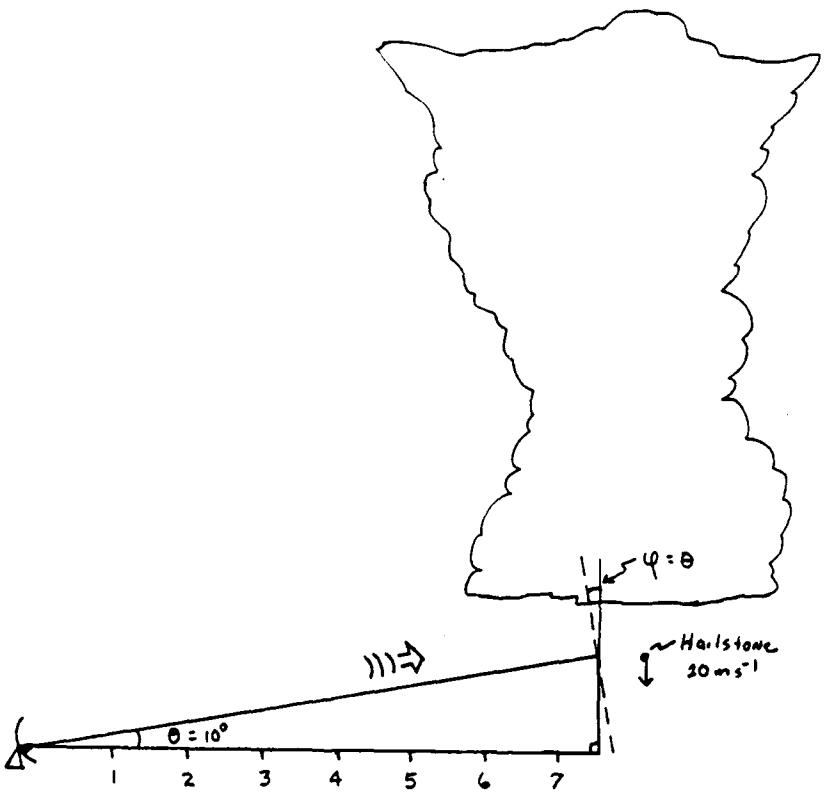

Fig. B1 Maximum effect of hail on radial velocity.

by specifying the amount of hailstones per volume of air.

$$N(d) = 561.3d^{-3.4}$$

Where N (mm^{-3}) and d (mm) for $1 < d < 50$ mm. A stone of 20 m/s fall speed would correspond to a stone at the upper end of the d (mm) scale. As the relationship suggests, the greater the individual hail size, the greater the possible contribution to the radial velocity, but the less the actual number of such hail per pulse volume. The result would suggest that for a volume of $7.07 \times 10^{6}\ m^{-3}$, the ensemble contribution would be negligible in the boundary layer unless an intense hailstorm is present.

Of greater importance is the impact of hail on the terminal fall speed via the precipitation-drag term. The relationship chosen was the Martner (1975) parameterization. It is weakly dependent on reflectivity. By introducing a 20% error, which seems to be an upper limit according to Spahn and Smith (1976), results as follows:

$$\text{Error } V \ (20\%) \sim .5 \text{ m/s}$$

The observed reflectivity was chosen to be 56 dBz with an actual value of 70 dBz.

A second source of error considered here is the impact error in terminal fall speed may have on the horizontal wind components. Again, an extreme example is used. If one radar is 6.5 km from the datum, the other is approximately 15 km away, see Fig. (3.1). The radial winds are an average of 8 m/s. Although both radars will not likely see the same magnitude of radial velocity or even the same sign due to geometric considerations, they will for purposes of illustration. Plugging back into one of the Armijo (1969) equations and using the same input parameters results in:

$$u = \left[\frac{(6.5\times10^{3}\,m)(8\,ms^{-1})y_1 - (15\times10^{3}\,m)(8\,ms^{-1})y_2}{(x_2y_1 - x_1y_2)}\right] -$$

$$\left[\frac{(y-y_2)(0+6.7\,ms^{-1})(1.25\times10^{3}\,m)}{(x_2y_1 - x_1y_2)}\right], \text{ or substituting:}$$

$$u = \frac{(52\times10^{3}\,m^2s^{-1})y_1 - (120\times10^{3}\,m^2s^{-1})y_2 - (y_1-y_2)8.38\times10^{3}\,m^2s^{-1}}{(x_2y_1 - x_1y_2)}$$

It is obvious from this illustration that the precipitation drag term will introduce a less than 10% error into the calculation even when assuming the presence of hail and a maximum error in the reflectivity. Also, the Barnes (1973) routine will smooth out any areas of maximum error so the singular, exceptionally large values of error are minimized.

The same procedure with more typical values (reflectivity

REFERENCES

Armijo, L., 1969: A Theory for the Determination of Wind and Precipitation Velocities with dual-Doppler Radars. J. Atmos. Sci., 26, 566-569.

Auer, August H., Jr., 1972: Distibution of Graupel and Hail with Size. Mon. Weath. Rev., 100, 325-328.

Barnes, S., 1973: Mesoscale Objective Analysis Using weighted time series observations. NOAA Tech. Memo ERL NSSL-62, 60 pp.

Bohne, A. R., and R. C. Srivastava, 1976: Random Errors in Wind and Precipitation Fall Speed Measurement by a Triple Doppler Radar System. Preprints, 17th Conf. on Radar Meteor., Seattle, Amer. Meteor. Soc., 7-14.

Brandes, E. A., 1977: Gust Front Evolution and Tornado Genesis as Revealed by Doppler Radar. J. Appl. Meteor., 16, 333-338.

_____,1978: Mesoscale Evolution and Tornado Genesis: Some observations. Mon. Wea. Rev., 106, 995-1011.

_____,1984: Relationship Between Radar Derived Thermodynamic Variables and Tornadogenesis. Mon. Wea. Rev., 112, 1033-1052.

Caracena, F., J. McCarthy, and J. Flueck, 1983: Forecasting the Likelihood of Microbursts along the Front Range of Colorado. Preprints, 13th Conf. on Severe Local Strms, Tulsa, Amer. Meteor. Soc., 261-264.

Chong, M., F. Rous, and J. Testud, 1980: A New Filtering and Interpolating Method for Processing Dual-Doppler Radar Data: Performance in Three Dimensional Wind Restriction, Ability to Derive Pressure and Temperature Fields. Preprints 19th Conf. on Radar Meteorology., Miami Beach, Amer. Meteor. Soc., 286-293.

Condray, P. M., 1987: Momentum Flux in the Subcloud Layer of a Microburst- Producing Thunderstorm. M.S. Thesis, Saint Louis University, 97 pp.

Coover, J. A. Jr., 1986: Analysis of the Momentum Budget for

the Mesoγ-scale of a Severe Convective Storm. Unpublished paper for Met 589, Independent Study Course at Saint Louis Univ., Mo., 21 pp.

_____, Y. J. Lin and J. Rupp, 1988: Kinetic Energy Budget of Microburst-Producing Thunderstorm Based on JAWS Dual-Doppler Data. Preprints, 20th Conf. on Severe Local Storms, Baltimore, Amer. Meteor. Soc., 249-256.

_____, 1986: A Mesoγ-scale Kinetic Energy Budget of a Squall-line Thunderstorm Derived from SESAME dual-Doppler Data. M.S. Thesis, St. Louis University, 140 pp.

Deardorff, J.W., 1972: Numerical Investigation of Neutral and Unstable Planetary Boundary Layers. J. Atmos. Sci., 29, 91-115.

_____, 1975: The Development of Boundary Layer Turbulence Models for Use in Studying the Severe Storm Environment. Proc. SESAME open meeting, D. K. Lilly, ED., Boulder, NOAA Env. Res. Lab., 251-264.

Doviak, R. J., P. S. Ray, R. G. Strauch and L. J. Miller, 1976: Error Estimation in Wind Fields Derived from dual-Doppler Radar Measurements. J. Appl. Meteor., 15, 868-878.

_____, and D.S. Zrnic, 1984: Doppler Radar and Weather Observation. Academic Press, Inc. 458 pp.

Elmore, K.L., 1982: Cell Structure and Evolution Within a Squall Line as Revealed by dual-Doppler Radar. M.S. Thesis, Univ. of Oklahoma, 212 pp.

_____, J. McCarthy, W. Frost and H.P. Chang, 1986: A High Resolution Spatial and Temporal Multiple Doppler Analysis of a Microburst and Its Application to Aircraft Flight Simulation. J. Climate Appl. Meteor., 25, 1398-1425.

Foote, G. B., and P. S. DuToit, 1969: Terminal Velocity of Raindrops Aloft. J. Appl. Meteor., 8, 249-253.

_____, 1984: Study of Hail Growth Utilizing Storm Conditions. J. Climate Appl. Meteor., 23, 84-110.

Fuelberg, H.E., and J.R. Scoggins, 1978: Kinetic Energy Budgets During the Life Cycle of Intense Convective Activity. Mon. Wea. Rev., 106, 637-653.

_____, and _____, 1980: Kinetic Energy Budget During Strong Jet Stream Activity Over the Eastern United States. Mon. Wea. Rev., 108, 69-77.

_____, and G. J. Jedlovec, 1982: A Subsynoptic Scale Kinetic Analysis of the Red River Valley Tornado Outbreak (AVE-SESAME I). Mon. Wea. Rev, 110, 2005-2029.

_____, and M. B. Printy, 1984: A Kinetic Energy Analysis of the Meso γ -scale Severe Storm Environment. J. Atmos. Sci., 41, 3212-3226.

_____, and J. R. Scoggins, 1978: Kinetic Energy Budgets During the Life Cycle of Intense Convective Activity. Mon. Wea. Rev., 106, 637-653.

Fujita, T. T., 1985: The Downburst. Satellite and Mesometeorology (SMRP), University of Chicago, 51 pp.

_____, 1983: Microburst Wind Shear at New Orleans International Airport; Kenner, Louisiana on July 9, 1982. SMRP Res. Paper 199, University of Chicago, 39 pp.

_____, and R. M. Wakimoto, 1983: Microbursts in JAWS Depicted by Doppler Radars, PAM, and Aerial Photographs. Preprints, 21st Conf. on Radar Meteorology, Edmonton, Canada, Amer. Meteor. Soc., 638-645.

_____, 1976: Spearhead Echo and Downburst Near the Approach End of a John F. Kennedy Runway, New York City. SMRP, University of Chicago, 51 pp.

Gal-Chen, T., 1978: A Method for the Initialization of the Anelastic Equations: Implications for Matching Models with Observations. Mon. Wea. Rev., 106, 587-606.

_____, and C.E. Hane, 1981: Retrieving Buoyancy and Pressure Fluctuations from Doppler Radar Observations: A Status Report. Atmospheric Technology, NCAR, No. 13, 98-104.

_____, 1982: Errors in Fixed and Moving Frame of References:: Applications for Conventional and Doppler Radar Analysis. J. Atmos. Sci., 39, 2279-2300.

_____, and R. A. Kropfli, 1984: Buoyancy and Pressure Perturbation Derived from dual-Doppler Radar Observations of the Planetary Boundary Layer: Application for Matching

Models with Observations. J. Atmos. Sci., 41, 3007-3020.

Hane, C.E., R.E. Wilhelmson, and T. Gal-Chen, 1981: Retrieval of Thermodynamic Variables Within Deep Convective Clouds: Experiments in Three Dimensions. Mon. Wea. Rev., 109, 564-576.

_____, and P. S. Ray, 1985: Pressure and Buoyance Fields Derived from Doppler Radar Data in a Tornadic Thunderstorm. J. Atmos. Sci., 42, 18-35.

_____, and M. Liou, 1980: The Structure of a Midlatitude Squall Line: A Case Study. J. Atmos. Sci., 37, 553-567.

Hjelmfelt, M.R., 1986: The Microbursts of 22 June 1982 in JAWS. J. Atmos. Sci., 44, 1646-1664.

_____, 1984: Radar and Surface Data Analysis of a Microburst in JAWS. Preprints, 22nd Conf. on Radar Meteor., Zurich, Switz., Amer. Meteor. Soc., 64-69.

Hughes, R. G., 1986: Dynamic and Thermodynamic Characteristics of a Microburst-producing Storm in Colorado Determined from JAWS dual-Doppler Data. Ph. D. Dissertation, Saint Louis University, 213 pp.

Intrieri, J. M., A. J. Bedard and R. M. Hardesty, 1988: Doppler Lidar Observations of Colliding Outflow Boundaries. Preprints, 15th Conf. on Severe Local Storms, Baltimore, Amer. Meteor. Soc., 249-252.

Kessler, E., 1969: On the Distribution and Continuity of Water Substance in Atmospheric Circulations. Meteor. Mongr., No. 32, Amer. Meteor. Soc., 84 pp.

Klemp, J.B., and R.B. Wilhelmson, 1978: The Simulation of Three-Dimensional Convective Storm Dynamics. J. Atmos. Sci., 35, 1070-1096.

Krueger, S. K., 1988: The Role of Entrainment by Falling Raindrops in Microbursts. Preprints, 15th Conf. on Severe Local Storms, Baltimore, Amer. Meteor. Soc., J103-J106.

Kung, E. C., and T. L. Tsui, 1975: Subsynoptic-scale Kinetic Energy Balance in the Storm Area. J. Atmos. Sci., 32, 729-740.

LeMone, M. A., 1983: Momentum Transport by a Line of

Cumulonimbus. J. Atmos. Sci., 40, 1815-1834.

Lin, Y. J., and R. W. Pasken, 1982: A Diagnostic Study of the Tornadic Storm Based on Dual-Doppler Wind Measurements. Cloud Dynamics (Agee and Asai, Eds.), D. Reidel Publication Co., 315-328.

_____, T. C. Wang, and J. H. Lin, 1986: Pressure and Temperature Perturbations Within a Squall-line Thunderstorm Derived from SESAME Dual-Doppler Data. J. Atmos. Sci., 43 2302-2327

_____, 1986: Unpublished Notes on Parameterization of Eddy Kinetic Energy Equation.

_____, R. G. Hughes, and R. W. Pasken, 1987: Subcloud-layer Kinematic and Dynamic Structures of a Microburst-producing Thunderstorm in Colorado Determined from JAWS dual-Doppler Measurements. Boundary-Layer Meteorology, 39 67-86

_____, and R. G. Hughes, 1987: Structural Features of a Microburst-Producing Storm in Colorado Revealed by JAWS Dual-Doppler Radars. J. Atmos. Sci., 24 3640-3655

_____, and P. M. Condray, 1988: Momentum Flux in the Subcloud Layer of a Microburst-Producing Thunderstorm Determined From JAWS Dual-Doppler Data. Boundary-Layer Meteorology, 43 125-142

Maddox, R. A., 1980: Mesoscale Convective Complexes. Bull. Amer. Meteor. Soc., 61, 1374-1387.

Martner, B. E., 1975: Z-R and Z-W Relations from Dropsize Measurements in High-plains Thunderstorms. Preprints, 9th Conf. on Severe Local Storms, Norman, Amer. Meteor. Soc., 307-310.

McInnis, D. H., and E. C. Kung, 1972: A Study of Subsynoptic-scale Energy Transformations. Mon. Wea. Rev., 100, 126-132.

Miller, J., J. D. Tuttle, and C. A. Knight, 1988: Airflow and Hail Growth in a Severe Northern Plains Supercell. J. Atmos. Sci., 45, 736-762.

Moncrieff, M. W., and M. J. Miller, 1976: The Dynamics and Simulation of Tropical Cumulonimbus and Squall Lines.

Quart. J. Roy. Meteor. Soc., 102, 373-399.

Nelson, S. P., and R. A. Brown, 1982: Multiple Doppler Radar Derived Vertical Velocities in Thunderstorms. Part I - Error Analysis and Solution Techniques. NOAA Tech. Memo., ERL-NSSL-94, 21 pp.

Pan, D., 1987: An Eddy Kinetic Energy Budget of a Microburst-Producing Storm Derived from JAWS Dual-Doppler Data. Master's Thesis, Saint Louis University, 47 pp.

Parsons, D. B., R. A. Kropfli, J. M. Schmidt, and T. Gal-Chen, 1983: Comparison Between Doppler Radar Derived Air Motions in Fixed and Moving Frames of Reference. Preprints, 21st Conf. on Radar Meteorology, Edmonton, Canada Amer. Meteor. Soc., 558-564.

_____, C. J. Kessinger, K. L. Elmore, and R. D. Roberts, 1985: An Investigation into the Forcing of Microbursts. Preprints, 14th Conf. on Severe Local Storms, Indianapolis, Amer. Meteor. Soc., 48-51.

Pasken, R., 1981: A Study of the Kinematic, Dynamic and Thermodynamic Features of a Severe Right-moving Thunderstorm. Ph.D. Dissertation, Saint Louis University, 120 pp.

Proctor, F. H., 1988: Numerical Simulation of the August 2, 1985 DFW Microburst with the Three-Dimensional Terminal Area Simulation System. Preprints, 15th Conf. on Severe Local Storms, J99-J102.

Ogura, Y., and M. Liou, 1980: The Structure of a Midlatitude Squall Line: A Case Study. J. Atmos. Sci., 37, 553-567.

Ray, P. S., M. Gilet, and K. W. Johnson, 1980: The Multiple Doppler Radar Workshop, November, 1979 - Part VI: Motion field synthesis and radar placement. Bull. Amer. Meteor. Soc., 61, 1184-1189.

_____, K. K. Wagner, K. W. Johnson, J. J. Stephens, W. C. Bumgarner, and E. A. Mueller, 1978: Triple- Doppler observations of a convective storm. J. Appl. Meteor., 17, 1201-1212.

_____, C. L. Ziegler, W. Bumgarner, and R. J. Serafin, 1980: Single- and Multiple-Doppler Radar Observations of Tornadic Storms. Mon. Wea. Rev., 108, 1607-1625.

Rao, G. V., and J. Fishman, 1975: An Iterative Initialization Scheme for Mesoscale Studies. Tellus, 27, 157-167.

Roux, F., J. Testud, M. Payen, and B. Pinty, 1984: Pressure and Temperature Fields Retrieved from Dual-Doppler Radar Data: An Application to the Observation of a West-Africa Squall Line. J. Atmos. Sci., 41, 3104-3121.

Rupp, J.A., 1987: A Kinetic Energy Budget of a Microburst Derived from JAWS Dual-Doppler Data. M.S. Report, Saint Louis University, 53 pp.

Sanders, F., and K. Emanuel, 1977: The Momentum Budget and Temporal Evolution of a Mesoscale Convective System. J. Atmos. Sci., 34, 322-330.

Schlesinger, R. E., 1980: A Three-dimensional Numerical Model of an Isolated Thunderstorm, Part II: Dynamics of Updraft Splitting and Mesovortex Couplet Evolution. J. Atmos. Sci., 37, 395-420.

Smagorinsky, J., 1963: General Circulation Experiment with the Primitive Equations: 1. The Basic Experiment. Mon. Wea. Rev., 91, 99-164.

Spahn, J. F., and P. L. Smith, Jr., 1976: Some Characteristics of Hailstone Size Distributions Inside Hailstorms. Preprints, 17th Conf. on Radar Meteorology, Seattle, Amer. Meteor. Soc., 187-191.

Srivastava, R. C., 1985: A Simple Model of Evaporatively Driven Downdrafts: Application to Microburst Downdrafts. J. Atmos. Sci., 28, 1004-1023.

_____, 1987: A Model of Intense Downdrafts Driven by the Melting and Evaporation of Precipitation. J. Atmos. Sci., 49, 1752-1773.

Tsui, T. L., and E. C. Kung, 1977: Subsynoptic-scale Energy Transformations in Various Severe Storm Situations. J. Atmos. Sci., 34, 98-110

Wakimoto, R. M., 1988: Operational Aspects of a Microburst-Producing Storm During MIST. Preprints, 15th Conf. on Severe Local Storms, Baltimore, Amer. Meteor. Soc., 384-387.

Waldleufel, P., 1976: An Analysis of Weather Spetra Variance

in a Tornadic Storm. NOAA Tech. Memo. ERL-NSSL-76, 80 pp.

Ward, J. H., and P. J. Smith, 1976: A Kinetic Energy Budget Over North America During a Period of Short Synoptic Wave Development. Mon. Wea. Rev., 104, 836-848.

Wilson, J. W., R. D. Roberts, C. Kissinger, and J. McCarthy, 1984: Microburst Wind Structure and Evaluation of Doppler Radar for Airport Wind Shear Detection. J. Climate Appl. Meteor., 22, 1227-1241.

Wirsing, F.C., 1985: An Intercomparison of Variational Techniques in Deriving Three-Dimensional Wind and Pressure Fields from Dual-Doppler Radar Data of a Severe Right-Moving Thunderstorm. M.S. Thesis, St. Louis Univ., 96 pp.

BIOGRAPHY OF THE AUTHOR

John Anthony Coover Jr. was born August 15, 1959 in Sapulpa, Oklahoma. He later moved to Shamokin Dam, Pennsylvania where the rural setting provided many chances to get first-hand knowledge of the forces of nature. Originally interested in volcanology and art, his interest turned to meteorology in the eighth grade, partially due to experiencing the Hurricane Agnes floods of 1972. After graduating from Selinsgrove Area High School in 1977, the author attended The Pennsylvania State University, where he graduated in 1981 with a Bachelor of Science degree and an Air Force Commission. After 2 1/2 years of service in the United States Air Force as an operations meteorology officer, he was offered an assignment through the Air Force Institute of Technology (AFIT) to pursue a Master of Science degree at Saint Louis University which he gratefully accepted. This dissertation is the culmination of rewarded effort from some rewarding research, instruction and conversation the past several years. A dissertation not only opens more doors, it makes the path a little clearer.